Droplet impact and spreading of viscous dispersions and volatile solutions

Daniel A. Bolleddula

A dissertation submitted in partial fulfillment of
the requirements for the degree of

Doctor of Philosophy

University of Washington

2011

Program Authorized to Offer Degree: Mechanical Engineering

University of Washington
Graduate School

This is to certify that I have examined this copy of a doctoral dissertation by

Daniel A. Bolleddula

and have found that it is complete and satisfactory in all respects,
and that any and all revisions required by the final
examining committee have been made.

Chair of the Supervisory Committee:

_____

Alberto Aliseda

Reading Committee:

_____

Alberto Aliseda

_____

James J. Riley

_____

Lucien N. Brush

Date: _____

In presenting this dissertation in partial fulfillment of the requirements for the doctoral degree at the University of Washington, I agree that the Library shall make its copies freely available for inspection. I further agree that extensive copying of this dissertation is allowable only for scholarly purposes, consistent with "fair use" as prescribed in the U.S. Copyright Law. Requests for copying or reproduction of this dissertation may be referred to Proquest Information and Learning, 300 North Zeeb Road, Ann Arbor, MI 48106-1346, 1-800-521-0600, to whom the author has granted "the right to reproduce and sell (a) copies of the manuscript in microform and/or (b) printed copies of the manuscript made from microform."

Signature_____

Date_____

University of Washington

Abstract

Droplet impact and spreading of viscous dispersions and volatile solutions

Daniel A. Bolleddula

Chair of the Supervisory Committee:
Professor Alberto Aliseda
Department of Mechanical Engineering

Spray coating processes require accurate control over the impact of highly complex and viscous liquid droplets on solid surfaces. Here we use theory and experiments to investigate aqueous colloidal dispersions and acetone-based solution droplets impacting solid surfaces of varying wettability. Over a range of impact speeds and effective viscosities, $We \sim \mathcal{O}(1-300)$ and $Oh \sim \mathcal{O}(0.01-1)$, we observe that the spreading dynamics follows a decaying function in characteristic times, D/U, where D and U are the initial drop diameter and impact speed, respectively. The spreading diameter decays to an asymptotic value referred to as the maximum spreading diameter. The maximum spreading diameter β_{max} during inertial times $\mathcal{O}(D/U)$ is shown to be in good agreement with three models available in the literature. The centerline height dynamics reveal an unstudied resonant regime for $We \sim 30$. In this regime, the centerline height sinks below the formation of a thick rim. As the centerline height recovers, the rim height h_r is shown to increase linearly with time for our complex liquids and equivalently viscous Newtonian solutions. Immediately following this inertial driven regime, the drop continues to spread by capillarity until equilibrium. The transient spreading dynamics of an aqueous colloidal dispersion on nearly fully wettable substrates reveals that Tanner's law, $d(t) \sim t^{1/10}$, is approached but

not in a consistent manner. The effects of residual inertia influence these short term spreading dynamics of both colloidal dispersions focused on herein and glycerol/water solutions. In particular, the spreading dynamics is found to obey a robust power law $d(t) \sim C(t/\mu D/\sigma)^n$, where C is found to be an $\mathcal{O}(1)$ constant and $1/9 \lesssim n \lesssim 1/5$.

ACKNOWLEDGMENTS

This work would not have been possible without the generous support of Pfizer, Inc. and a quarter of funding from the Washington NASA Space Grant Consortium.

I'm grateful for the guidance of my committee which has been priceless throughout my time here at the University of Washington. I thank Prof. Riley for his attention to detail and developing my mathematical interests. I am also indebted by the generosity of Prof. Berg and Prof. Pozzo for use of their experimental facilities. I have developed a deeper appreciation for education in research and teaching from experiencing Prof. Berg's passion for science in and out of the classroom.

I have also benefitted by working closely with Prof. Brush on theoretical modeling. His insight and interest in science has been a constant source of inspiration. Finally, I am grateful to my advisor Prof. Aliseda for giving me the opportunity to learn, teach, and conduct research at the highest level. His patience, insight, and work ethic has been a constant source of inspiration and has served me well during my time at the UW. I hope to be a credit to him in the future.

The staff in the Department of Mechanical Engineering have been a friendly distraction during the work day. I'm grateful to each one of them for their kind assistance along the years.

I'm particularly thankful for the support of my friends here in Washington, Oregon, and Colorado. My life has been rich because of the great friends I have made and sustained during my time in graduate school and I count each one a blessing. They have motivated me to work hard and stay focused on the big picture.

I thank my family for their support and encouragement throughout my studies

here at the University of Washington. My mother continues to be a constant source of inspiration both professionally and personally. I would not be where I am without her unconditional love.

Finally I want to thank my wife for her love, support, and most importantly, friendship. I dedicate this work to her.

DEDICATION

To Shanna

TABLE OF CONTENTS

LIST OF FIGURES

LIST OF TABLES

Chapter 1

INTRODUCTION: SPRAY COATING AT A GLANCE

1.1 Overview

The impact of a liquid droplet on a solid surface is a problem ubiquitous in nature and industry. Despite the considerable amount of effort devoted to droplet impact over the past century, there has been little attention directed towards complex rheology liquids used in various industrial applications, such as spray coating. In these settings, a liquid stream is broken into small droplets (typically ranging from a few microns to a few millimeters in diameter) and those droplets impact a solid surface, applying a thin coating on the surface. An analog to spray coating is the process of spray painting where a distribution of droplets exits the nozzle orifice, impact a surface, and subsequently cure through evaporation of the solvent resulting in a thin dry film. These processes serve varying purposes such as preventing rust formation, providing water resistance, or simply for aesthetic qualities. Fundamentally, the process of a spray making contact with a solid surface can be broken down into individual droplets impacting, spreading, coalescing, and drying on a solid surface. All these processes are critical to providing a uniform and thin coat on a surface, however, the initial impact and spreading forms the foundation of a coat. Some of the liquids of interest in those processes are broadly classified as colloidal dispersions and high volatility solvents, and most of them have high viscosities with slightly non-Newtonian characteristics. When these liquid drops impact and spread on a solid surface many seemingly naive questions come to mind. How do suspension droplets differ from pure liquids? What mechanisms drive spreading? What conditions (impact velocity, drop size, etc.) enhance spreading?

These questions will be addressed under the driving motivation of spray coating processes and yet I will simultaneously explore a class of fluids with complex rheology that have received little attention in droplet impact and spreading processes. The focus of my effort will explore these questions under the context of a viscous complex rheology liquid droplet impacting perpendicular to a solid substrate. These results will provide a data set particularly relevant for spray coating operations and viscous colloidal dispersions and volatile solutions at large. A brief background on the driving motion of this study and the collaborative efforts of this initiative are described in the following section.

1.2 Motivation

In the pharmaceutical industry, tablets are coated for various purposes including masking unpleasant taste, delivering a time released active agent, or brand recognition, Aliseda et al. [4]. A simplified schematic of the cross section of a coating apparatus is seen in Figure 1.1. An atomizer placed in the center of a rotating drum sprays droplets in the size range of $\mathcal{O}(10 - 100\mu\text{m})$ at speeds of $U \sim$ 1-10 m/s. The tablets tumble and are dried by a secondary flow of air. The coating process is a complex thermodynamic process, yet at the tablet interface, it becomes a classic mechanics problem: droplets are impacted and may rebound, splash, or deposit cleanly as is desirable.

The present research is building off a collaborative effort between Pfizer Inc., UCSD, and UW exploring three fundamental problems. The initial phase of this work consisted of characterizing the atomization of these coating liquids using a high speed coaxial gas jet to promote break up of the liquid jet into droplets. The experiments conducted produced size and velocity measurements with a Phase Doppler Particle Analyzer (PDPA). The results were compared to a model and resulted in good agreement. In fact, the model is used currently by Pfizer, Inc. in predicting droplet size distributions for scale-up processes.

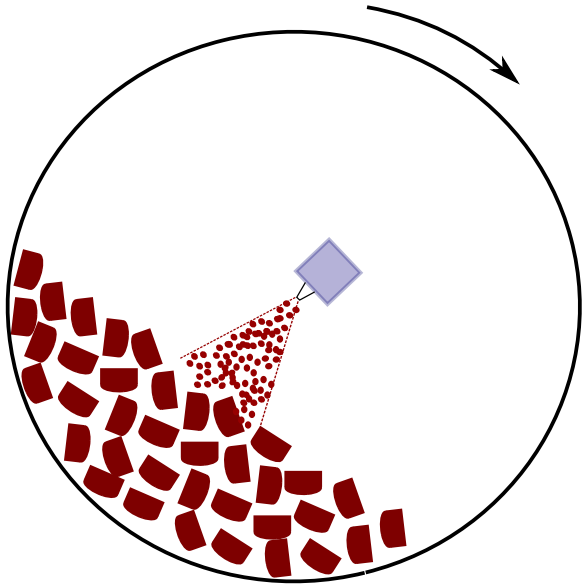

Figure 1.1: Simple schematic of spray coating operation. Atomizer at the center sprays tablets as they are turned. Drying air (not shown) subsequently cures coating.

Following complete atomization of the coating solutions, a collection of droplets downstream of the atomizer are transported to the tablet bed. The droplets undergo evaporation, shrinkage, and in some cases precipitous film formation on the periphery of the drop. The dynamics of these droplets between the initial plane and the tablet bed is another problem of importance. Currently, there is an ongoing effort to model the droplets using computational fluid dynamics with a Lagrangian approach. The goal is to predict the rheological changes occurring within the droplet as it travels toward the surface of the tablet bed. We have assisted Pfizer in this effort by providing some benchmark numerical solutions using realistic sizes and velocities of droplets from atomization experiments. Preliminary results revealed the spray angle and distribution of droplets approaching the tablet bed which is not highlighted in this document. Furthermore, our collaborators at UCSD have provided a model to measure the decrease in drop size as function of time, Sartori [5]. Finally, once droplets reach the tablet bed, they impact the tablet surfaces at various angles, velocities, and

sizes. The summation of all these events sets the film thickness and uniformity of the final coat.

These coatings formed by liquids are classified broadly as aqueous colloidal dispersions and acetone-based solutions. The latter are particularly useful in creating controlled-released functionality. Before one of these coatings is applied, the tablets, referred to as tablet cores, are in some cases loaded with a hydrophobic lubricant in powder form which is added with the drug in powder form before being compressed into a tablet. This sets the rate of dissolution of the coat but may also inhibit clean deposition of droplets on the surface. The parameter space for these operations is quite large as we set out to study 13 different liquid formulations varying in solid content and solvent and 12 tablet cores with varying surfaces properties quantified by tablet breaking force, percent of hydrophobic lubricant, and precoated tablets.

Our study implements realistic droplet size and velocity data from prior atomization experiments to set the parameter space indicative of spray coating processes. From the scientific perspective, this study investigates highly viscous liquids, with values of the Ohnesorge number ~ 1 which are higher than previously studied before. The $Oh = \mu/(\rho\sigma D)^{1/2}$ where ρ, μ, and σ denote the liquid density, viscosity, surface tension, respectively, and D the diameter of the drop, is strictly a function of geometry (D) and liquid properties and defines a balance between the shear resistance of the liquid and the restoring forces of surface tension. The ability of the droplets to impact, spread, coalesce, and dry are all critical to producing an effective tablet coat. If the scaling parameters in any of these processes, atomization, transport, and impact are not properly understood, the inevitable failure of the coat will result in wasted resources.

This dissertation consists of three distinct studies investigating the effects of particles and effective viscosities in the spreading of colloidal dispersions and acetone-based solutions on surfaces of varying wettability. Each chapter is meant to be read individually as they are self contained bodies of work. Chapter 2 begins with a detailed

description of the materials and methods and post processing of the data. Chapter 3 begins with a review of topics relevant to drop impact studies. Furthermore it investigates the effects of spreading of colloidal dispersions over a range of Weber and Ohnesorge numbers. We find that the colloidal dispersions resist spreading only slightly and the spreading dynamics agrees well with three different models. Chapter 4 explores the capillary spreading dynamics of colloidal dispersions on hydrophilic surfaces. In this transient regime, spreading follows a robust power law, but the exponents measured deviate from Tanner's law due to the influence of residual inertia and non-Newtonian rheology. The impact and spreading dynamics of acetone-based solutions particularly important for time released functionality is investigated in Chapter 5. Here we highlight a previously unreported regime in which the rim height is found to increase linearly as the centerline height oscillates to equilibrium. This regime is also present in the case of colloidal dispersions and viscous Newtonian solutions in a narrow range of parameters. Chapter 6 contains a summary of the key results from this study and a few potential next steps in this research initiative.

Chapter 2

MATERIALS AND METHODS

An overview of the materials and methods is described in this chapter. The composition of the liquids, preparation, and properties is presented first, followed by a characterization of the solid surfaces. Drop production is described followed by the entire setup of our experiments and data extraction techniques.

2.1 Liquids

2.1.1 Preparation of Colloidal Dispersions

The colloidal dispersions are prepared by slowly pouring a powder of colloidal particles into a beaker of water that has already formed a vortex by a magnetic stirrer. Care is taken in introducing the powder into the water to avoid excess aggregation and to promote uniform mixing. Once the powder is completely poured into water, the beaker is sealed and the dispersion is mixed for up 4 hours to ensure uniformity before experimentation. The colloidal particles are composed of varying proportions of Hydroxypropylmethycellulose (HPMC)/Lactose/TiO2/Triacetin/Polyethylene glycol(PEG)/Polyvinyl alcohol(PVA)/Talc. The colloidal particles are obtained from Colorcon, Inc., and are identified by the name Opadry. The particle sizes vary for each Opadry formulation but can range from 1-500 μm from tests conduced at Pfizer with a Malvern Mastersizer 2000 laser diffraction measurement. However, a representative particle size is $\mathcal{O}(1\mu m)$, see Figure 2.1. Furthermore the particles are completely wetted by the dispersion medium, in our case, water, and subject to aggregation.

2.1.2 Preparation of Acetone-based Solutions

Another brand of coating liquids used in this study are special formulations created by Pfizer to provide controlled release functionality of a particular drug. Such solutions are acetone rich and hence must be prepared as quickly as possible to avoid rapid evaporation. The acetone rich solutions are prepared by a mixture of water and acetone which is stirred until a central vortex forms in the beaker. The Polyethylene glycol(PEG) is added first then the Cellulose Acetate(CA) is slowly poured to avoid preferential aggregation of cellulose acetate units. Once the CA is completely poured, the beaker is covered and allowed to mix for up to 4 hours to ensure the CA is completely dissolved into solution. The powders are composed of Hydropropylcellulose(HPC), PEG, and Cellulose Acetate (CA). The exact proportions are proprietary and are commonly referred to as Pfizer membranes. These solutions have rapid response to evaporation since acetone evaporates much quicker than say water. When evaporation of acetone takes place, the free surface obtains a porous membrane which can impede drop production and spreading. Solutions of similar nature have been studied in the context of drug release rates in Altinkaya [6]. We discuss these matters further and demonstrate the existence of a distinct membrane in Chapter 5. As a basis of quantifying any nonlinear behavior of these complex liquids studied focused herein, we use glycerol/water solutions at matched dimensionless groups (i.e. Oh) to provide case by case comparisons. These solutions are prepared in a similar manner to the acetone based and colloidal dispersions.

2.2 Target Surfaces

The impact surfaces are actual tablet cores which vary in composition, hardness, and surface treatments. The tablet cores are made with either Microcrystalline cellulose (MCC) or Magnesium Stearate. The main variable in this study is the amount of hydrophobic lubricant loaded in the tablet which varies from 0 to 4%.

Acrylic, mica, and teflon surfaces are tested as well which have similar energetics as the slightly rougher tablet core surfaces. The mica surfaces are cleaved from thin sheets and produce a smooth surface. The acrylic (PMMA) and teflon surfaces are cleaned with methanol and allowed to dry before each test.

The surface energetics are obtained from sessile drop measurements on the liquid/surface combinations and show partial wetting characteristics for both the colloidal dispersions and acetone rich solutions. Exact values will be documented in subsequent chapters.

The roughness of a surface is particularly important in discriminating various splashing events. Such events are prevalent for high speed impacts on relatively rough surfaces. Herein, the tablet cores are prepared through a compression mold of forming constituents and the active ingredients. The samples used here are placebos but have similar roughness characteristics of formulated tablets. The roughness measurements were carried out using a MarSurf X20 surface metrology equipment. The measurement technique is consists of placing the profilometer tip on the tablet surface and dragging 4 millimeters across the tablet surface which indicates a run. Once the tip reaches the end it goes back and forth once more which are indicated as runs 2 and 3. The tablet is then rotated 90° in the same plane and the runs are sequenced again. A summary of these results are listed in Table 2.1. The validity of subsequent runs are drawn into question as it is clear that each run shows a higher roughness value for each test. It was evident that the profilometer tip was coarsening the surface after observing trace particles were left on surface. However a consistent trend showed that the roughness on tablet 03135 > 03134 > 03136. For the entire list of coating liquids and tablets we set out to study see Appendix B.

2.3 Drop production

Single drops are ejected by one of two methods. 1) A drop of liquid is forced through a blunt needle via a syringe pump and allowed to drop under its own weight. A

Table 2.1: Average roughness R_a measurements in μm of tablets 03134, 03135, and 03136 with 0, 2, and 4% hydrophobic lubricants.

Tablet	test	Run 1	Run 2	Run 3	Average	Std. Dev.
3134	1	2.146	2.239	2.344	2.243	0.10
	2	1.749	2.009	2.039	1.932	0.16
3135	1	2.429	2.546	2.988	2.655	0.30
	2	2.054	2.230	2.359	2.214	0.15
3136	1	1.926	1.963	1.989	1.959	0.03
	2	1.734	1.992	2.028	1.918	0.16

critical drop size for release from a syringe can be found from a force balance at the drop/syringe boundary given as $D = (6\sigma D_0/\rho g)^{1/3}$, where D_0 is the inner radius of the orifice. This relationship gives a reasonable upper bound on the size of the drop D, although a correction factor has been shown to provide better agreement, Middleman [7]. The impact speeds vary from 0.3-2.5 m/s with corresponding release heights of 35-300 mm, respectively. 2) Drops of size $D < 1$ mm are more challenging to generate through conventional techniques. However, we use a technique more common to the ink-jet industry, namely (Drop-on-Demand technology).

One common Drop-on-Demand (DOD) technique is driven by a piezoelectric disc or sleeve which acts to squeeze a liquid column out of an orifice and subsequently break off by surface energy minimization. Here we use a piezodriven capillary tube methodology that ejects monodisperse drops of size $D \sim \mathcal{O}(10-100\mu m)$. A capillary tube is surrounded by a piezoelectric sleeve. A voltage source is used to send a signal to the piezoelectric sleeve. The sleeve expands and squeezes with each pulse which in turn induces a volume change inside the capillary tube, Dijksman [8]. The sleeve bonded to a capillary tube is referred to herein as the drop generator, Figure 2.3. The drop generator and signal source (jetting driver) are from Microfab, Inc., in Plano, TX.

The procedure and mechanism of droplet ejection is as follows. Liquid is pumped into the capillary tube until the meniscus of the liquid is level with the tube outlet, then a waveform is sent to the piezo device which evokes a pressure pulse inside the liquid thread. Once the kinetic energy of the liquid tongue ejected out of the tube is sufficient, capillarity will break the thread into one or a series of drops on the order of $\mathcal{O}(10 - 100\mu m)$, Figure 2.5. The generation of drops by this method is commonly referred to as Drop-on-Demand technology, Chen and Basaran [9]. Here we use a slightly modified square waveform that follows the form shown in Figure 2.2 and with a exact parameters seen in Table 2.2, Son and Kim [10].

It is also possible to generate drops that impact at higher speeds ($U \sim 1$ m/s) while still obtaining realistic drop sizes seen in atomization processes. When drops cannot be generated by the above method, we use the theory of Rayleigh-Plateau jet breakup which predicts the largest wavelength necessary to break up a liquid jet into a series of drops. Coupling jet instability with a forced perturbation creates drops earlier in the jet stream and at higher speeds. This methodology is implemented in the more volatile acetone rich solutions where membrane formation impedes drop generation by the DOD method.

The colloidal dispersions and acetone rich solutions are pumped at (1.12 ml/s) through the piezodriven capillary tube and leave as a liquid jet. A waveform is sent which breaks up the liquid jet into monodisperse drops. This methodology allows higher impact speeds not achievable with the prior technique.

2.3.1 Cleaning piezoelectric nozzle

Before and after use of piezoelectric nozzles, the nozzle should be cleaned according to the following steps

1. Vacuum backflush the device by applying vacuum through a syringe and immersing the nozzle glass tip within a clean solvent (isopropanol). Warm solvents

can be used for remove an orifice clog.

2. Vacuum backflush with 2% water solution of Micro-90 cleaning solution or equivalent.

3. Vacuum backflush with DI water for at least one minute followed by a one minute vacuum backflush of acetone. Check nozzle tip for clarity and repeat steps as necessary.

2.4 High Speed Imaging

The sequences of drop generation, flight, and impact on solid surfaces are visualized through a Phantom V12.1 High Speed Camera. For millimeter size drop impacts we film at 7600 fps. For micron size drop impacts we film at rates of 30000-60000 fps. For drops 100 μm and larger we are able to capture the inertial and capillarity driven spreading dynamics. The millimeter size drops are seen with a Tamron Lens with a spatial resolution of 17 μm/pixel. A long distance microscope from Infinity, Inc., provides a spatial resolution of 1.45 μm/pixel.

2.5 Setup

An overall setup up the experimental apparatus consists of a high speed camera viewing a drop falling from a profile perspective, Figure 2.4. The impact surface is placed on a vertical stage and the drop generation devices are mounted on a vertical traverse. The drops are backlit by an Edmunds optical light source. The high speed camera and voltage source (jetting drive) have independently controlled user software.

The camera has an internal buffer and can be triggered post impact within a reasonable response time thus requiring no automation. Similarly, the waveform sent to the drop generator can be triggered on demand. The protocol for a single drop impact experiment is enumerated as follows:

1. Feed liquid through tubing until near exit of orifice

2. Click Capture to ensure any .cine files remaining in the memory are deleted which will render the Trigger button active.

3. Start pumping of liquid until drop falls for mm size drops. Start waveform for μm size drops

4. When drop impact is observed, Click the Trigger button. (*The camera has an internal buffer memory and thus the trigger button only stops recording if the camera is in post trigger mode, see Vision research documentation for details on pretrigger settings. The camera can also be programmed to record at multiple frame rates in a single recording session (see 'frame-rate profile')*)

2.6 Post-Processing

Once the video is collected, several quantities are extracted from image processing. NASA's image processing software, Spotlight, is used to extract the drop size, velocity, and spreading dynamics. The drop size is calculated from the vertical and horizontal diameters and then an equivalent diameter is calculated by $D_{eq} = (D_h^2 D_v)^{1/3}$. The drop velocity U is averaged over the distance travelled 5 to 10 frames just before impact and is calculated according to

$$U = \frac{\Delta x}{\Delta t} = (\text{distance travelled in pixels}) \times (\text{scale factor in [units]/pixel}) \times (\#\ \text{frames/frames per second}). \quad (2.1)$$

The spreading diameter and centerline height is either extracted manually when the image quality is poor or through a threshold.

The images are referenced by a scale factor obtained by capturing an image of a ruler of characteristic dimension for the drops studied, namely millimeter and micron

sized drops. Once the scale factor is related to pixels, the drop size and velocity is calculated by entering the AOI (Area of Interest) tab. Particular points can be tracked automatically with the step by step procedure detailed in Appendix A.

Table 2.2: Typical waveform parameters for drop-on-demand ejections, all in μs.

rise	dwell	fall	echo	final rise
2	15	4	45	2

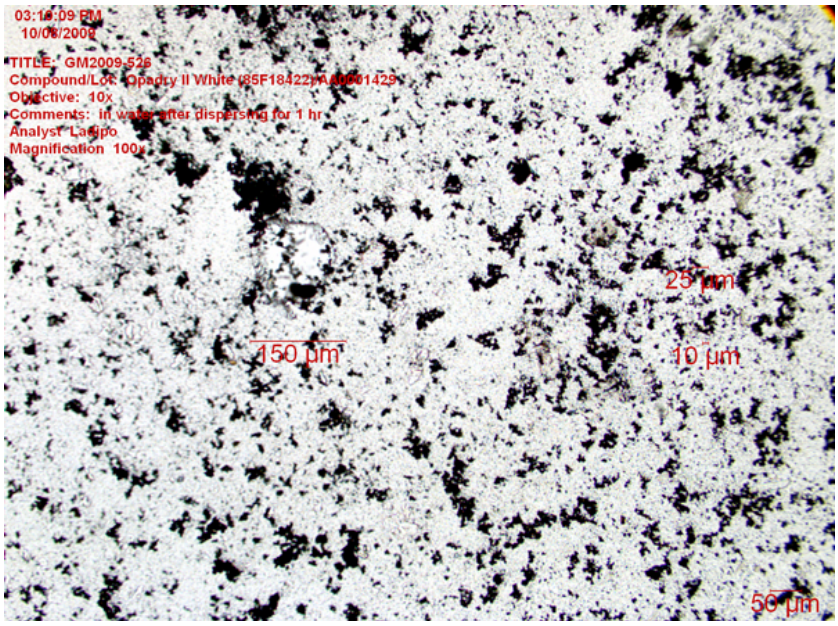

Figure 2.1: Representative particle size of aqueous dispersions used in present study. Most of the particles are approximately 1 μm of TiO_2.

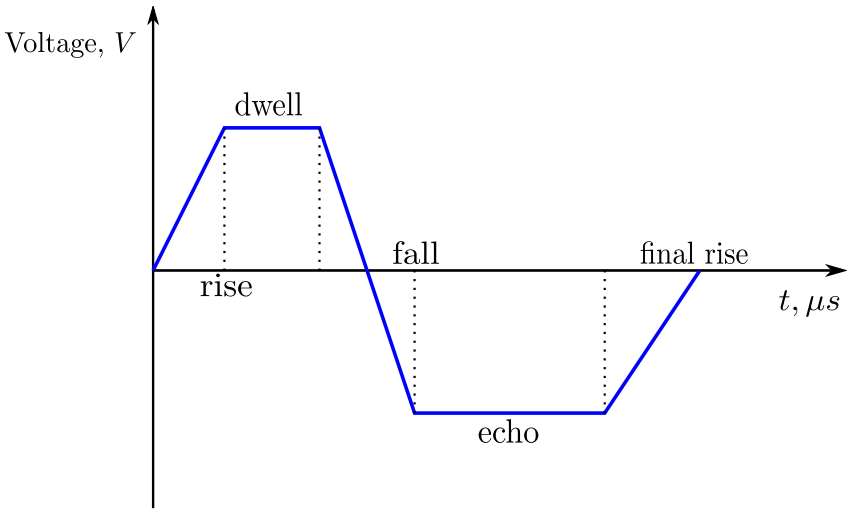

Figure 2.2: Typical waveform used to generated $\mathcal{O}(\mu m)$ sized drops. The specific times are identified in Table 5.2.

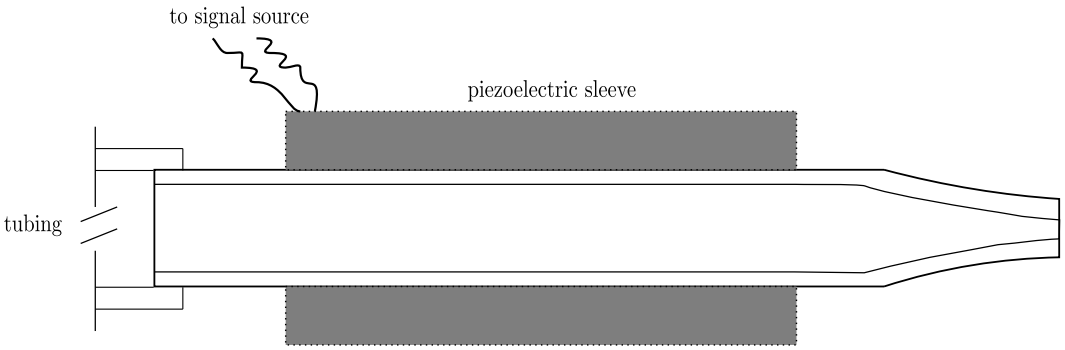

Figure 2.3: Schematic of piezoelectric sleeve bonded to capillary tube.

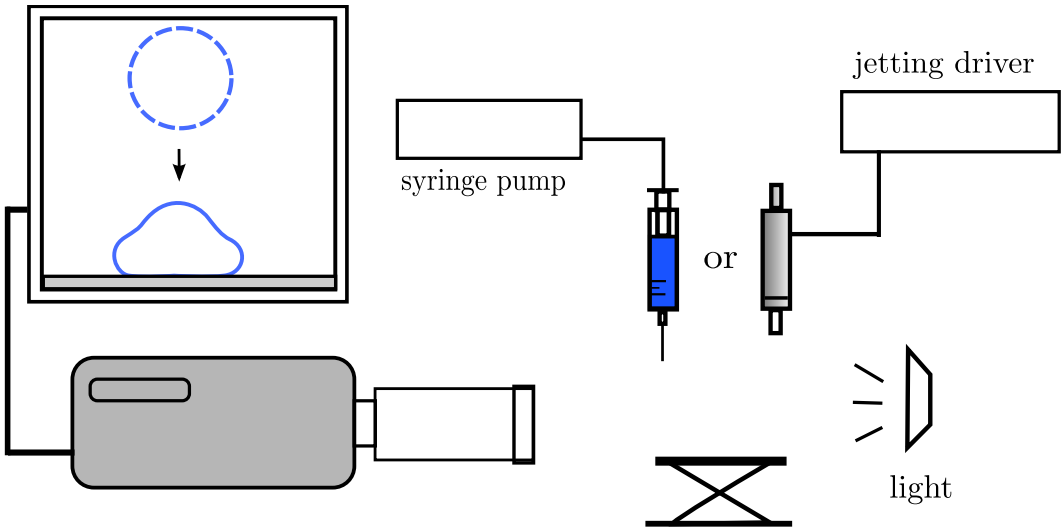

Figure 2.4: Schematic of experimental apparatus.

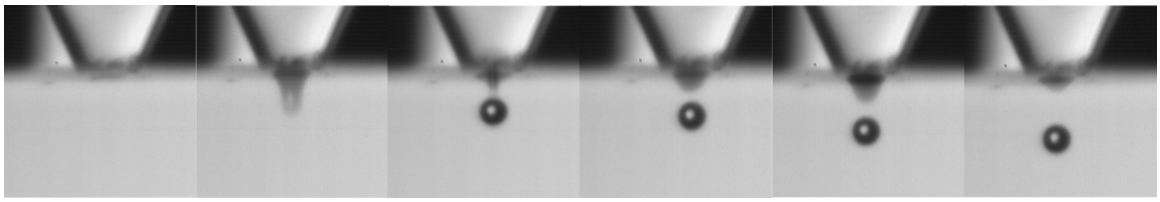

Figure 2.5: Illustration of drop-on-demand technique. A water drop of size $D \sim 30$ μm is ejected from orifice when liquid tongue ejects is long enough for capillarity to pinch off. The orifice is has an inner diameter of approximately 60 μm. Time between each frame is 37 μs.

Chapter 3

IMPACT OF A HETEROGENEOUS LIQUID DROPLET ON A DRY SURFACE

Droplet impact is a problem of fundamental importance due to the wealth of applications involved, namely, spray coating, spray painting, delivery of agricultural chemicals, spray cooling, ink-jet printing, soil erosion due to rain drop impact, and turbine wear. Here we highlight one specific application, spray coating. Although most studies have focused their efforts on low viscosity Newtonian fluids, many industrial applications such as spray coating utilize more viscous and complex rheology liquids. Determining dominant effects and quantifying their behavior for colloidal suspensions and polymer solutions remains a challenge and thus has eluded much effort. In the last decade, it has been shown that introducing polymers to Newtonian solutions inhibits the rebounding of a drop upon impact, Bergeron et al. [11]. Furthermore Bartolo et al. [12] concluded that the normal stress component of the elongational viscosity was responsible for the rebounding inhibition of polymer based non-Newtonian solutions. We aim to uncover the drop impact dynamics of highly viscous Newtonian and complex rheology liquids used in pharmaceutical coating processes. The generation and impact of mm and μm size drops of coating liquids and glycerol/water mixtures on tablet surfaces is systematically studied over a range of $We \sim \mathcal{O}(1-300)$, $Oh \sim \mathcal{O}(10^{-2}-1)$, and $Re \sim \mathcal{O}(1-700)$. We extend the range of Oh to values above 1, not available to previous studies of droplet impacts. Outcomes reveal that splashing and rebounding is completely inhibited and the role of wettability is negligible in the early stages of impact. The maximum spreading diameter of the drop is compared with three models demonstrating reasonable agreement.

3.1 Introduction

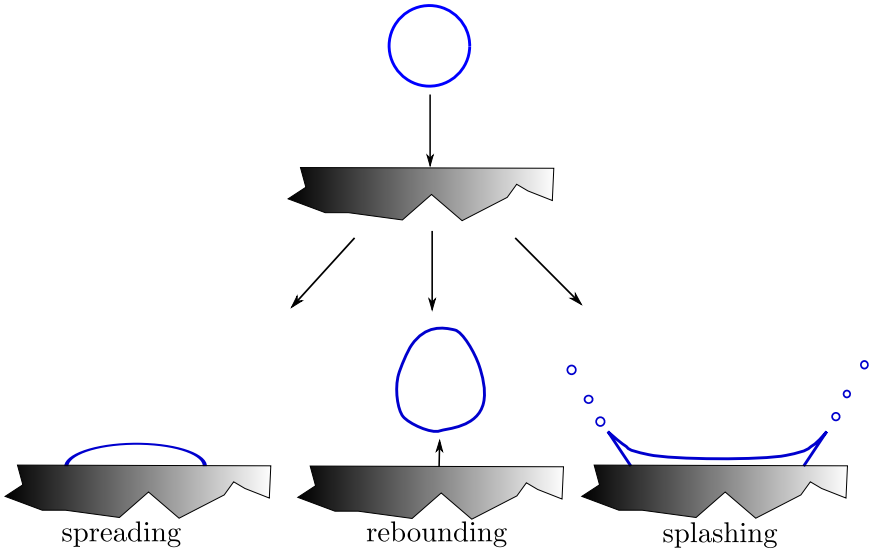

Figure 3.1: Impact of a drop on a solid surface: spreading, bouncing, and splashing.

When a liquid drop orthogonally impacts a solid substrate, the drop may deposit into a thin disk, disintegrate into secondary droplets, or recede and possibly rebound and bounce, see Figure 3.1. When inertia is negligible the drop will deposit gently over the surface until equilibrium is reached. This equilibrium is a function of the solid/liquid/gas contact point commonly defined by the contact angle, θ. If the contact angle is at a minimum ($\theta = 0$), the drop will spread indefinitely into a thin film, potentially reaching molecular thickness (e.g. silicone oil on glass). If $\theta > 0$, the drop will attain equilibrium once balance is reached between gravity, capillarity, and viscosity in a time of $\mathcal{O}$(s). If the drop approached the substrate with sufficient kinetic energy, then the balance is complicated by the addition of inertia. When the surface/liquid combination has a high contact angle ($\theta > 90°$) at equilibrium, then inertia will act to maintain excess surface energy upon impact and may partially recede the drop and even completely lift the drop off the surface. If the substrate is roughened, the drop may splash upon impact. Dimensional analysis provides a list of

relevant parameters useful in discriminating these drop impact outcomes,

$$We = \frac{\rho D U^2}{\sigma}, Re = \frac{\rho D U}{\mu}, Oh = \frac{\mu}{(\rho \sigma D)^{1/2}} = \frac{We^{1/2}}{Re}, K = WeOh^{-2/5}, \tag{3.1}$$

where ρ, μ, and σ denote the liquid density, viscosity, surface tension, respectively, and D and U are the initial drop diameter and impact velocity, respectively. We, Re, and Oh are the Weber, Reynolds, and Ohnesorge numbers, respectively, and K is a composite group that can be used to identify the onset of splashing. Gravity related effects are described through the Bond number $Bo = \rho g D^2/\sigma$ or by the Froude number $Fr = U^2/(gD) = We/Bo$. Usually, gravity effects are considered negligible in drop impact, yet this assumption is typically unsubstantiated. Two difficult parameters to model are roughness and wettability effects. These two parameters prove to be challenging in theoretical modelling yet are crucial to providing accurate boundary conditions at the contact line (i.e. three phase line or triple point, or interline).

It is clear that dimensional analysis provide a reduced set of components by which characterization can be simplified. Yet there remains many questions left unanswered. There must be a systematic methodology implemented in order to delineate potential outcomes. Previous investigators have determined qualitatively the influence of various parameters such as viscosity, velocity, etc.. and thereby determined their relative tendency to attain a specific outcome. It is still not clear whether dynamic similarity is held by the use of the above nondimensional parameters, Rioboo and Tropea [13]. However, it is also not clear if these parameters alone are sufficient in characterizing more complex rheological features.

Drop impact studies are commonly motivated by their ubiquity in nature and industry. However, the overwhelming majority of studies available has elucidated the behavior of pure liquids of low viscosity. This class of liquids is appropriate for the application towards the inkjet industry, agricultural sprays, or the aerospace industry. Pharmaceutical tablet spray coating processes typically contain liquids of complex rheology, containing large amounts of insoluble solids and considerably higher

viscosities, $\mu > 10$ cP. We are unaware of previous studies of droplet impact in the context of a range of parameters characteristic of spray coating processes utilized in the pharmaceutical industry to prepare tablet cores in final dosage form. It is our intention to provide a quantitative study of aqueous-based colloidal dispersions and their impact in a range of parameters characteristic of pharmaceutical coating operations.

Tablets are coated for various purposes including masking unpleasant taste, providing a barrier to moisture, delivering a controlled released active agent, or brand recognition, Aliseda et al. [4]. A simplified schematic of the cross-section of a coating apparatus is seen in Figure 3.2. An atomizer placed in the center of a rotating drum sprays droplets on the size range of $\mathcal{O}(10 - 100\mu\text{m})$ at speeds of $U \sim$ (1-10 m/s). The tablets tumble and are dried by a secondary flow of air. The coating process is a complex thermodynamic process yet at the tablet interface, droplets are impacted and may rebound, splash, or deposit cleanly as is desirable. An important question is how critical are the physical size of the droplets and impact speeds to deposition behavior. We hope to address that question in this study.

To date, solid and liquid surface impacts have been studied which has prompted two recent reviews on the subject, Rein [14], Yarin [15]. Despite the numerous studies conducted to date, there is a gap in the knowledge regarding complex fluids which are used in industrial coating processes. The effects of surfactants in liquids led to the investigation of dynamic surface tension, Zhang and Basaran [16]. The introduction of polymers revealed that rebound can be completely suppressed, which is explained by the elongational viscosity, Bergeron et al. [11]. The inkjet industry has benefitted significantly from drop impact studies such as Kannangara et al. [17] and Daniel and Berg [18]. These studies and more will be described in further detail in the following section with special attention to those relevant to coating fluids used in pharmaceutical industries.

The goal of this section is not to replicate the reviews mentioned above, but to pro-

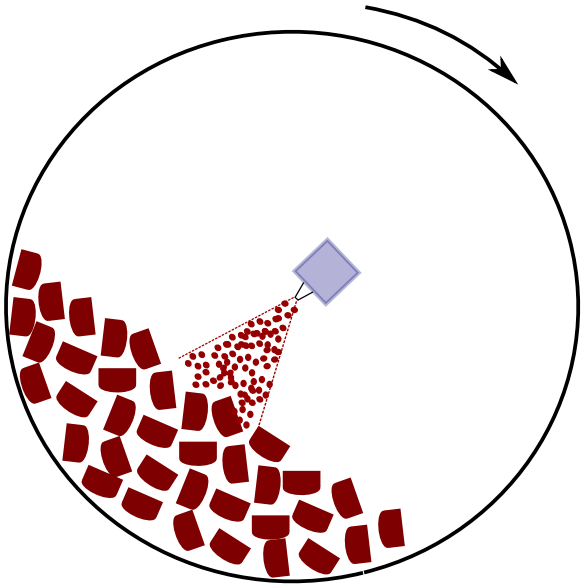

Figure 3.2: Simple schematic of spray coating operation. Atomizer at the center sprays tablets as they are turned. Drying air (not shown) subsequently removes coating solvents for final film formation.

vide background on relevant concepts obtained from notable studies on droplet impact on dry surfaces. We also aim at elucidating the need for accurate modelling considering non-Newtonian features. We will review prior studies conducted in three broad categories: spreading, splashing, and rebounding for Newtonian fluids. Subsequently, a survey of micron sized impact studies will be outlined. Finally, a review of impacts of complex fluids (multiple liquid phases, colloidal dispersions, non-Newtonian characteristics) will follow. The experimental work is described followed by the results, analysis and conclusions.

Four parts of this study are described in Sections 3.3 and 3.4

1. Determine rheology of coating liquids

2. Determine impact outcomes of pharmaceutical coating liquids in a range of dimensionless groups indicative of these processes.

3. Compare the effect of viscosity from coatings and glycerol/water solutions

4. Determine utility of existing models that predict the maximum spreading diameter

3.2 Background and Review

Droplet impact has been studied for over a hundred years dating back to the pioneering work of Worthington [19]. In fact, much of his ingenuity contributed to modern day high speed photography. Over the past 40 years significant contributions in theoretical, numerical, and experimental work have been made. Here a review of three broadly categorized outcomes are reviewed, namely spreading, splashing, and rebounding. Following these sections, two sections highlighting the contributions of droplet impact studies utilizing complex solutions and micron sized drop impact experiments will be highlighted.

3.2.1 Spreading

Negligible Inertia

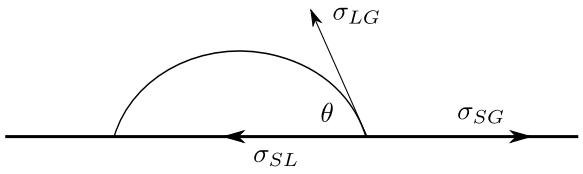

Figure 3.3: Force balance at contact line

When a drop is gently placed on a solid substrate, the balance of capillarity, gravity, and viscosity ensues. The Bo and the capillary number, $Ca = \mu U_{cl}/\sigma$, where U_{cl} is the velocity at the contact line, are typical parameters that describe the balance of forces. The wettability is defined by the contact angle. A simple horizontal force balance at the contact line gives us the well known Young's equation, Eq. 3.2

$$\cos\theta = \frac{\sigma_{SG} - \sigma_{SL}}{\sigma_{LG}}. \tag{3.2}$$

If the surface is has low surface energy and the liquid has high surface tension the liquid will not spread indefinitely, but attain a shape of minimum area approximating a spherical cap resting on the surface as shown in Figure 3.3. The angle drawn in the liquid is defined as the contact angle, θ. The contact angle and surface tension of the liquid-gas interface are both measurable quantities but the quantity in the numerator of Eq. 3.2 is not. However, the magnitude of the numerator can be estimated from the known contact angle and liquid surface tension. The solid surface energy has been estimated by equations of Girifalco-Good and Fowkes which demonstrates attractive or repulsive forces, Berg [20]. The contact angle defined by Young's equation is defined at equilibrium. However, the angle attained when the three phase contact line is moved forward (advanced) or backward (receded) is a better indication of solid/liquid interfacial energies. The advancing and receding angle can be determined through many techniques, most notably the sessile drop method. The difference between the advancing angle, θ_{adv}, and the receding angle, θ_{rec} is defined as the hysteresis $\Delta\,\theta$. Causes for such hysteresis are attributed to surface roughness and chemical heterogeneity, de Gennes [21]. The time scale associated with these impacts can be considerably longer if $Ca < 1$, being $\mathcal{O}$(s). Such experiments can be modelled using a lubrication approximation to the Navier-Stokes equations to yield an equation for the height of the drop. The results can be recast in terms of the spreading diameter, Starov et al. [22], Cox [23], and Hocking and Rivers [24].

Rioboo et al. [25] approximated the final diameter of a small drop on a surface with the inclusion of advancing and receding contact angles

$$\frac{d_i}{D} = 2\left[\frac{\sin^3\theta_i}{2(1-\theta_i)(2-\cos\theta_i-\cos^2\theta_i)}\right]^{1/3}, \tag{3.3}$$

where the subscript, i, denotes the advancing or receding contact angle. This formula is only valid for small drops, smaller than the Laplace length $\ell = \sqrt{\sigma/\rho g}$.

If gravity and viscosity are in balance, the radius of the drop $R \sim t^{1/8}$, Middleman [7]. If surface tension is included then the classical Tanner's law is derived , $R \sim t^{1/10}$, Tanner [26]. Both agree well with experimental data, Chen [27]. It was also shown by Rafaï et al. [28] that when non-Newtonian effects such as normal stress and shear thinning components are included, deviations from Tanner's law are minor and only require logarithmic corrections. Additional effects have been observed such as the thin precursor film of submicron dimensions which commonly is used to alleviate the force singularity at the contact line. Additionally, when this film is of the order of a few hundred Angstroms, van der Waals forces introduce additional interfacial forces commonly described as disjoining pressure. For further discussion of contact line related concepts see Dussan [29] and de Gennes [21]

Moderate Inertia

When a drop impacts for $We \gg 1$, impact is further complicated by the addition of inertia. Thus, the kinetic energy of the drop immediately before impact will play a determining role in the subsequent outcome. If the speeds are moderate and the surface is relatively smooth, the drop will spread out like a disc and come to rest as a truncated sphere or a thin film depending on the equilibrium contact angle of the system. As described before, the contact angle will still play a role in the final shape as the drop may recede and advance in an oscillatory manner until viscosity dampens the motion. The time scale of spreading associated with inertia is approximately D/U which yields milliseconds and μs for mm and μm sized drops, respectively. For partially wetting systems $\theta > 0$, Chandra and Avedisian [30] observed entrainment of a small air pocket inside the drop upon impact. Subsequently, van Dam and Clerc [31] used scaling arguments to describe the size of the bubble yielding a characteristic length, L_b as

$$L_b = \frac{\nu_{air}}{U_0}\left(\gamma_1^4 \frac{\rho}{\rho_{air}}\right)^{1/3}, \tag{3.4}$$

where γ_1 is an $\mathcal{O}(1)$ adjustable parameter. Agreement between experiments is quite reasonable. Furthermore, Medhi-Nejad et al. [32] simulated the impact of water, n-heptane and molten nickel droplets on a solid surfaces and verified the entrainment of an air bubble under the impacting droplet.

Although droplet impact affords significant experimental parameter space, the effort in modelling has promoted the use of a simple energy balance to predict the maximum spread of a droplet upon impact without splashing. Attané et al. [33] reviewed a large set of experimental data and contributed a new 1-D energy balance model to predicted the dynamics of the spreading diameter. This approach dates back to Chandra and Avedisian [30] which will be outlined here.

Maximum spread: Energy Balance

The classical approach is to use an Energy Balance as follows

$$\underbrace{E_k + E_p + E_s}_{\text{before impact}} = \underbrace{E_k^{'} + E_p^{'} + E_s^{'} + E_d^{'}}_{\text{after impact}}, \tag{3.5}$$

and mass conservation

$$m = m'. \tag{3.6}$$

If splashing does not occur then work done by viscosity to dissipate energy is $E_d^{'} = E_k + E_p + E_s$. The kinetic and surface energy before impact can be described by

$$E_k = \frac{1}{12}\rho U^2 \pi D^3, \tag{3.7}$$

and

$$E_s = \pi D^2 \sigma. \tag{3.8}$$

At maximum extension, the surface energy can be described by

$$E_s^{'} = \frac{\pi}{4} D_{max}^2 \sigma (1 - \cos\theta), \tag{3.9}$$

where the contact angle is defined herein at equilibrium.

The dissipated energy is difficult to determine since the velocity distribution inside the droplet is not known. This is the major modelling challenge which is still a topic of ongoing investigation, Roisman et al. [34], Roisman [3], Attané et al. [33]. Chandra and Avedisian [30] used a very simple model to determine $E_d^{'}$

$$E_d^{'} = \int_0^{t_e} \int_V \phi \, dV dt \approx \phi V t_e. \tag{3.10}$$

The dissipation per unit mass of the fluid is given by

$$\phi = \mu \left(\frac{\partial u_x}{\partial y} + \frac{\partial u_y}{\partial x} \right) \frac{\partial u_x}{\partial y} \approx \mu \left(\frac{U}{h} \right)^2, \tag{3.11}$$

where t_e is the characteristic time for deformation estimated to be $t_e \approx D/U$. The volume of the droplet when flattened out can be approximated by the shape of a disc as

$$V \approx \frac{\pi}{4} D_{max}^2 h, \tag{3.12}$$

where h represents the height of the disc. If we combine Eqs 3.5-3.12, introducing the Re and We with $\beta_{max} = D_{max}/D$ and $E_p = E_p^{'}$, the equation for the splashing deposition boundary is obtained

$$\frac{3}{2} \frac{We}{Re} \beta_{max}^4 + (1 - \cos\theta) \beta_{max}^2 - (\frac{1}{3} We + 4) = 0 \tag{3.13}$$

From this equation one can obtain an expression for the maximum diameter. For coating liquids utilized in the pharmaceutical industry, viscosities are high, $\mu >$ 10cP and surface tensions are low $\sigma \sim 0.04$ N/m. In such circumstances, a balance between the initial kinetic energy $\rho D^3 U^2$ and viscous dissipation $\mu (U/h) D_{max}^3$ along with volume conservation $h \sim D^3/D_{max}^2$ yields $\beta_{max} \sim Re^{1/5}$ as remarked in Clanet et al. [35].

Experimental validation in Chandra and Avedisian [30] shows over-prediction of β_{max} which is attributed to the underestimation of the energy dissipated during droplet deformation. It is the viscous dissipation which continues to draw questions as

to the validity in modelling. A simple model describing the force balance in squeezing of a cylinder under a mass yields an equation that can be fit to the regression group $(Re^2Oh)^a$ with agreement within 10% of experimental data, Scheller and Bousfield [36]. Pasandideh-Fard et al. [37] derived the time to β_{max} as $t_\beta = 8D/3U$ Many authors have made assumptions to more accurately define viscous dissipation but most lack universality, Mao et al. [2], Asai et al. [1]. Most recently, Attané et al. [33] pursued the viscous dissipation term with vigor and collected the various approaches from the literature. In Attane's paper, he used the unsteady energy equation and listed two commonly used geometries at the maximum spread, the spherical cap, or cylinder. A second-order nonlinear differential equation describes the height of the drop with the use of an empirical function of the Oh number. The agreement is quite good using a diverse set of experimental and numerical data from the literature and expands upon previous work, predicting the dynamics of drop spreading. Mao et al. [2] used a stagnation point flow to model the flow distribution in the drop and developed a low and high viscous regime model for β_{max}. The model is fitted with a least squares regression to the data and is written as

$$\left[0.2Oh^{0.33}We^{0.665} + \frac{1}{4}(1-\cos\theta_{eq})\right]\beta_{max}^2 + \frac{2}{3}\beta_{max}^{-1} = \frac{We}{12} + 1. \tag{3.14}$$

The model of Mao et al. [2] which, like most models, only predicts the β_{max}, agrees within 10% of experimental data in the literature. Another later model by Asai et al. [1] provides a simple correlation

$$\beta_{max} = 1 + 0.48We^{0.5}\exp[-1.48We^{0.115}Oh^{0.21}], \tag{3.15}$$

ignoring the effect of the contact angle but still providing good agreement with their micron drop impact experiments. Roisman et al. [38] provides one of the few models that describes the rate of the spread and the maximum diameter without the use of any adjustable parameters. Roisman points out that the energy balance approach, does not reliably describe the flow in the impacting drop. Instead, a mass and momentum balance of the lamella and bounding rim which gives an expression for the

dimensionless height of the drop and from conservation of mass yields the maximum diameter. However, agreement is within 20%. In Roisman [3], a semiempirical relation based on this methodology was presented and is expressed as

$$\beta_{max} = 0.87Re^{1/5} - 0.40Re^{2/5}We^{-1/2}. \tag{3.16}$$

Furthermore, Roisman et al. [34] show that the flow accompanying drop impact is universal for high impact We and Re. Roisman et al. [38] also accounts for the effect of receding and rebounding which will be discussed in the next section. For a further discussion of modelling, including the effect of solidification, see Bennett and Poulikakos [39].

The impact of water and glycerin on inclined smooth and wetted surfaces were studied in the work of Š. Šikalo et al. [40]. The critical We at which rebound occurs for a given impact angle was found to be constant if the normal velocity component is used in computing We. Effects of target curvature was studied in the work of Bakshi et al. [41]. From the film thickness developing over the target, they found three distinct temporal phases: drop deformation, inertia dominated, and viscous dominated. The first two phases were found to collapse onto each other for various Re and droplet-target combinations.

Numerical models have also provided insight into this problem, beginning with the earliest work where the full Navier-Stokes equations were solved using a Marker and Cell technique including the effect of liquid compressibility, Harlow and Shannon [42]. Bechtel et al. [43] used a variational approach beginning with an energy balance and solved for the height of the drop as a function of We, σ_{air}/σ_{lg}, and μ. Fukai et al. [44] used a finite element approach with a deforming grid and a Galerkin method with defining features including the occurrence of droplet recoiling and mass accumulation. Subsequently, Fukai et al. [45] improved upon this model with the inclusion of wetting effects, including hysteresis $\Delta\theta$. Pasandideh-Fard et al. [37] used a SOLA-VOF method and implemented measured values of dynamic contact angles

as boundary conditions. Furthermore, Bussman et al. [46] used a 3-D model on a symmetric surface geometry with a volume tracking algorithm to track the free surface. Inviscid, axisymmetric spreading including σ and a boundary integral method was implemented by Davidson [47]. Pasandideh-Fard et al. [48] modelled the fluid dynamics, heat transfer, and phase change of a molten drop impact and solidification. The motivation for modelling was applied to controlling solidification of liquid metals in solder deposition of printed circuit boards.

3.2.2 Rebounding

When a drop impacts a surface with low wettability with $We \gg 1$, the drop will recede and potentially lift off the surface due to increased liquid/gas surface energy. Mao et al. [2] systematically studied this phenomenon and developed a model to predict the onset of rebounding. Recently, the manufacture of micron and even nano textured surfaces spurred the use of these surfaces in impact experiments. Quéré [49] describes the nature of these surfaces in further detail. Richard and Quéré [50] studied the bounding of water drops on micro textured surfaces. Okumura et al. [51] later used scaling arguments to predict the contact time upon maximum deformation and developed a model describing the flow field inside the drop. Renardy et al. [52] focused on the shape of the drop upon impact and found that when $We > 1$ and $WeCa < 1$ the drop takes on pyramidal shapes upon impact then forms a toroidal shape followed by lift off. The impact of low viscosity drops on superhydrophobic surfaces predicted a dependence on the maximum diameter of the drop as $\beta_{max} \sim D_0 We^{1/4}$, where D_0 is the initial drop diameter, Clanet et al. [35]. The dynamics of the contact angle has received little attention although it is expected to be important for this unsteady process. Bayer and Megaridis [53] focused on the dynamic behavior of the apparent macroscopic contact angle, θ_D for partially wettable systems. Validation with molecular kinetics of Blake and Haynes [54] was shown. Most recently, Kannan and Sivakumar [55] used water drops impacting on stainless steel surfaces comprising

of rectangular grooves.

Modelling this behavior is complicated by the additional surface energy responsible for retraction of the drop. In Kim and Chun [56] an empirically determined dissipation factor is used to estimate viscous dissipation. The Oh is demonstrated to play the most important role in characterizing the recoiling motion. Using a level set approach, Caviezel et al. [57] developed a regime map for the conditions of rebounding and deposition.

3.2.3 Splashing

The interest in high speed impacts was applied to steam turbines and the aerospace industry in part to understand and prevent erosion of materials. Heymann [58] studied the impact of high speed liquid drops and determined parameters such as the impact pressure. Compressibility effects were explored further in the work of Lesser [59]. In these impacts a shock wave moves into the liquid and solid. In these scenarios the liquid is treated as an compressible inviscid fluid. Such compressible effects are highlighted in the works Lesser and Field [60], Lesser [59], Dear and Field [61], Field et al. [62], and Rein [14].

Here we focus our discussion on $We < 10^3$, neglecting liquid compressibility effects. We define the outcome of splashing when a drop disintegrates into two or more secondary droplets after colliding with a solid surface. The criteria appropriately defining a splashing threshold is determined by the conditions at which the transition from spreading to splashing takes place. From our experience in rain, we see that high impact velocities yield splashes which points to kinetic energy playing a pivotal role. The surface energy acts as a restoring force and enables drops to break off in pursuit of a minimum energy state. The ratio of these two forces points to the importance of the We in defining splashing criteria. Other relevant variables include drop size, surface roughness, ambient gas pressure, and surface compliance, etc. Expressed in dimensionless groups, the criteria necessary for splashing is commonly defined as

$K = f(WeRe^n)$ where the exponent n is determined through empirical correlations. The constant K is a function of the surface roughness and sets the value at which splashing or spreading occurs. The onset of splashing has been shown to depend on more than the fluid properties exclusively but it is still unclear how surface roughness plays a determinant role.

Stow and Hadfield [63] examined the splashing threshold of water drops. They found that drops spread without splashing as long as $RU^{1.69} < S_c$. S_c is a dimensional function of the properties of the liquid and the surface. In nondimensional form the relation can be written as $ReWe_c^2 < \epsilon$ where $\epsilon = f(R_a)$, where R_a is the roughness amplitude. Mundo et al. [64] studied the deposition/splash limit and determined it to be $K = OhRe^{1.25}$. For rough surfaces at high Re, splashing is observed through the corona splash event. For low Re on rough surfaces deposition was observed. Furthermore a value of $K > 57.7$ leads to incipient splashing where as $K < 57.7$ leads to complete deposition. Range and Feuillebois [65] found splashing to be independent of viscosity (< 10 cP) for low velocity impacts. The mechanism for the perturbations observed on the rim is explained by either surface roughness or a Rayleigh-Taylor instability.

Droplet trains were studied by Yarin and Weiss [66] and provided measurement of secondary droplets which provided good agreement with their model. Cohen [67] developed a statistical model to describe the shattering of a single drop into multiple daughter drops neglecting viscosity. Bhola and Chandra [68] determined the shape of molten wax droplets falling on surfaces of varying temperature finding that the substrate temperature was found to promote break up. A model based on Rayleigh-Taylor instability was used to predict the number of satellite droplets that broke loose upon impact. Furthermore, Aziz and Chandra [69] studied the impact of molten metal droplets on heated substrates exploring the effects of solidification as well. Bussmann et al. [70] simulated the fingering and splashing of a drop by introducing perturbations in the velocity of the fluid near the solid surface at a time shortly after impact.

Splashing may be enhanced when a drop collides obliquely with a surface or when a drop impacts normally on a moving wall, Bird et al. [71]. A theoretical approach to the determination of a splashing threshold was given by Cohen [67] which is based on the assumption that there exists a minimum radius for secondary droplets. Rein [14] believed compressibility may play a more dominant role in splashing and thus the Mach number must be included in analysis.

Rioboo and Tropea [13] delineated six different distinct outcomes following drop impact, the first being deposition as described earlier. The second is prompt splash where droplets are ejected directly at the contact line between the surface and the liquid. The third is the corona splash where a corona is formed during the spreading phase and eventually breaks into droplets. The receding break-up occurs when droplets are left on the surface during the retraction of the drop. Rebound occurs when the entire drop lifts off the surface and partial rebound when part of the drop stays attached to the surface. The unique descriptions of each distinct outcome are discussed in terms of individual properties as opposed to dimensionless groups. The two we will discuss in more detail are the prompt splash and corona splash.

Rioboo and Tropea [13] determined that the prompt splash is observed only with rough surfaces. This is attributed to the surface structure, namely the peaks which promote rupture and pinch off of thin ligaments formed upon initial spreading. The corona splash which is a more commonly seen splash in studies Range and Feuillebois [65], Bird et al. [71], Yarin and Weiss [66], is produced when the rim of the droplet turns upward and subsequently breaks off into drops. This outcome is more characteristic of drop impact on liquid films. Furthermore, the receding break up can be understood by wetting behavior. As the contact line recedes after reaching maximum spread, the dynamic contact angle decreases and when the minimum of $\theta_D = 0$ is reached the drops are left behind the bulk flow of the drop. It was concluded from his study that increasing the surface roughness, R_a, promotes a prompt splash. Increasing the impact velocity, U, also promotes a prompt splash and receding break up.

Recently it was shown by Xu et al. [72] that reducing the ambient pressure completely suppresses splashing. Furthermore, Xu et al. [73] showed prompt splashing to be initiated by surface roughness. For small drops deposition occurs and for large drops, corona splash is found on smooth surfaces with low surface tension liquids ($\sigma < 70$ dyne/cm). Corona splashing was explained by instabilities produced by surrounding gas, Xu et al. [73]. Moreover, Mandre et al. [74] demonstrated, by neglecting intermolecular forces, the liquid drop does not contact the solid, instead it spreads on a very thin air film. It is reasoned that the effect of viscosity acts to reduce probability of all disintegration mechanisms. The rate of the air film being squeezed out between the drop and solid surface has not been well characterized experimentally and should elucidate further it's role in controlling impact outcomes.

3.2.4 Micron droplet experiments

It is worth noting some experiments which utilized realistic size droplets in the context of industrial applications. Asai et al. [1] developed a simple correlation for the maximum spread of inkjet droplets on various printing surfaces providing good agreement. Schiaffino and Sonin [75] studied the molten droplet deposition and solidification at low Weber numbers. Through scaling arguments, droplet impact was divided into four regimes based on a We and Oh phase diagram. The divisions identified dominant forcing regimes depending on the strength of capillarity, viscosity, and inertia. The generation of these drops is complicated by non-isothermal conditions associated with their production. Attinger et al. [76] following this work and investigated the transient dynamics upon impact. The production of droplets is commonly created through the so called "drop-on-demand" mode. Recently, Basaran developed a method to significantly reduce the drop radius without reducing the nozzle radius in Chen and Basaran [9]. The key to forming drops with $R_d < R$ is to judiciously control the capillary, viscous, and inertial time scales that govern the flow within the nozzle and eject a drop. van Dam and Clerc [31] studied water drops of 18 and 42 μm on

glass substrates of varying wettability. In order to capture the dynamics upon impact of such a fast time scale $t \sim U/D \sim 10^{-6}$s, a delayed flash photographic technique was employed. Thus, the events from several drop impacts were sequentially ordered to observe the impact dynamics. The inherent assumption with this technique is that the impact is a highly repeatable event when the experimental conditions are precisely controlled. Higher spatial and temporal resolution was obtained by Dong et al. [77] using a pulsed laser and integrated with a imaging system. Furthermore, the drop-on-demand technique was expanded to the use of polymers in the work of Shore and Harrison [78]. Son et al. [79] studied the impact of water droplets on glass surfaces of varying wettability for $We = 0.05$-2 and $Oh = 0.017$. Following this study, the impact of Boger fluids, was observed in a range of $We = 2$-35 and $Oh = 0.057$. Tails were shown to follow the ejection of the droplet staying attached to the nozzle even upon impact, Son and Kim [10].

We are aware of only one study of the spreading of Newtonian and non-Newtonian drops which was solved numerically using the commercial code *Flow3D* Toivakka [80].

3.2.5 Complex Rheology liquids

To this point, the discussion on impact has only included single component liquids. More complex solutions as may occur in industrial applications is the focus of the work here and a review of the relevant topics associated with such fluids will be described.

Surfactant solutions were investigated in a series of works relevant to spray coating operations since the liquid/gas interface undergoes rapid adjustments over a short time scale. The importance of these types of solutions comes with the ability of reducing surface tension and thereby enhancing spreading. Additionally, the accumulation of surface active materials along the drop surface provides dynamic nature to the fluid interface and points toward the concept dynamic surface tension. Dynamic surface tension is a quantity commonly measured over a range of surfactant concentrations and typically decreases until a new lower equilibrium surface tension is reached. Sur-

factant solutions were studied in the work of Pasandideh-Fard et al. [37] where they explored the effect of equilibrium contact angle reduction. Surprisingly, they concluded that dynamic surface tension did not influence drop impact during inertia times. However, Mourougou-Candoni et al. [81] concluded that droplet retraction was drastically influenced by the adsorption kinetics of the surfactants which limited the return to the equilibrium surface tension, σ. In a subsequent publication, Mourougou-Candoni et al. [82] observed two types of retraction: a fast destabilizing and an exponentially decaying slow retraction. The works of Basaran's group also studied the effects of surfactants, and σ_d, and reasoned that the decreases in surface tension thereby enhances spreading, yet in opposition is the non-uniform distribution of surfactants along the fluid interface giving rise to Marangoni stresses inhibiting spreading, Zhang and Basaran [16]. Emulsions drew attention from Prunet-Foch et al. [83] and it was determined that emulsification plays a significant role in the existence and aspects of splashing and also the shape of the contact line instabilities.

Bergeron et al. [11] discovered, by adding very small amounts of flexible polymers to an aqueous phase, inihibition of droplet rebound on a hydrophobic surface is attained, thus allowing desirable deposition behavior with minimal alteration of shear viscosity. The inclusion of small concentrations of polymers isolates the non-Newtonian effect to normal stress effects which can be quantified through the elongational viscosity, which explains the increased resistance to droplet rebound. Following this work, Cooper-White et al. [84] group systematically investigated the role of elasticity on the dynamics of drop impact. The quality of a Boger fluid is that the shear viscosity remains nearly constant with shear rate thereby isolating the effect of the elasticity as the sole non-Newtonian feature. Worm like viscoelastic surfactant solutions were studied by Cooper-White et al. [84] with an outcome suggesting that lowering the equilibrium σ via surfactants normally offers little advantage over the time frame associated with impact, 5-10 ms for a 2-4 mm drop. Later, the effect of strain hardening was included in Cooper-White et al. [85]. A unique hydrodynamic

feature was included in Rozhkov et al. [86], where a polymer drop impacts a disc of diameter slightly larger than the drop. A splashing threshold was defined as

$$K_1 = \frac{\rho D^3}{\sigma t_{rel}} \times We^{3/8}, \quad K_1^* = 1140, \tag{3.17}$$

where t_{rel} is the relaxation time and when $K_1 > K_1^*$, splashing occurs. Four splashing regimes are discriminated in Rozhkov et al. [87]. Most recently, Bartolo et al. [12] derived an equation which identifies the elongational viscosity or more importantly, normal stress differences, for the reduction in rates of retraction and inhibition of rebounding behavior.

The impact and spreading of a neutrally buoyant suspension was investigated in Nicolas [88]. The study was conducted over a range of particle volume fractions and deduced that the particles are unevenly distributed throughout the drop with preference towards the outer portion of the drop forming an annular structure. Furthermore, for large Re, splashing was observed and explained by additive role of particles.

We were aware of only one study of the impact of yield-stress liquids. Nigen [89] used a commercial vaseline as the major test fluid. The final shape of the drop depends on when the yield-stress limit is reached in the spreading phase. Recently, however, Saïdi et al. [90] showed that for increasing yield stress, the spreading was inhibited and retraction of the spreading diameter was weakened.

3.3 Experiments

3.3.1 Overview

The following sections will cover our characterization and overview of experiments conducted using colloidal dispersions and equivalently viscous glycerol/water solutions over a range of parameters. Furthermore, our intention is to focus our study on pharmaceutical grade coating solutions and thereby understand the influence of colloidal dispersions in spray coating operations. These coating liquids are aqueous suspensions and are commonly defined by their solid content by weight. It

is noteworthy that the ratios studied here are realistic proportions for industrial scale coating operations. We will study three commercially available coating liquids from Colorcon, Inc. The three coating liquids are Opadry^{TM}II White differentiated by contents of partially-hydrolyzed polyvinyl alcohol (PVA), polyethylene glycol(PEG), hydroxypropyl methylcellulose (HPMC). The powders also consist of Lactose/TiO_2/Triacetin. The coatings are identified from here on by ID's #2, 4, and 5. Coatings #4 and 5 and differ by the addition of PEG. It is important to note that these coating powders do not include polymers in large concentrations and thus are different from previous studies described earlier Bergeron et al. [11], Bartolo et al. [12], Cooper-White et al. [84]. A summary of these coatings and their physical properties are shown in the next section. Coatings are prepared by slowly adding solid content to water over a magnetic stir plate. Care is taken to avoid aggregation of colloidal particles and obtain uniformity. The resulting liquid forms an aqueous suspension of colloidal particles. We will also use glycerol/water mixtures as a test liquids to compare the effect that the colloids have on spreading rates.

The target surfaces are tablets identified by ID's 03136, 03134, and 03135 corresponding to 0, 2, or 4 % hydrophobic lubricant. We will also use pure smooth surfaces as a benchmark for comparison with the results of the impact on tablets described in the next section. From here on we will discuss the coatings and surfaces by their ID defined above and the resulting Oh and contact angles produced. In all three studies we will characterize the effects by two parameters: The spreading diameter $\beta(t)$ and the centerline height of the drop $h(t)$. In this study we will provide fluid properties of coating liquids and then systematically study the impact on surfaces of varying wettability. The presentation of results will be divided into three sections: Experimental Setup, Data, and Analysis.

3.3.2 Setup and operation

Figure 3.4 is a schematic of our experimental apparatus. A high speed camera Phantom V12, Vision Research Inc., is used to visualize the impact of a drop from a solid surface. The magnification provides a spatial resolution of 17 μm/pixel and 1.45 μm/pixel for the mm and μm sized droplets, respectively. A long distance microscopic lens provided by Infinity USA Inc. is utilized in the micron sized drop impacts. The impact is backlit by an Edmunds fiber optic light source.

Single mm size drops are ejected by a syringe pump through a stainless steel needle (22g) and fall under their own weight with a diameter, $D \sim 2.5$mm. The vertical and horizontal diameters are measured and an equivalent diameter is calculated by $D_{eq} = (D_h^2 D_v)^{1/3}$. The droplets are approximately spherical with a maximum deviation between D_h and D_v of 10%. The impact velocities are measured between the two frames just prior to impact. Currently we are conducting uncertainty analysis on the velocity measurements over many realizations. For this study we are only concerned with order of magnitude estimates on dimensionless groups. The height of release is adjusted to obtain different velocities. The use of a piezoelectric sleeve bonded to a capillary tube of diameter 120μm provides drops of size $\mathcal{O}(60 - 80\mu\text{m})$. The piezo nozzle and voltage generator are provided by MicroFab, Inc. A close up of the piezo nozzle is shown in Figure 3.5. A typical waveform to eject droplets is shown in Figure 3.6. In a typical experiment, mm and micron drop impacts are recorded at 7600 fps and 60000 fps, respectively. In order to obtain greater temporal resolution, a higher speed camera is necessary to resolve short term dynamics. We investigate the parameter space defined in We and Oh shown in Figure 3.7. By working with such highly viscous fluids we are able to realize higher $Oh \sim O(1)$ thereby extending the range of previous studies. All quantitative data is collected with image processing software developed by NASA, Spotlight, Klimek and Wright [91].

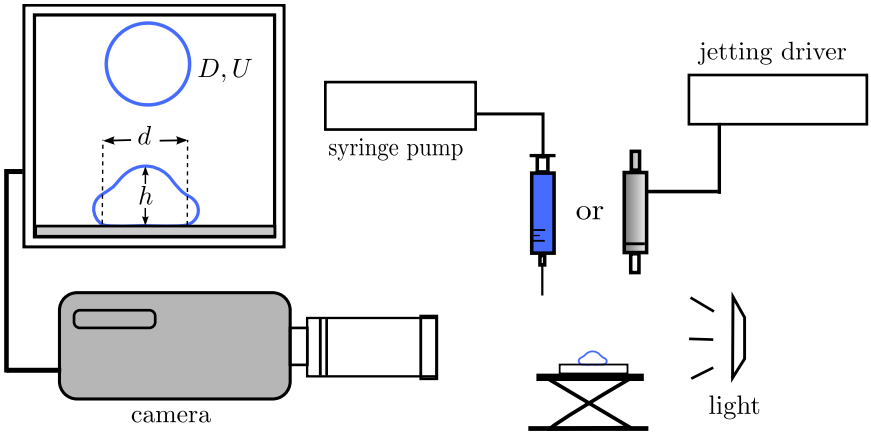

Figure 3.4: Schematic of experimental apparatus. Data extracted is spreading diameter $d(t)$ and centerline height $h(t)$

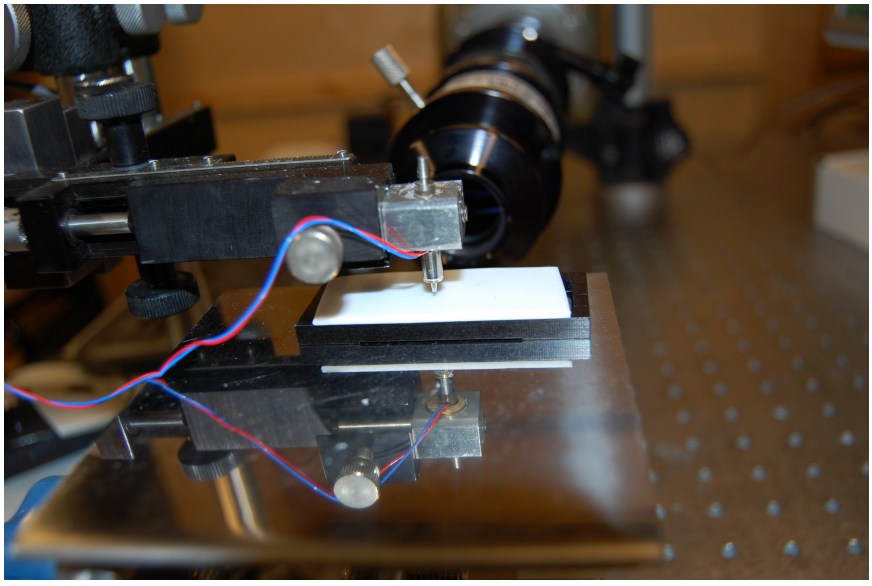

Figure 3.5: Photo of 120 μm diameter nozzle.

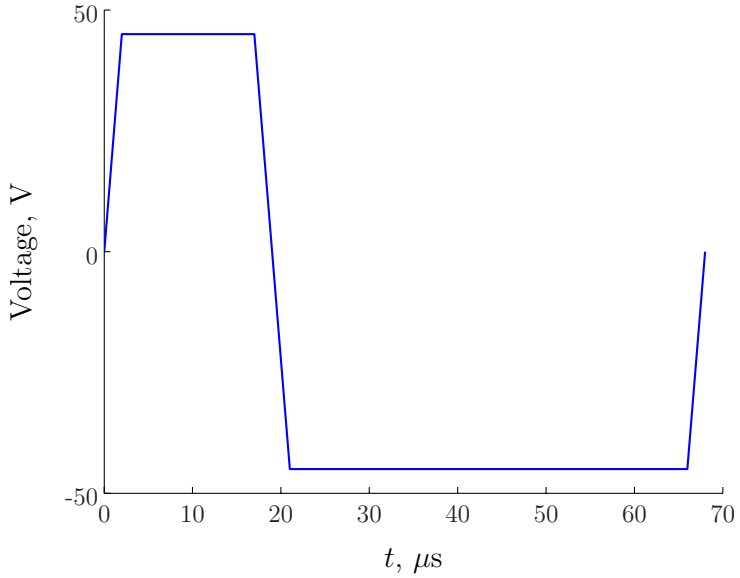

Figure 3.6: Typical waveform used to eject droplets from nozzle. Frequencies vary but range from 10-100 Hz.

3.3.3 Materials and Methods

Impact Surfaces

Table 3.1 summarizes the target surfaces utilized in this study. We have three tablet core substrates of varying hydrophobicity that are used as our impact targets as well as three ideal surfaces: acrylic, mica, and teflon. The tablets are composed of Microcrystalline cellulose or Magnesium stearate and are formed through by compression. The porosity of the tablets is altered by hydrophobic lubricant yet they still can be subject to capillary imbibition. The use of highly viscous coating suspensions prevents penetration for the coating suspensions but not for the glycerol/water mixtures. Three 'ideal' surfaces are chosen based on their matched wettability with coating/tablet combinations (see Table 3.2). Impact of glycerol mixtures is attempted only on ideal surfaces.

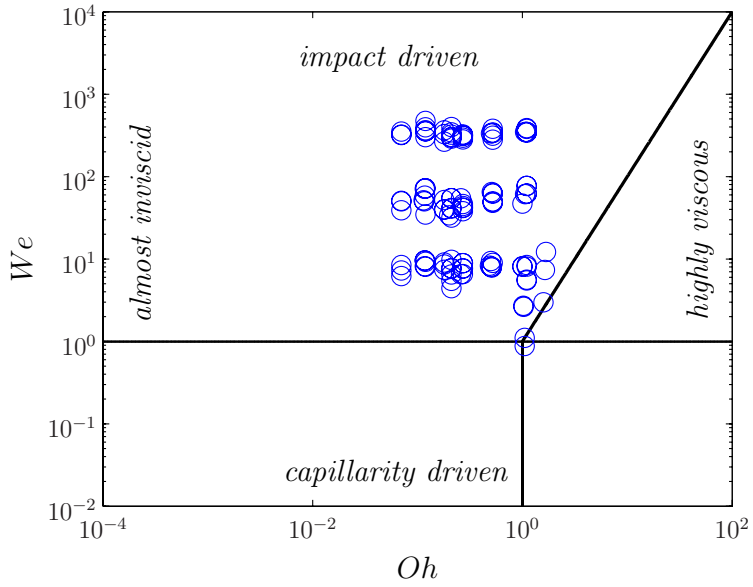

Figure 3.7: Regime plot impact study based on We and Oh

Rheology

Characterization of the coating suspensions was carried out through shear viscosity measurements. A Brookefield II Cone+plate viscometer and a Anton Paar MCR301 Rheometer with a double gap rheometer configuration was utilized. Figure 3.8 shows a typical viscosity measurement over a range of shear rates of 10^{-3}-10^{3}s^{-1} for #5.

The shear viscosity maintains a very slight shear thinning profile for all coating suspensions used in this study and thus the implementation of the shear viscosity at 1000 s^{-1} is a conservative estimation. The shear rates upon impact can range from 1-1000 s^{-1}, thus employing the lowest viscosity serves as a first order approximation and is used herein. The viscosity can be fit excellently to the form $\mu = m\gamma^{n-1}$ for $\gamma > 1$. Furthermore, the viscosity at 1000 s^{-1} versus increasing solid content obeys an power law function as observed in Figure 3.9. Assessing any non-Newtonian feature is difficult as the coatings are comprised of colloids of varying size and shape and ability to aggregate. It is proposed that using the shear viscosity is an appro-

Table 3.1: Summary of target surfaces and properties

Surfaces	notable properties
acrylic	Synthetic polymer, PMMA
mica	Silica mineral, molecularly smooth
teflon	synthetic fluoropolymer, PTFE
03136, 0% lubricant	100 % microcrystalline cellulose
03134, 2% lubricant	magnesium stearate
03135, 4% lubricant	magnesium stearate

Table 3.2: Summary of equilibrium contact angles from FTÅ200 measurement system

Fluid	mica	acrylic	teflon	3136	3134	3135
2, 20%, Opadry^{TM}II White, PVA/PEG	28	62	77	34	58	91
4, 15%, Opadry^{TM}II White, HPMC/PEG	15	54	75	33	62	87
5, 10%, Opadry^{TM}II White, HPMC	13	53	81	36	56	91
5, 12%, Opadry^{TM}II White, HPMC	13	49	75	40	70	92
5, 15%, Opadry^{TM}II White, HPMC	25	46	74	57	77	106
60% Glycerol/H_2O	7.5	66	94			
75% Glycerol/H_2O	13	75	92			
85% Glycerol/H_2O	16	70	93			

priate first characterization of these coating solutions. However we anticipate further characterization is necessary to gain quantitative understanding of the influence of colloidal particles in spreading. To date we are aware of only one quantitative study on the impact of a suspension of density matched particles Nicolas [88].

The surface tension is measured by our colleagues at UCSD with a du Nuoy Ring method and maintains a value approximately half that of water. Table 3.3 shows a summary of the fluid properties used to define dimensionless parameters.

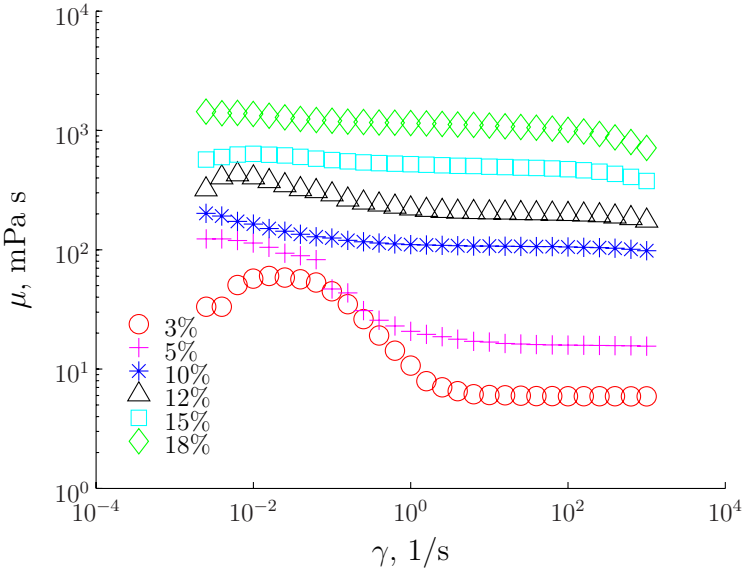

Figure 3.8: Shear viscosity of Opadry suspension # 5

Table 3.3: Summary of fluid properties

Fluid	μ, mPa·s @1000 s^{-1}	ρ, kg/m^3	σ, N/m	T, °C
2, 20%, Opadry^{TM}II White, PVA/PEG	39.35	1070	0.04393	25.4
4, 15%, Opadry^{TM}II White, HPMC/PEG	73.6	1040	0.04707	25.4
5, 10%, Opadry^{TM}II White, HPMC	98	1020	0.04822	25.4
5, 12%, Opadry^{TM}II White, HPMC	175	1030	0.04766	25.4
5, 15%, Opadry^{TM}II White, HPMC	377	1040	0.04667	25.4
60% Glycerol/H_2O	10.8[a]	1156	0.065	25.4
75% Glycerol/H_2O	35.5	1195	0.063[b]	25.4
85% Glycerol/H_2O	109	1220	0.062	25.4

[a]Viscosities for 60 and 75% glyc/water are extracted from properties table

[b]Interpolated value between 85% and 75% glyc/water

Micron droplet ejection

Although it was demonstrated that gravity has only a minor effect in droplet impacts, it was only validated for low viscosity liquids, with $Oh \sim 10^{-2}$, Dong et al. [92].

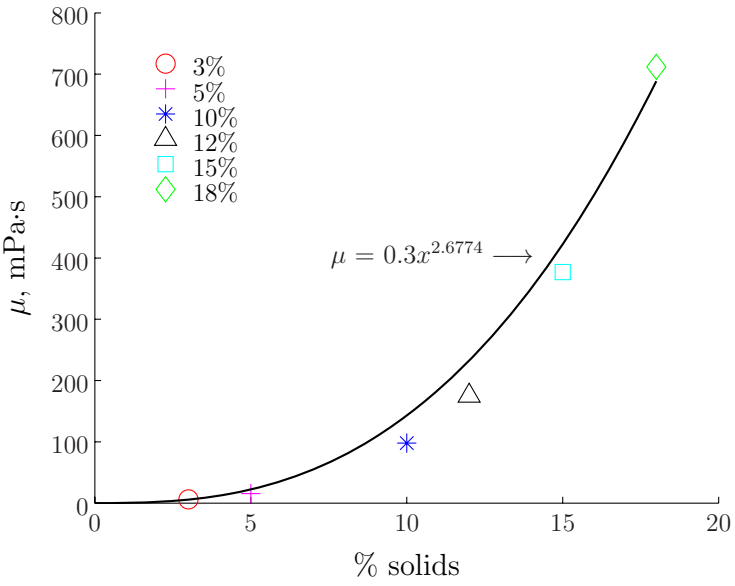

Figure 3.9: Shear viscosity of Opadry suspension # 5 taken at 1000 s^{-1} versus solid content.

We anticipate that gravity will also be negligible here, at least for μm size drops where $Bo \ll 1$. However, when mm size drops are employed then $Bo \sim 1$. Many authors justify neglect of gravity by introducing the Froude number expressed as $Fr = U^2/Dg \gg 1$ for both mm and μm size drops. This is not an accurate parameter to characterize the effect of gravity. The Fr characterizes the propagation of gravity surface waves against the convective fluid motion, whereas the key effect of gravity is to modify the overall shape of the droplet through the balance between potential, kinetic and surface energy.

Here we utilize viscosities of $\mathcal{O}(10^2\text{cP})$ thus obtaining $Oh \sim (1)$. Drop-on-demand technology has generally been motivated by the ink-jet industry, yet the need for developing polymer based electronics such as polymer LED's has provided a need to generate micron size drops of more complex rheology liquids Son and Kim [10]. Here we demonstrate that by applying a suitable waveform and frequency we are able to generate $30 - 80$ μm diameter drops with glycerol/water mixtures and coating #5,

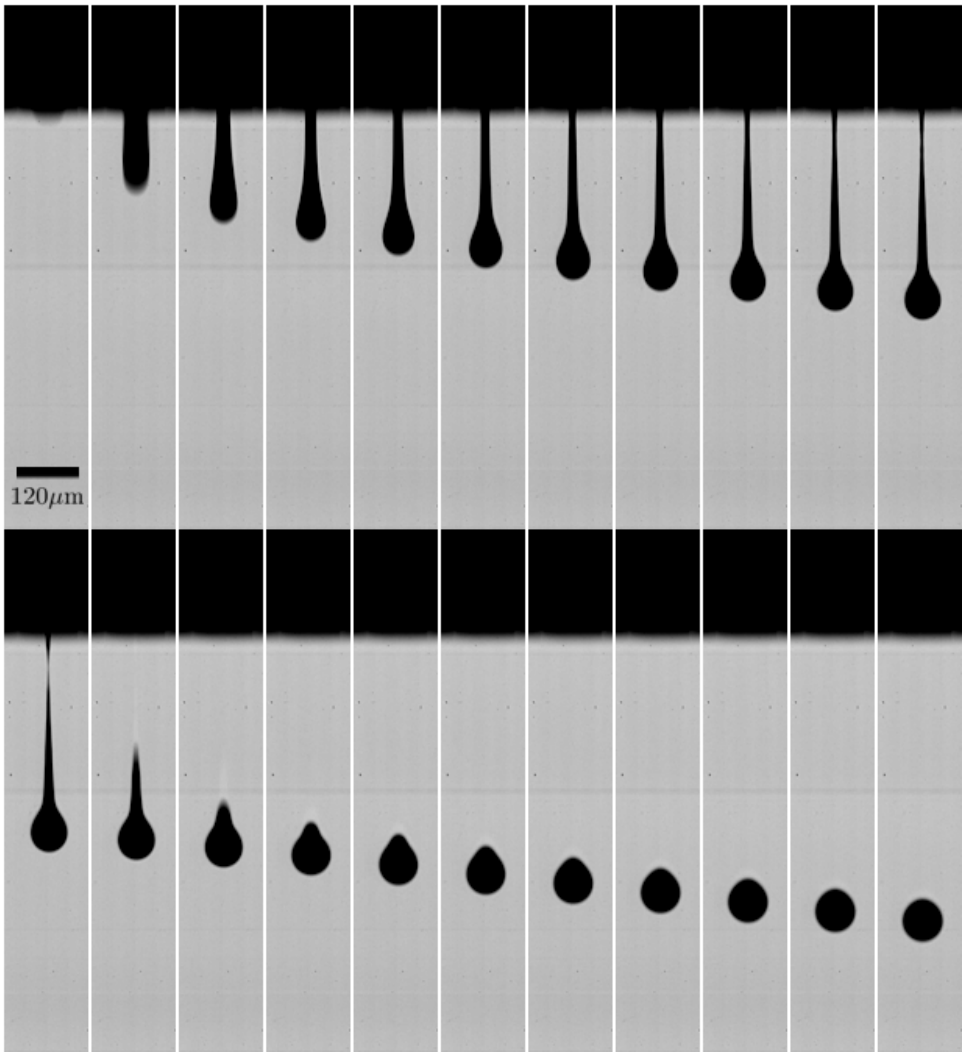

Figure 3.10: Ejection sequence of #5, 10%. Time interval between each frame is 31 μs

10% solids both having $\mu \sim 100$cP. A sample sequence of ejection of coating #5, 10% solids from the piezo nozzle is shown in Figure 3.10

At this point, the generation of micron sized droplets is produced at the expense of droplet speed and thus we are limited to $We \sim 1$. Furthermore, limited temporal resolution of our high speed technology precludes us from obtaining precise dynamic behavior of the impacted droplet. However, we are able to obtain the maximum

spreading diameter which will be highlighted later. The ejection of higher speed droplets will be the focus of future work. From here on we focus our attention on experiments from mm size drop impacts.

3.4 Results and Discussion

3.4.1 Analysis

Since the viscosities of the liquids we use in this study are high ($\mu > 10$cP), splashing and rebounding is absent under the range of impact velocities (0.4-2.5 m/s) studied herein. Therefore we are able to quantify the outcome in terms of the spreading regime and extract the spreading diameter and centerline height of the drop during initial impact times, $\sim D/U$. A typical impact sequence is shown in Figure 3.11. A drop of high viscosity impacts and jets a lamella around the periphery of the drop and attains a 'mushroom' like shape for a few instants. Given sufficient kinetic energy, the apex of the drop overshoots the height of the rim then either oscillates or dampens into a flat disc or a spherical cap at equilibrium. The contact line region undergoes sharp adjustments in slope depending on the speed of the contact line. The liquid/solid area rapidly dissipates any available energy and settles to equilibrium in a matter of a few ms. Figure 3.12 shows the dimensional results for spreading diameter and centerline height of the drop immediately following contact with the substrate. The general behavior of the spreading diameter, $d(t)$ follows a decaying exponential of the form $d(t) = d_{max}(1 - \exp[-ct])$, where c is presumable a function of fluid properties, e.g. surface tension, viscosity, etc. The centerline height also obeys a rapidly decaying exponential behavior for the first few ms and then slowly decays to equilibrium. From here on we will present the data in nondimensional form using the initial diameter and velocity of the drop D and D/U as the length and time scales, respectively.

The regime plot shown in Figure 3.7 describes the experimental space for $We \sim \mathcal{O}(1 - 400)$, $Oh \sim \mathcal{O}(10^{-2} - 1)$, $Re \sim \mathcal{O}(1 - 700)$, and $Bo \sim \mathcal{O}(10^{-3} - 1)$. This range captures the behavior of impact conditions in atomization experiments where impact speeds are $U \sim \mathcal{O}(1 - 10)$m/s. Noteworthy is the extension of $Oh \sim \mathcal{O}(1)$ which initiates a balance between viscosity and surface tension. From here on we will discuss the results in terms of these dimensionless groups. The spreading rate and

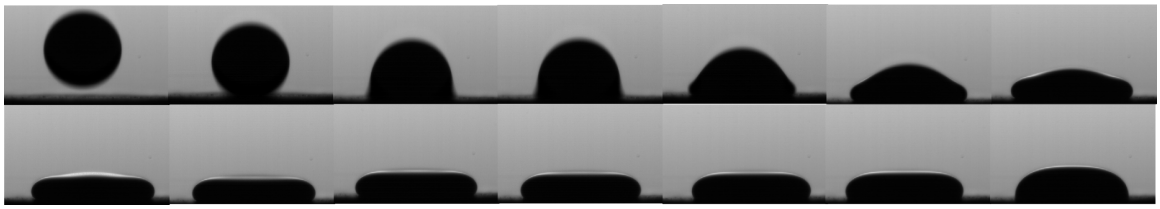

Figure 3.11: Typical impact outcome. Time interval between each image is 0.2 ms excluding the last image which occurs approximately 11ms after impact. Coating #5, 10% with $D \approx 2.5$ mm impacts tablet 03135 at velocity of $U = 2.47$ m/s

centerline height are expressed in nondimensional form as $\beta(t) = d(t)/D$ and $h(t)/D$, respectively (see Figure 3.4). Reproducibility of the following results are within 5% when comparing maximum diameters.

The focus of this effort will be divided into three parts. Firstly, we will characterize the behavior for three increasing amounts of solid content for a single coating. Secondly we will compare the behavior of the three coatings with varying solid contents. Finally, we will compare the coatings to three glycerol/water mixtures of similar viscosity to elucidate the effect of colloidal particles. For all studies, we will discuss the studies in terms of order of magnitude but for reference to exact parameters calculated see Table 3.4.

Study 1: Characterization of solid content of coating #5

Figure 3.13 demonstrates the effect of solid content (viscosity) on spreading. As the solid content is increased as seen through the $Oh = 0.3 - 1.1$ for corresponding weight percentages of 10-15%, the spreading history slows quicker and leads to a smaller resting diameter. Moreover, the viscosity decreases the spreading rate for all three We tested. Similarly, the height of the drop rapidly decreases until a dimensionless time $\mathcal{O}(1)$ and subsequently viscosity dampens the motion of the drop into a slow decay to equilibrium, Figure 3.14. In Figure 3.15 we observe very little impact of the percentage of lubricant in the substrate composition on the spreading behavior. This

Table 3.4: Summary of calculated dimensionless parameters from experimental set. Each of the colloidal dispersions is identified by (#), (% solids)

	2, 20%			4, 15%			5, 10%			5, 12%			5, 15%			60%/40% glyc/water			75%/25% glyc/water			85%/15% glyc/water	
	We	Oh	Re	We	Oh	Re	We	Oh	Re	We	Oh	Re	We	Oh	Re	We	Oh	Re	We	Oh	Re	We	Oh	Re
acrylic	35	0.12	49	10	0.21	15	8	0.27	10	9	0.52	6	8	1.10	3	7	0.02	105	6	0.07	35	9	0.18	16
	72	0.12	71	32	0.21	26	44	0.27	24	49	0.52	14	62	1.10	7	37	0.02	249	50	0.07	101	40	0.18	35
	355	0.12	157	322	0.21	87	320	0.27	66	342	0.52	36	347	1.10	18	268	0.03	665	320	0.07	253	265	0.18	89
mica	10	0.12	26	7	0.21	12	9	0.27	11	8	0.51	6	6	1.10	2	7	0.03	104	7	0.07	38	7	0.18	15
	59	0.12	65	55	0.21	35	42	0.27	24	65	0.51	16	77	1.10	8	38	0.02	252	39	0.07	88	52	0.18	39
	474	0.12	182	289	0.21	79	314	0.27	66	380	0.52	37	341	1.10	17	276	0.02	685	352	0.07	265	328	0.18	99
teflon	8	0.12	24	8	0.21	13	7	0.27	10	9	0.50	6	5	1.10	2	7	0.02	107	8	0.07	101	9	0.18	16
	72	0.12	72	55	0.21	35	42	0.27	24	62	0.52	15	77	1.10	8	37	0.02	250	51	0.07	101	40	0.18	34
	355	0.12	157	400	0.21	93	324	0.27	67	338	0.52	35	378	1.10	18	262	0.03	650	322	0.07	255	364	0.18	104
3134	8	0.12	24	5	0.21	11	7	0.26	10	8	0.49	6	8	1.00	3									
	71	0.12	70	34	0.20	28	54	0.26	28	48	0.52	13	61	1.06	7									
	396	0.12	167	303	0.21	85	296	0.27	62	313	0.52	33	347	1.06	18									
3135	10	0.12	26	4	0.21	10	9	0.27	11	8	0.50	6	8	1.00	3									
	50	0.12	61	41	0.21	31	47	0.27	25	50	0.52	14	47	1.00	7									
	366	0.12	161	299	0.21	83	311	0.27	64	281	0.52	33	347	1.10	18									
3136	9	0.12	26	8	0.21	13	8	0.27	10	8	0.51	6	8	1.10	3									
	52	0.11	63	42	0.21	32	38	0.27	22	63	0.52	16	62	1.10	8									
	301	0.12	145	344	0.21	89	282	0.27	62	334	0.50	36	388	1.10	19									

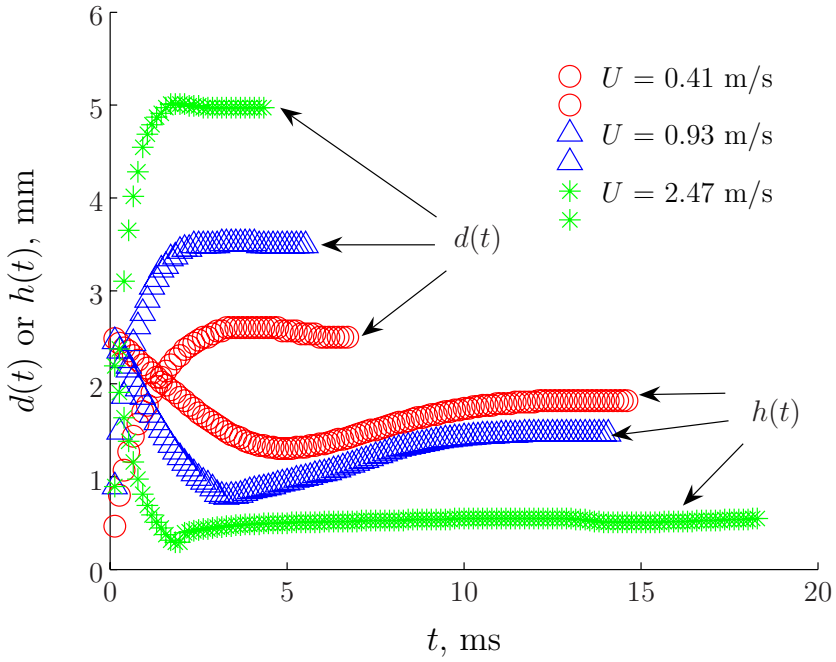

Figure 3.12: Spreading diameter $d(t)$ and centerline height $h(t)$ taken after moment of impact for three different velocities. Coating #5, 10% impacts tablet 03135.

was expected since we are only concerned with the impact dynamics for a dimensionless time of $\tau = Ut/D$ = 1-4 for $We \sim 300$. Decreasing the impact speed verifies this expected behavior only showing a slight difference as observed in Figure 3.16 for $We \sim 10$ where the interfacial energy at the solid/liquid area plays a more significant role. Increasing the solid content to #5 does not alter this trend as shown in Figure 3.17. To further verify this conclusion, we observe the outcome on the ideal surfaces and find enhanced spreading for acrylic and teflon surfaces compared to mica in Figure 3.18. It is reasoned that the higher surface energy of mica causes a delay during impact times. For $We \sim 300$, we see in Figure 3.19 acrylic shows faster spreading and confirms the negligible effect of wettability in early stages of impact. Comparison of the two remaining coatings, #4 and #2 will reveal any variation in colloidal behavior during spreading.

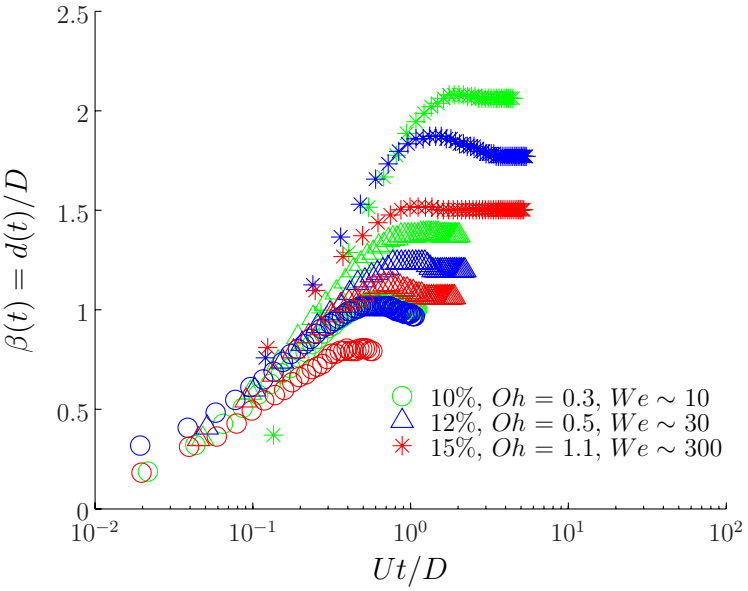

Figure 3.13: Spreading diameter, β of coating #5 (See Table 3.3) on tablet surface 03135 (4% lubricant). β versus time scaled with initial impact velocity U and diameter D. The colors green, blue, and red indicate 10, 12, and 15% solid content. The symbols $\bigcirc$, $\triangle$, and $*$ are for We of approximately 10,30, and 300, respectively.

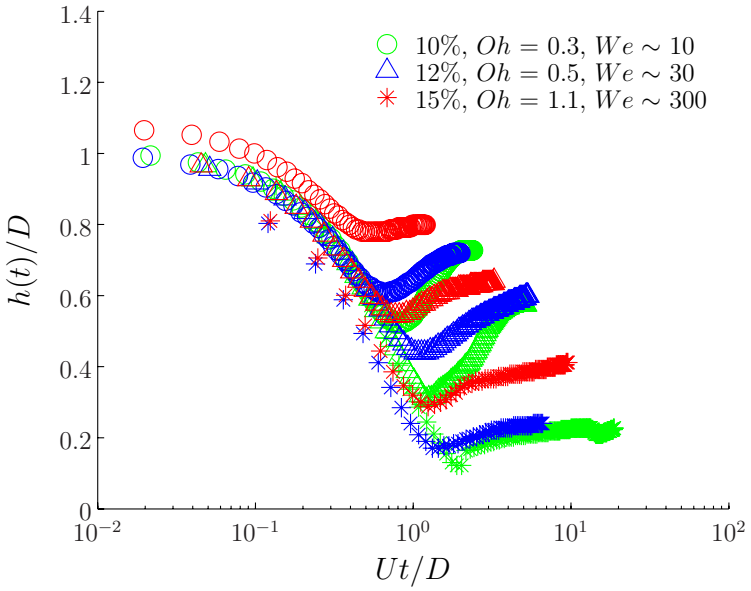

Figure 3.14: Centerline height, of coating #5 (See Table 3.3) on tablet surface 03135 (4% lubricant). $h(t)/D$ versus time scaled with initial impact velocity U and diameter D. The colors green, blue, and red indicate 10, 12, and 15% solid content. The symbols $\bigcirc$, $\triangle$, and $*$ are for We of approximately 10,30, and 300, respectively.

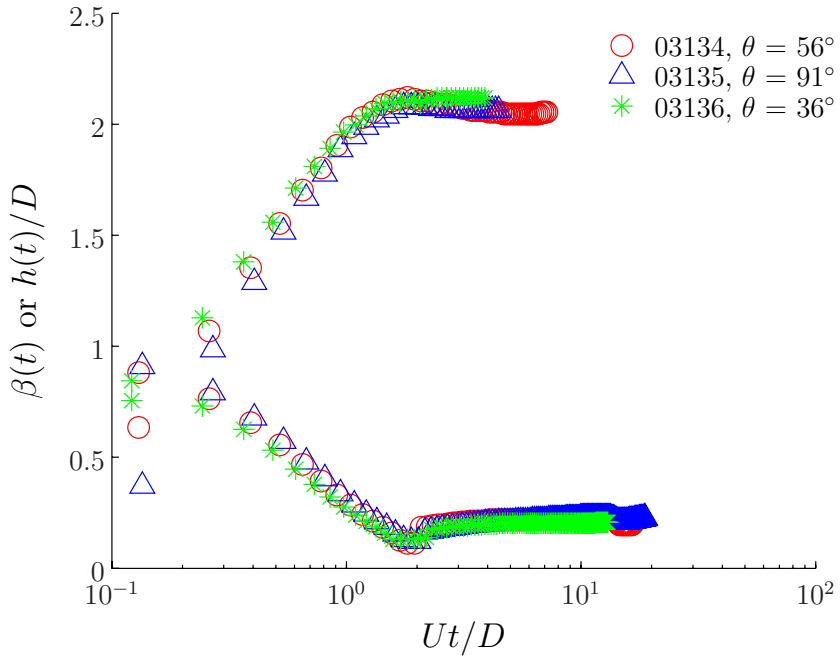

Figure 3.15: Spreading diameter and centerline height on tablets of differing wettability for $We \sim 300$ coating #5, 10%. Top and bottom set of curves describe β and h, respectively.

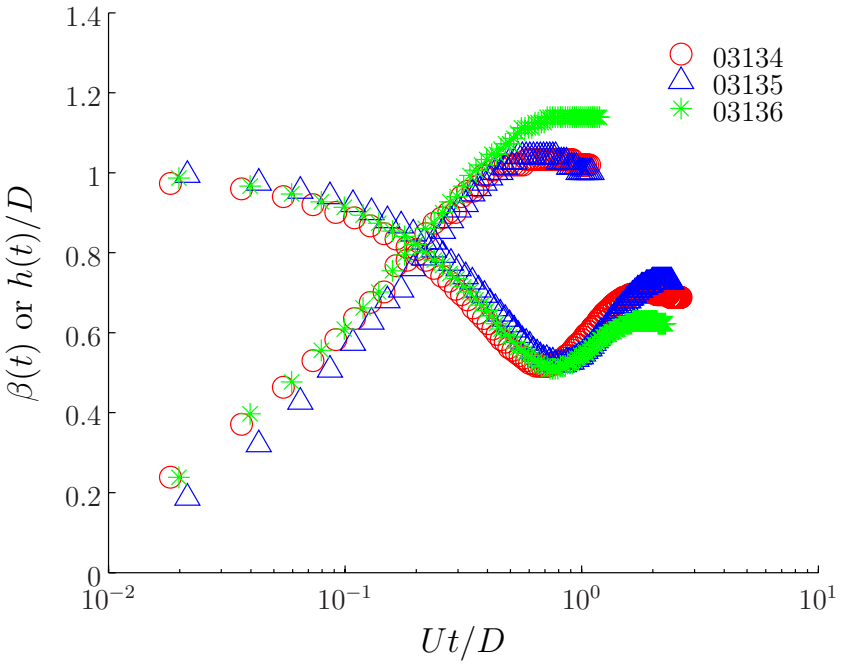

Figure 3.16: #5, 10%, Spreading diameter and centerline height on tablets of differing wettability for $We \sim 10$. Top and bottom set of curves describe β and h, respectively.

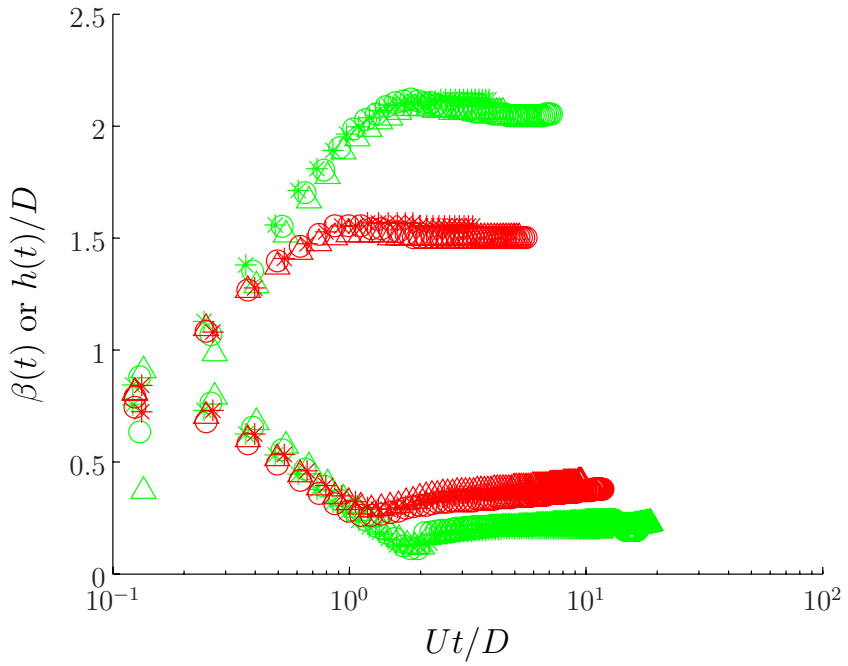

Figure 3.17: Spreading diameter and centerline height on tablets of differing wettability for $We \sim 300$. Top and bottom set of curves describe β and h, respectively. Green and Red sets of curves are for coatings #5, 10% and #5, 15%, respectively. The symbols $\bigcirc$, $\triangle$, and $*$ correspond to tablet surfaces 03134, $\theta = 56°$, 03135, $\theta = 91°$,and 03136, $\theta = 36°$, respectively.

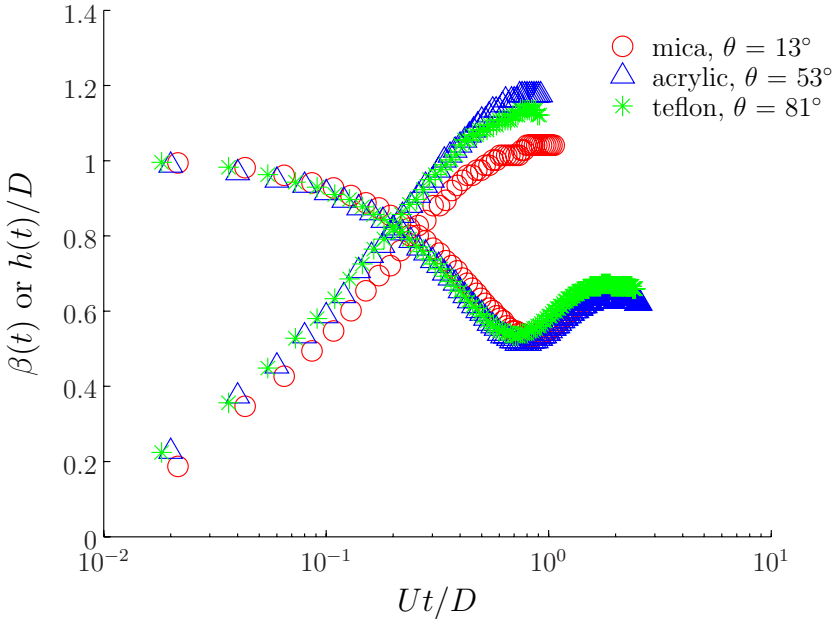

Figure 3.18: #5, 10%, Spreading diameter and centerline height on ideal surfaces of differing wettability for $We \sim 10$. Top and bottom set of curves describe β and h, respectively.

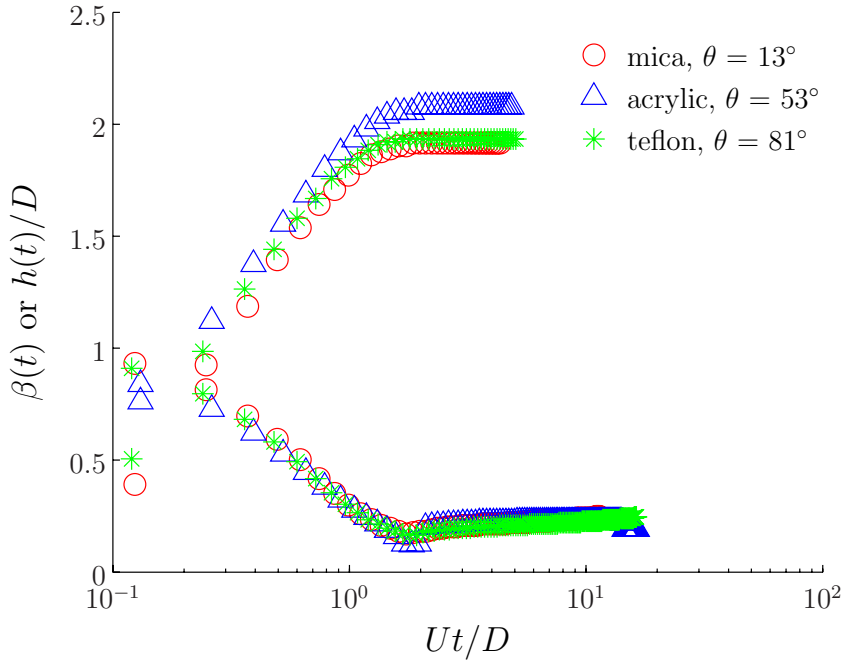

Figure 3.19: #5, 10%, Spreading diameter and centerline height on ideal surfaces of differing wettability for $We \sim 300$. Top and bottom set of curves describe β and h, respectively. Note that the slightly larger spread is observed on acrylic compared to mica but this is explained by statistical uncertainty between repeated tests.

Study 2. Comparison of coatings #5, 10%, #4, 15%, and #2, 20%

Comparing the three coatings on tablet 03136 (no lubricant) in Figure 3.20 we observe a slightly higher spread of coating #4 for $We \sim 10$ which is validated for $We \sim 300$ in Figure 3.21. This trend is consistent for tablets 03134 and 03135. It is reasoned that although the solid content is larger (15% compared to #5, 10%), the addition of PEG may enhance spreading in the early stage of impact by acting as a surfactant. Moreover, the colloidal particles of #4 may not provide increased resistance due to addition of PEG which is absent from #5. Furthermore, it is apparent in Figure 3.21 that coatings #2, 20% and #5, 10% follow similar paths despite the doubling of solid content and viscosities of 40 and 98 mPa·s, respectively. These two contradictory effects cancel out in the spreading behavior.

Examining coating #4, 15%, $Oh = 0.2$ in more detail, we observe diminished spreading and slight recession of the diameter for $We \sim 10$ shown in Figure 3.22. For $We \sim 30$, the centerline height overshoots the height of the rim and remains out of sight until it recovers over the rim and proceeds to go through two successively damped periods of oscillation. The linear portion which starts at 10^0 and ends approximately at 2.5 is the height of the rim data collected automatically from the image processing algorithm. The linear rise of the height of the rim (not the centerline) when the apex of the drop falls below is an unexpected trend and not previously documented to our knowledge. Note that this whole process occurs with an arrested contact line. This way of preserving conservation of mass is in opposition to the most common behavior where the decrease in centerline height is balanced by continued spreading until equilibrium is reached. Furthermore, the lack of this effect for $We = 300$ points toward a window of We where this behavior occurs.

If we compare the behavior of coating #4 on tablet and ideal surfaces we observe similar trends for all three tablet surfaces with the $\beta_{max} \approx 2.5$, Figure 3.23. Figure 3.24 demonstrates for $We \sim 300$, $\beta_{max} \approx 2.5$ on acrylic as opposed to mica and teflon

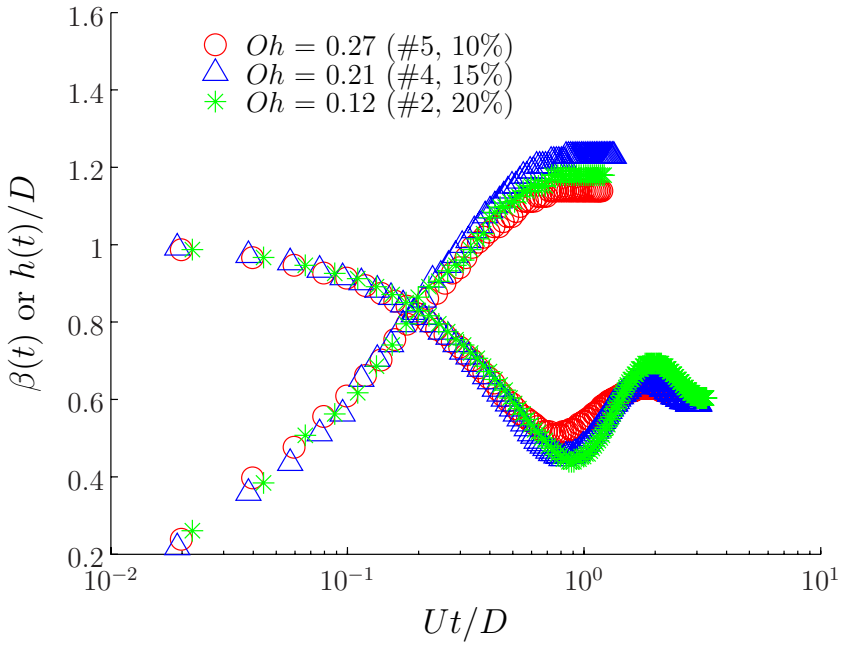

Figure 3.20: Spreading diameter and centerline height for coatings #5, 10%, 4, 15%, and 2, 20% for $We \sim 10$ on tablet 03136 (no lubricant). Top and bottom set of curves describe β and h, respectively. Note that coating 4 (Figure 3.21) spreads to larger area. We confirm this observation by looking at a higher We.

attaining $\beta_{max} \approx 2$. At this point we have not compared the effect of the coatings to Newtonian liquids. It will be apparent how dominant the role of colloidal particles are by comparing the spreading behavior for the glycerol/water mixtures and coating liquids at similar viscosities.

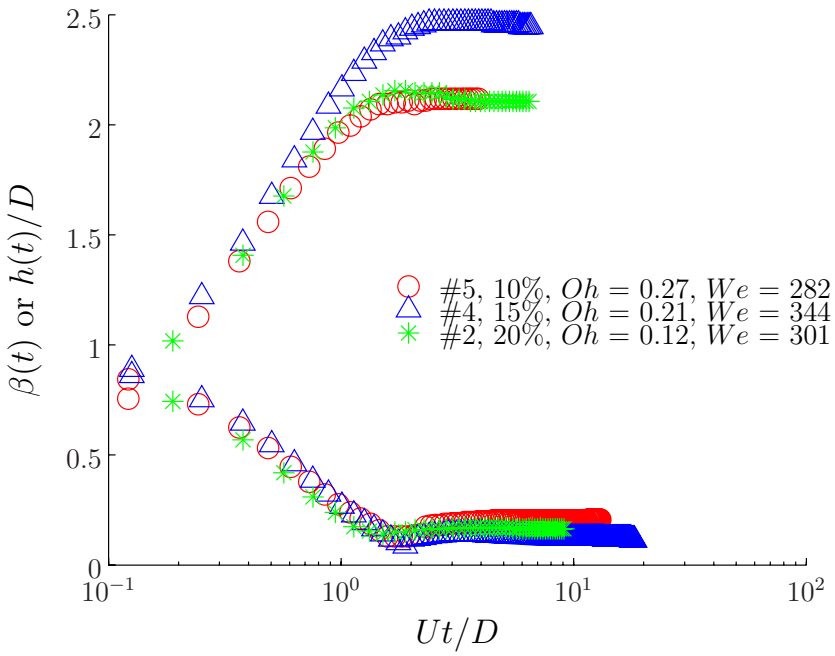

Figure 3.21: Spreading diameter and centerline height for coatings #5, 10%, 4, 15%, and 2, 20% for $We \sim 300$ on tablet 03136 (no lubricant). Top and bottom set of curves describe β and h, respectively. Confirm large spreading diameter for coating 4.

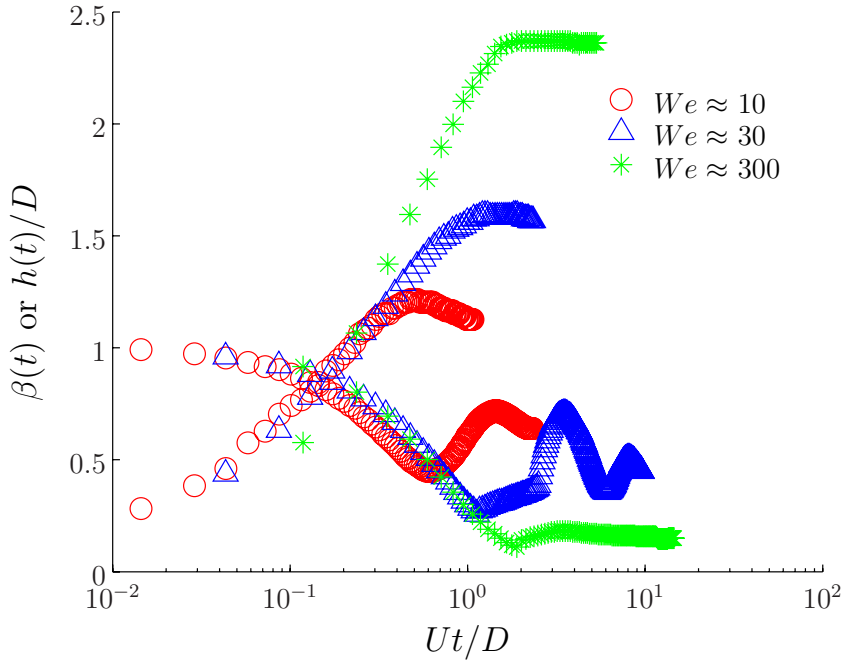

Figure 3.22: Spreading diameter and centerline height for coating #4, 15% ($Oh = 0.21$) on tablet 03135.

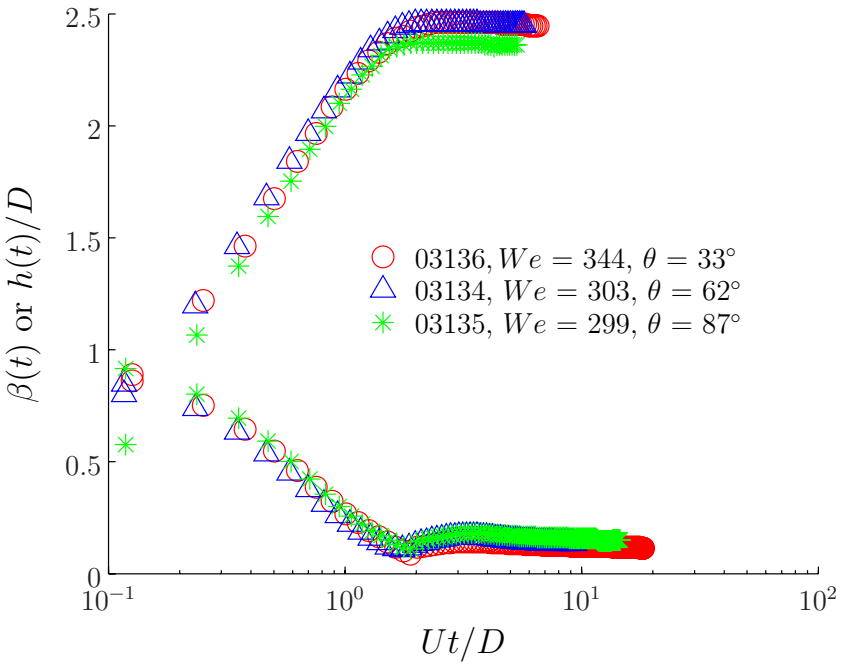

Figure 3.23: Spreading diameter and centerline height for coating #4 ($Oh = 0.21$) on tablets for $We \sim 300$.

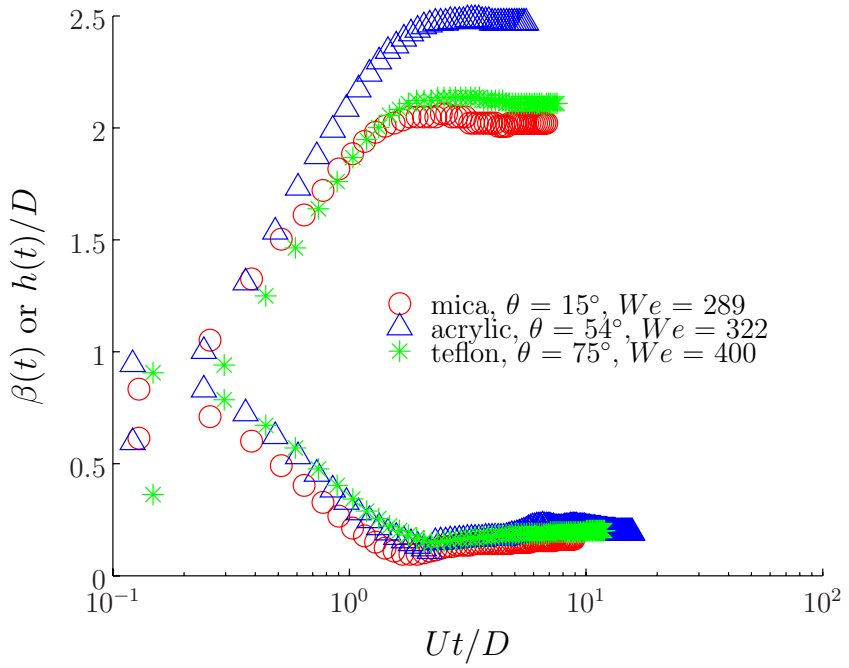

Figure 3.24: Spreading diameter and centerline height for coating #4 ($Oh = 0.21$) on idealized surfaces for $We \sim 300$.

Study 3. Comparison of coatings and glycerol/water mixtures

We compare the previous results to glycerol/water mixtures on ideal surfaces. Reduction in spreading rate is confirmed with the increase in viscosity as demonstrated in Figure 3.25. The role of the colloids have been understated thus far but it will be apparent if they affect the spreading rate by comparing the glycerol/water mixtures to coating liquids. Since 85% glycerol/water and #5, 10% have viscosities of $\mathcal{O}$(100 cP) we can compare their results over a range of We. Figure 3.26 demonstrates the expected behavior in the role of colloidal particles promoting increased resistance to spreading as indicated by slightly larger Oh. The further validate this assertion we compare two almost identical We and further observe reduced spreading for the colloidal dispersion #5, 10%, Figure 3.27. Similarly in Figure 3.28 for 75% glycerol/water and coating #2 we obtain increased spreading for the glycerol/water mixture which is further confirmed for almost identical We, Figure 3.29. It is important to note that following the impact time scale ($Ut/D \sim$ 1-4), the glycerol/water drops recede back to a shape obtaining contact angle equilibrium. Receding is minimal if even present for coating liquids which is explained by reduced surface tension compared to glycerol/water solutions and resistance of solid particles.

We have demonstrated that the colloidal dispersions show very a consistent difference in behavior with comparable pure Newtonian liquids. To further validate this observed behavior and verify the utility of previous models to include colloidal dispersions, we will compare our experimental results in the next section to two models that predict the maximum spreading diameter, β_{max}.

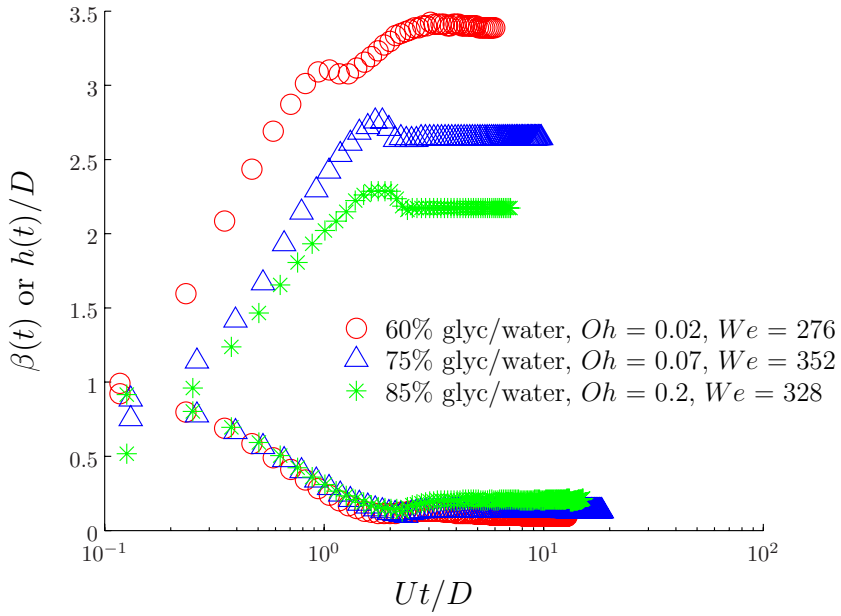

Figure 3.25: Spreading diameter and centerline height for glycerol/water solutions on mica, $We \sim 300$. $Oh = 0.02$, 0.07, and 0.2 for 60, 75 and 85% glycerol/water. Note the halt in the contact line followed by further spreading. Influence of viscosity is obvious, minimizing viscosity enhances spreading during impact times $\sim D/U$.

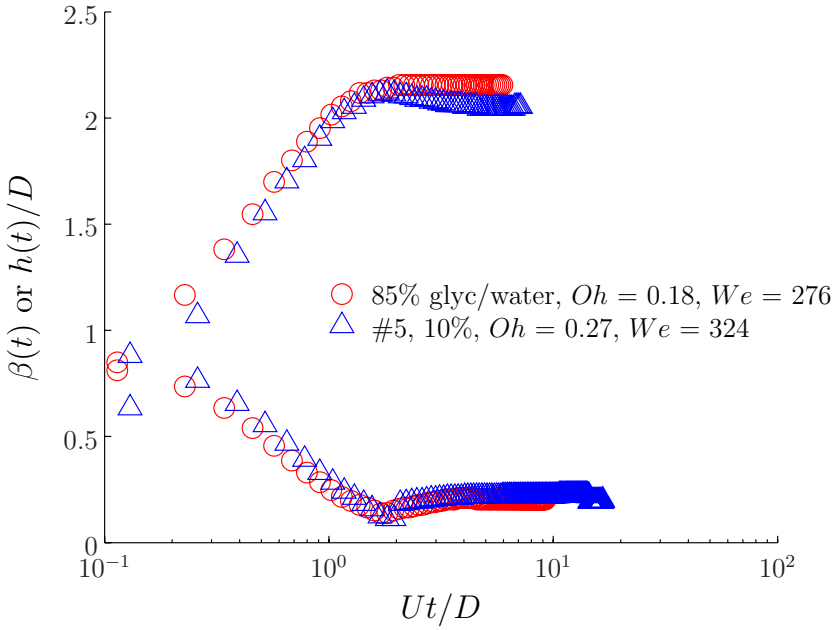

Figure 3.26: Spreading diameter and centerline height for glycerol/water solutions on teflon, $We \sim 300$. For 85% glycerol/water and #5, 10% the $Oh \approx 0.2$, respectively. General behavior follows an exponentially decaying function.

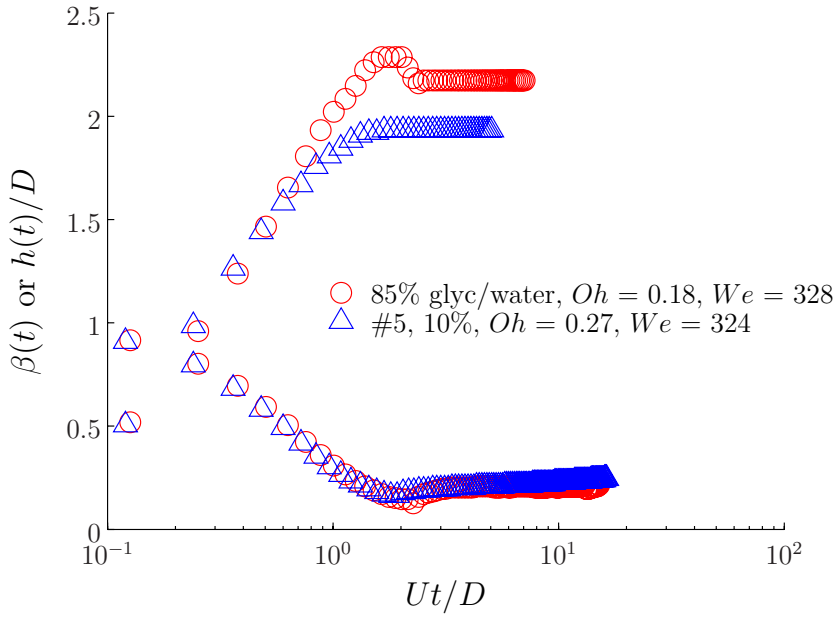

Figure 3.27: Spreading diameter and centerline height for 85% glycerol/water and #5, 10% on mica and teflon, respectively, for almost identical We and $Oh \approx 0.2$.

Study 4. Max diameter comparisons to models

The comparison of β_{max} extracted from the results shown herein and models of Mao et al. [2], Asai et al. [1], and Roisman [3] will demonstrate the utility of these models for colloidal dispersions. These two models are chosen here for comparison based on their simplicity and overall agreement with experimental data available in the literature. Figure 5.8 compares the experimental vs. predicted results using Eq. 3.15. It is apparent that the behavior follows reasonable agreement with predictions, within 12% when both glycerol/water and coatings are included together. When compared separately, glycerol/water is within 9% and the coatings are within 13%. Comparing the data with the model of Mao, Eq. 3.14, give slightly lower agreement with a total deviation of 13 % (11% glycerol/water and 13% for coatings) as seen in Figure 3.31. The simpler model of Asai that avoids the inclusion of the contact angle still provides better agreement. The model of Roisman [3] shows better agreement for larger drops

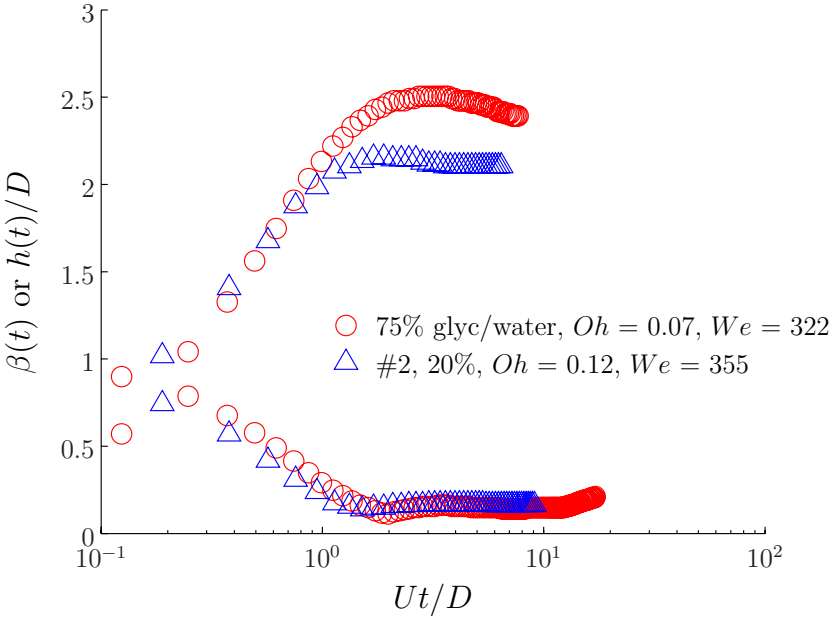

Figure 3.28: Spreading diameter and centerline height for 75 % glycerol/water solution and coating #2, 20% on teflon, $We \sim 300$. For 75% glycerol/water and #2 the $Oh \approx$ 0.07 and 0.12, respectively.

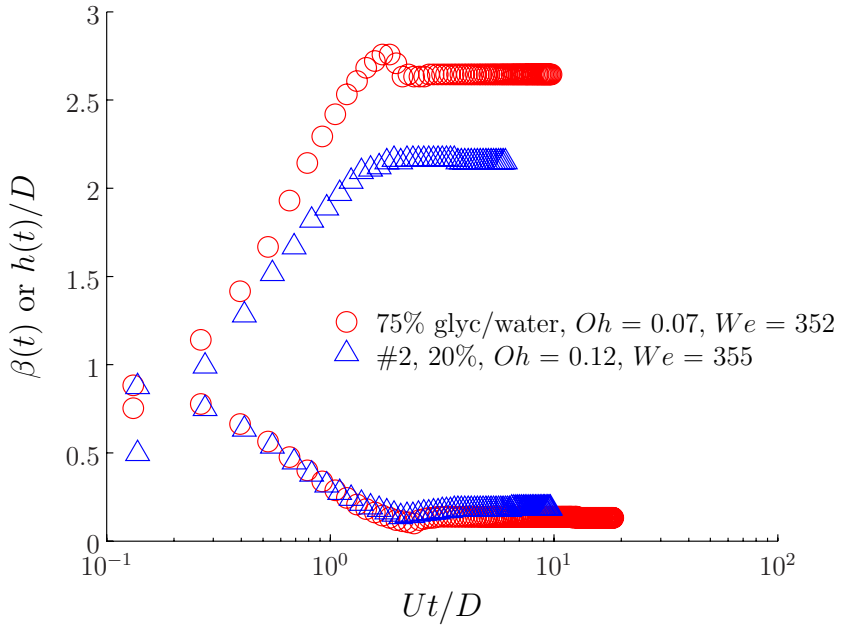

Figure 3.29: Spreading diameter and centerline height for 75 % glycerol/water solution and coating #2, 20% on mica and teflon, respectively, for almost identical We and Oh.

tested with approximately 8% error but deviates up to 50% for small drops at low We, Figure 3.32. This was anticipated, since the viscous stresses in the rim are neglected in the development and deserves further attention. These coatings are viscous dominated in these early stages of impact and require further analysis. This is expected as we show in Figure 3.33 how wettability has a negligible effect except for low We impacts ($< 2\%$) on the spreading and deposition during the initial stages of impact. Furthermore, in Figure 3.34 we show that our experimental results confirm the work of Clanet et al. [35] and verify that in this highly viscous regime, $\beta_{max} \sim Re^{1/5}$. All the models used to compare our experimental maximum spreading diameters β_{max} are semi-empirical. Thus by fitting our data to any one of the models could provide better agreement despite the fact that explicit effects of complex rheology are not won't be considered.

3.5 Conclusion

A systematic study of droplet impact was conducted with both canonical Newtonian fluids with high viscosity and liquids relevant to the pharmaceutical industry. Such liquids contain large quantities of insoluble solids and result in an aqueous suspension. At viscosities on $\mathcal{O}(10 - 100\text{cP})$ over a range of $We = \mathcal{O}(1 - 300)$, characteristic of spray coating conditions, we have demonstrated the outcome of drop impact results in a spreading outcome, avoiding splash and rebound, with only minimal recession of the spreading diameter. The role of viscosity observed with and without colloids is reasoned to explain the inhibition of splashing and rebounding. In other words, for increasing viscosity, a larger portion of energy is dissipated upon collision reducing the probability of an instability which can lead to rebounding and splashing. Furthermore, for intermediate We, we found an interesting behavior that has not been characterized for pure liquids. Specifically, in experiments with colloidal dispersions at $We \sim 30$, the height of the rim is found to increase linearly after the apex of the drop sinks below the rim as spreading is arrested, which is also observed for comparable glycerol/water

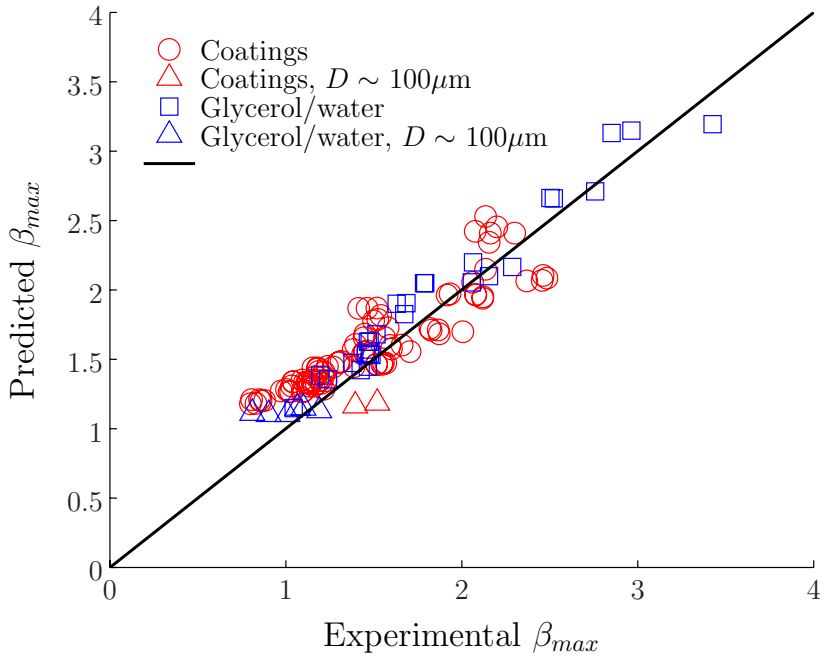

Figure 3.30: Summary of β_{max} diameters for all fluids tested at a time of 1-4 Ut/D versus model of Asai, Eq. 3.15. Red circles indicate coating liquids and blue squares indicate glycerol/water mixtures.

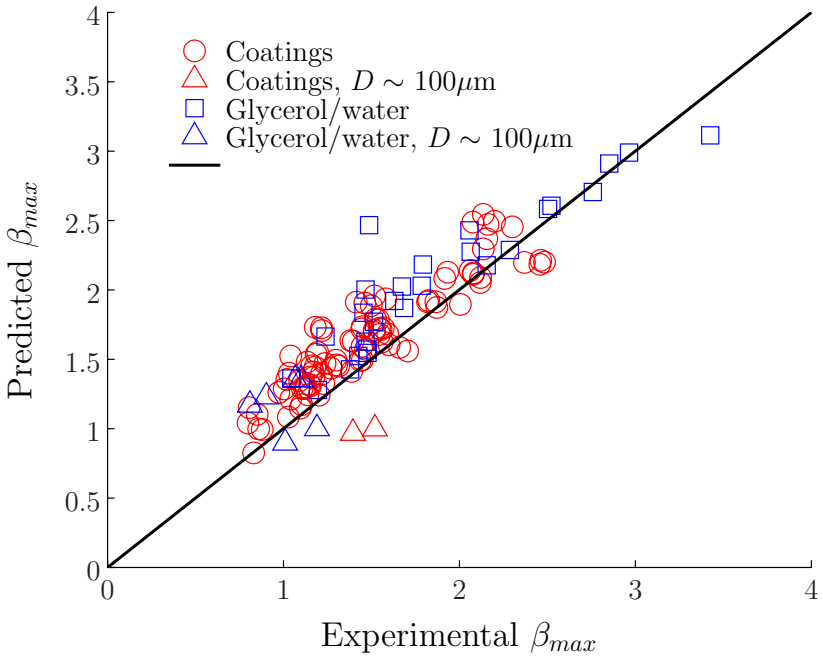

Figure 3.31: Summary of β_{max} diameters at a time of 1-4 Ut/D versus model of Mao, Eq. 3.14. Red circles indicate coating liquids and blue squares indicate glycerol/water mixtures.

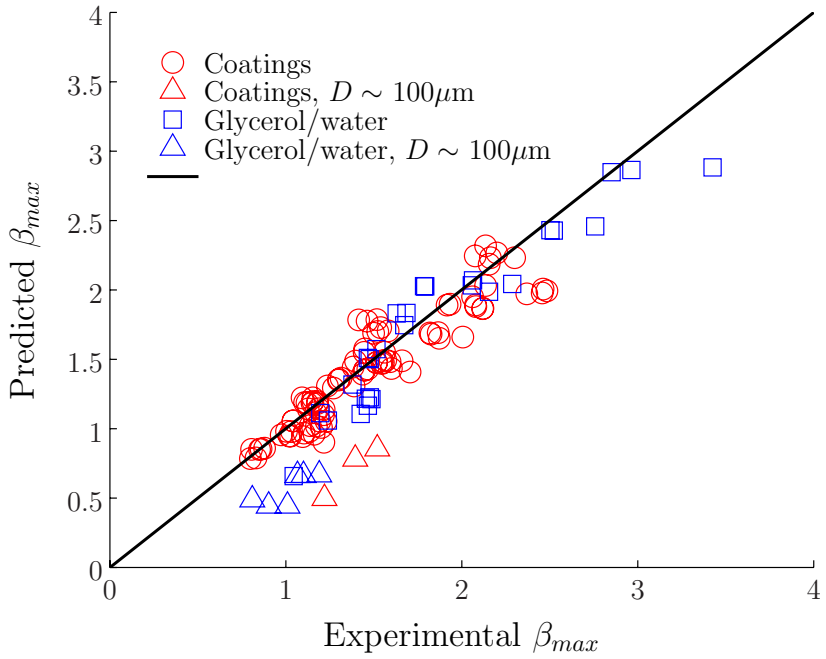

Figure 3.32: Summary of β_{max} diameters at a time of 1-4 Ut/D versus model of Roisman, Eq. 3.16. Red circles indicate coating liquids and blue squares indicate glycerol/water mixtures.

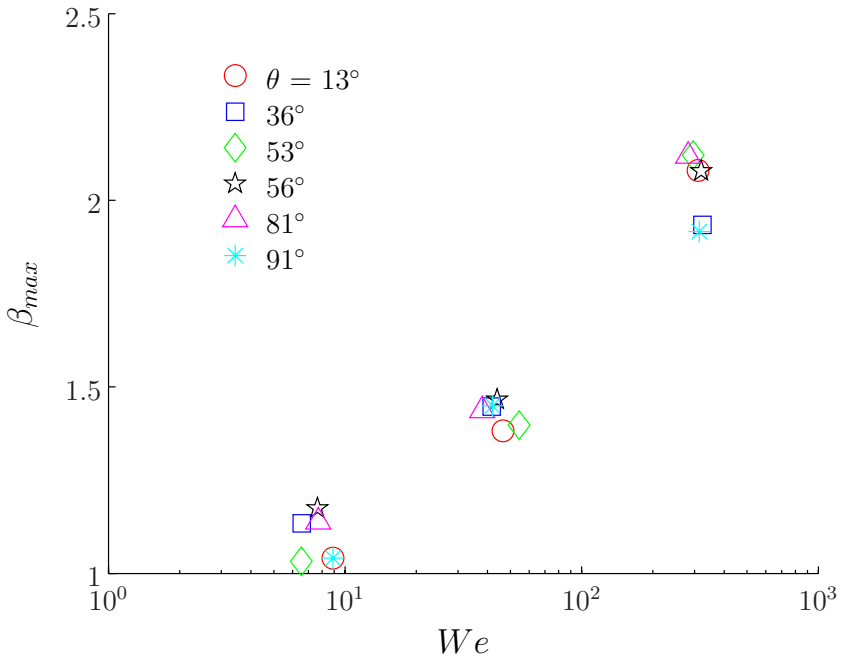

Figure 3.33: Effect of wettability shown for β_{max} vs θ. Since β_{max} is almost identical for $\theta = 13 - 91°$, the contact angle is shown to play a minor role in characteristic spreading times $Ut/D \sim$ 1-4.

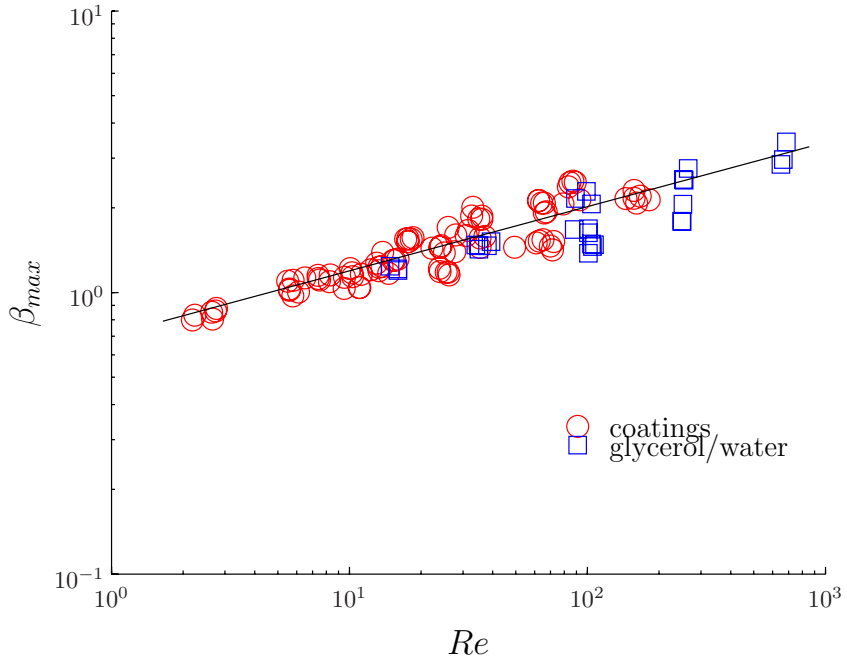

Figure 3.34: β_{max} versus Re for coatings and glycerol/water mixtures. The points are fit well to the solid line, $\beta_{max} \sim Re^{1/5}$.

mixtures.

We confirm previous studies that during the initial stages of impact, corresponding to $Ut/D \sim$ 1-4, the spreading diameter is insensitive to wettability. Furthermore, we observe reasonable agreement with three existing models for β_{max} for all We studied. Despite reasonable agreement, the effect of the colloidal particles is not included and may assist in providing better agreement. The utility of models of Asai et al. [1] and Mao et al. [2] still provide a robust model for first order approximations. The model of Roisman [3] provides the best correlation and points toward a more accurate method to modelling drop impact including the effect of particles. Additionally, we verify that the viscous regime obeys $\beta_{max} \sim Re^{1/5}$ even for the coating liquids studied herein.

This work stands to provide fundamental insight into aqueous colloidal suspension utilized in the pharmaceutical industry. We plan to investigate the impact for $We \sim 100$ of micron sized droplets and verify the results of the millimeter size experiments described herein. It is inconclusive to make any judgements about potential agreement. It is anticipated that small drops will be less likely to splash given the increased effect of viscosity, as characterized by larger values of Oh associated with smaller drops. The physical size of the drops should not change their behavior if the Oh is matched, unless there is another physical effect that we may not have taken into account. For small droplets, $\mathcal{O}(\mu\text{m})$, shear rates may be larger, for a given We number, and therefore non-Newtonian effects on viscous dissipation will be a larger percentage of the energy partition. In order to keep We constant, we need to increase U^2 as D goes down. Moreover, since the shear rate is proportional to U/D, higher shear rates will be present and may induce different effects for comparable We. These topics will be a subject of future investigations.

Chapter 4

SPONTANEOUS SPREADING OF COLLOIDAL DISPERSIONS ON HYDROPHILIC SURFACES

When liquid drops impact and spread on a solid substrate, the dynamics of spreading are initially dominated by the inertia the drop carries to the surface. Following this rapid spreading regime, the liquid may continue to spread out until Young's equation $\cos\theta = (\sigma_{SG} - \sigma_{SL})/\sigma_{LG}$ is satisfied. In this regime the spreading is controlled by capillarity and resisted by viscosity. Pure liquids have been common test fluids in prior studies, yet most industrial coating operations use highly viscous liquids with insoluble solids, i.e. colloidal dispersions. Here we study colloidal dispersions with viscosities $\mu \sim 100$ cP on nearly wettable substrates. Realistic sized drops created from sprays are deposited at $We \sim$ 1-10. These drops impact and spread first due to inertia and then by capillarity. In this transient regime immediately following inertia driven spreading events we observe the that equivalently viscous colloidal drops spread faster than pure Newtonian solutions. Specifically, in this transient regime, the spreading diameter of colloidal drops is found to follow a robust power law, $d(t)/D = C(t/\mu D\sigma)^n$ where C is an $\mathcal{O}(1)$ constant and $1/7 \lesssim n \lesssim 1/5$. These results are particularly relevant for pharmaceutical industries but are relevant to spray coating processes utilizing complex viscous rheology.

4.1 Introduction

When a drop of water is placed on a substrate, the drop may spread out completely into a thin film, spread to a finite area, or rest on the surface like a solid sphere. The resulting outcome is set by the net interactions between the liquid and solid surface,

namely, the polarizabilities (net attraction) of the liquid/solid pair at the intersection of the three phases: liquid/solid/gas. The balance between these forces is described by Young's equation $\sigma \cos\theta = \sigma_{sg}$ - σ_{ls}, where σ is the interfacial tension between the liquid/gas surfaces, σ_{sg} and σ_{ls} are the tensions for the solid/gas and liquid/solid interfaces, and θ is the equilibrium contact angle. Solid surfaces that maintain high concentrations of apolar molecules like Fluorine, i.e., teflon, resist interactions with water molecules, and water droplets rest on the surface in a hemispherical shape with contact angles $\theta = 110°$. Liquids with contact angles $\theta \approx 0°$ completely spread or 'wet' to a thin film. For these completely wetting scenarios, the spreading diameter evolves as $d(t) \sim Ct^{1/10}$, where C is a function of liquid properties. This expression is first attributed to Tanner and is commonly referred to as Tanner's law, Tanner [26] which has been validated experimentally by several investigators, Chen [27], Rafaï et al. [28]. These experiments are typically conducted over characteristic times on the order of a minute. In realistic spray coating applications where drops are micron sized, the time scale for spreading is less than a second before evaporation dominates. Hence the short term dynamics must be well characterized to validate Tanner's law for varying scales.

Tanner's law is restricted to fully wetting scenarios and small drops, typically smaller than the Laplace length $\ell = \sqrt{\sigma/\rho g}$ ($\ell = 2.67$ mm for water). However, neglecting gravity entirely by satisfying the inherent restriction set by the Laplace length may not be sufficient to ignore gravity effects if $D \sim \ell$ where D is the diameter of the drop. The Bond number $Bo = \rho D^2 g/\sigma$ gives a better indication of the balance between gravity and surface tension. For water drops with $D \sim 2$ mm, the $Bo = 0.5$. Thus, it is not completely evident that gravity can be entirely ignored. It has been shown that for drops where $\ell/D \gtrsim 1$, $d \sim t^{1/8}$ both experimentally and theoretically, Middleman [7]. For drops of size $\mathcal{O}(10 - 100\mu m)$ where $\ell \ll 1$ and $Bo \ll 1$, the validity of Tanner's law should hold. Yet few studies have had the capability of creating sufficiently small drops (100μm) to validate this assertion. Drops that are

micron sized are realistic for industrial spray coating processes yet there are few studies that investigate the impact and spreading events of this range, Yarin [15]. Additionally, most studies have neglected to study these spreading events over time scales ($\mu D/\sigma \approx 0.17$ ms) relevant to industrial spray coating operations which is relatively fast for most standard imaging technologies. Here we explore a range of parameters that scans both the effects of complex rheology and micron-sized droplets spreading on solid surfaces.

The nature of these aqueous colloidal dispersions makes them unamenable to theory of dilute hard sphere rheology such as the models first developed by Einstein and Krieger-Dougherty, (see Stickel and Powell [93] for a review). The volume fractions studied herein are significantly higher than those studied in dilute concentrations, leading to shear viscosities $\mu \sim \mathcal{O}(10 - 100\text{cP})$. An important quality of these dispersions is that the particles are fully wet by the dispersion medium. Moreover, the particles form aggregates but can be broken down during shearing events.

When these micron-size viscous colloidal dispersion drops are gently placed on a wettable substrate the drops spread to a finite diameter. When the film thickness reaches values as low as $h \sim \mathcal{O}(100\text{nm})$, van der Waal's forces are dominant, Israelachvili [94]. These forces act to destabilize the film and can lead to rupture and hence nonuniformity in film coatings. This can be particularly relevant near the edges of the drops. The dynamics at the edge of the drop continues to draw significant theoretical and experimental attention mostly due to the need to alleviate the infinite stress singularity at the contact line, de Gennes [21]. A review of various approaches to remove this singularity has been summarized in Eggers and Stone [95]. Primarily, these studies have focused on completely wetting scenarios of single phase liquids. Recently, the spreading of a nanoparticle laden drop was numerically modelled and showed contact line pinning and stair-like formations near the edges, Craster et al. [96]. Particle laden drops were also studied numerically by Jeong et al. [97] and were shown to resist spreading compared to single phase liquids and were reasoned to be

inhibited by variations of shear rates, the angular velocity of particles and kinetic energy of the drop.

Here we describe the early spreading dynamics of capillary driven colloidal dispersion drops on nearly fully wettable substrates. Obtaining measurements of these moving contact line scenarios using high volume fraction colloidal dispersions has not been reported previously, to the best of our knowledge. Exploring the dynamics of micron-size droplets spreading may shed more light on these and other moving contact line scenarios.

4.2 Theory

When a drop is deposited on a surface from a syringe, the drop makes contact with a substrate at negligible inertia, $We \leq 1$. If the drop is ejected from the syringe with considerable inertia, then the drop will spread to a diameter in a characteristic time scale of the order U/D and will continue to spread until the contact angle reaches equilibrium. The higher the impact speed the larger the contact area the drop will cover in this inertia-dominated phase. The dynamics are well described by the $We = \rho U^2 D/\sigma$ and the $Oh = \mu/\sqrt{\rho\sigma D}$ and these ratios will provide an indication of the initial conditions in our drop spreading study. Here, we characterize our drop spreading dynamics over a range $We \approx 0-10$ and $Oh \approx 0.1-1$, (Figure 4.1). In this regime we expect a balance of capillarity with inertia and viscosity. From dimensional analysis, we expect the spreading radius to be related to inertia and viscous time scales as

$$\frac{d(t)}{D} = f\left(\frac{t}{(\rho D^3/\sigma)^{1/2}}, \frac{t}{\mu D/\sigma}, \theta\right), \tag{4.1}$$

where D is the radius of the drop. The dynamics in this range of parameters was highlighted in the work of Schiaffino and Sonin [75]. When capillarity balanced inertia, the time scale is $t_{iner} \sim (\rho R^3/\sigma)^{1/2}$ and when capillarity is resisted by viscosity $t_{visc} \sim \mu R/\sigma$. The boundary for these events is not completely defined through analysis alone. In other words, when $Oh = 1$, viscosity is said to balance the surface

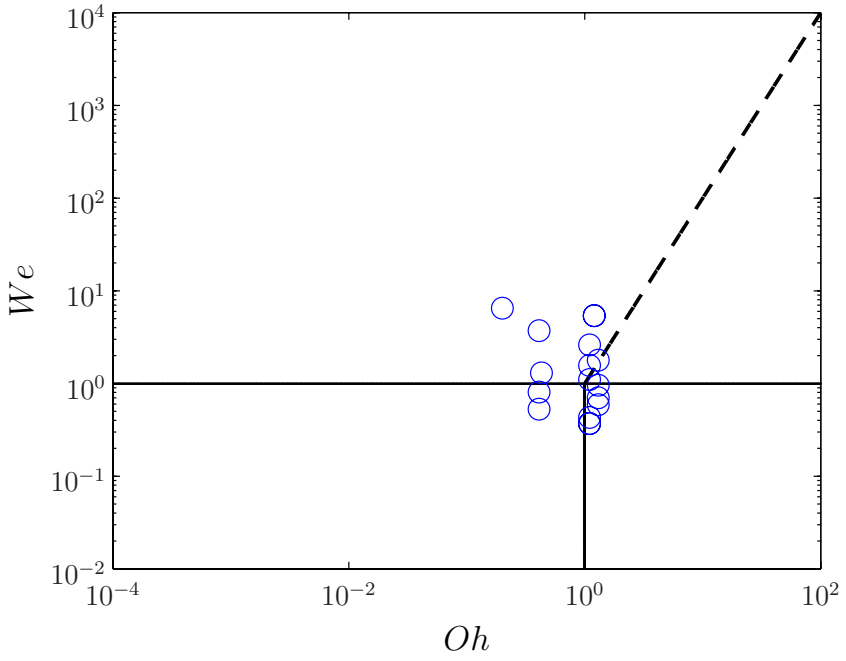

Figure 4.1: Phase plot of experimental study. The dashed line indicates when $We = Oh^2$. Note that dimensional analysis indicates a regime when inertial, viscous, and capillary forces are in balance.

tension. However, recall that dimensional analysis makes no claim of the order of magnitude of coefficients for a given relationship, i.e. $d(t)/D = C[t/(\mu D/\sigma)]^n$ where C and n are experimentally extracted coefficients. These coefficients can vary in orders of magnitude and hence dramatically affect the transition from inertial to viscous dominated spreading, $\mathcal{O}(Oh = t_{visc}/t_{iner})$.

The dynamics of drop impacts and spreading surrounding the boundary of $We \approx 1$ and $Oh \approx 1$ will be studied to elucidate if the scaling based on dimensional analysis is valid in this regime. These colloidal drops spreading experiments are characterized experimentally in terms of the spreading diameter $d(t)$ and film thickness $h(t)$ at early times $\sim \mu D/\sigma$ described in Section 4.3. Section 4.4 outlines the results from this study and demonstrates that the spreading diameter follows a robust power law.

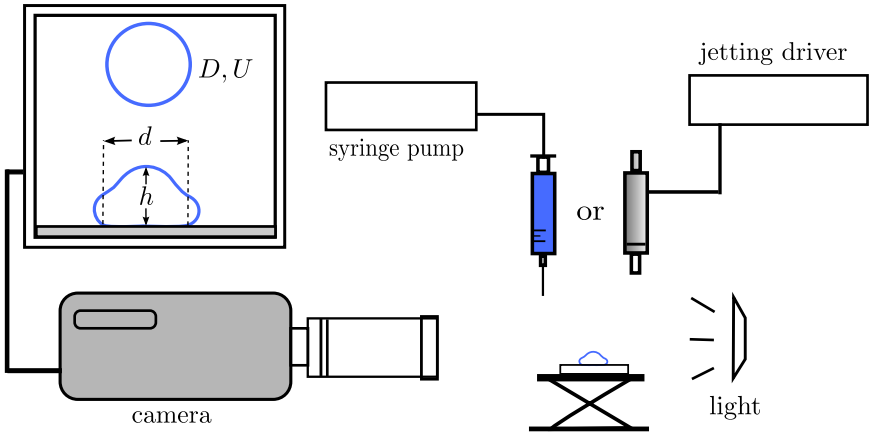

Figure 4.2: Schematic of experimental apparatus.

4.3 Experimental Methods

The drop generation device is mounted on a vertical traverse and the impact surface is placed on a vertical stage. The camera is positioned to view the piezoelectric drop generator nozzle and impact surface in the same field of view with backlighting provided by an Edmunds optical light source. The high speed camera and voltage source for the piezoelectric drop generator are controlled through independent proprietary software. The images are processed using Spotlight, an image analysis software created by NASA, Klimek and Wright [91]. The entire experimental apparatus consists of a high speed camera viewing a drop falling from a profile perspective, Figure 4.2.

The sequences of drop generation, flight, and impact on solid surfaces are visualized through a Phantom V12.1 High Speed Camera. For millimeter size drop impacts we film at 7600 fps. For micron size drop impacts we film at rates of 63063 fps. Hence, for drops that are $\geq$ 100 μm we are able to capture the late inertial and capillarity driven spreading dynamics. The millimeter size drops are imaged with a 180-mm Macro Tamron Lens with a spatial resolution of 17 μm/pixel. A long distance microscope from Infinity, Inc. that provides a spatial resolution of 1.45 μm/pixel is used to resolve the spreading of micron-sized droplets.

The colloidal dispersions are prepared by slowly pouring colloidal particles into a beaker of water that has already formed a vortex from a magnetic stirrer. Care is taken to introduce the powder slowly into the water to avoid excess aggregation and ensure uniform mixing. Once the powder is completely poured into water, the beaker is sealed and the dispersion is mixed for up to 4 hours to ensure uniformity before experimentation. The colloidal particles are composed of varying proportions of Hydroxypropylmethycellulose (HPMC)/Lactose/TiO2/Triacetin/Polyethylene glycol(PEG)/Polyvinyl alcohol(PVA)/Talc. The colloidal particles are obtained from Colorcon, Inc., and are identified by the brand name Opadry. The particle sizes vary for each Opadry formulation but can range from 1-500 μm from tests conduced at Pfizer with a Malvern Mastersizer 2000 laser diffraction measurement. However, a representative particle size is $\mathcal{O}(1\mu m)$. Furthermore the particles are completely wetted by the dispersion medium, in our case, water. An Anton Paar Rheometer with a double gap configuration is used to measure shear viscosity μ. The viscosities over a range of shear rates from 0.001 to 1000 s^{-1} show only a slightly shear thinning behavior, Figure 4.3. Even for impact speeds $U \approx 0.1$ m/s and drop sizes $D \approx 100$ μm, estimated shear rates are $\gg \mathcal{O}(10^3)s^{-1}$. Therefore, the viscosity at 1000 s^{-1} is used as first order estimate in representing dimensionless groups (e.g., Re). Any non-Newtonian effects in the later slower stages of spreading is a case not studied herein. Mica surfaces are used to provide a smooth partially wettable substrate ($\theta \leq 20°$). The mica sheets are cleaved to create fresh surfaces for each experiment. These surfaces provide partial wetting liquid/solid pairs for all liquids studied herein, see Table 4.1.

Drops are produced by a piezodriven capillary tube methodology that can eject monodisperse drops on demand of sizes $D \sim \mathcal{O}(10 - 100\mu m)$. A capillary tube is surrounded by a piezoelectric sleeve. A voltage source is used to send an electric signal to the piezoelectric sleeve. The sleeve expands and squeezes with each pulse which in turn induces a volume change inside the capillary tube, Dijksman [8]. The

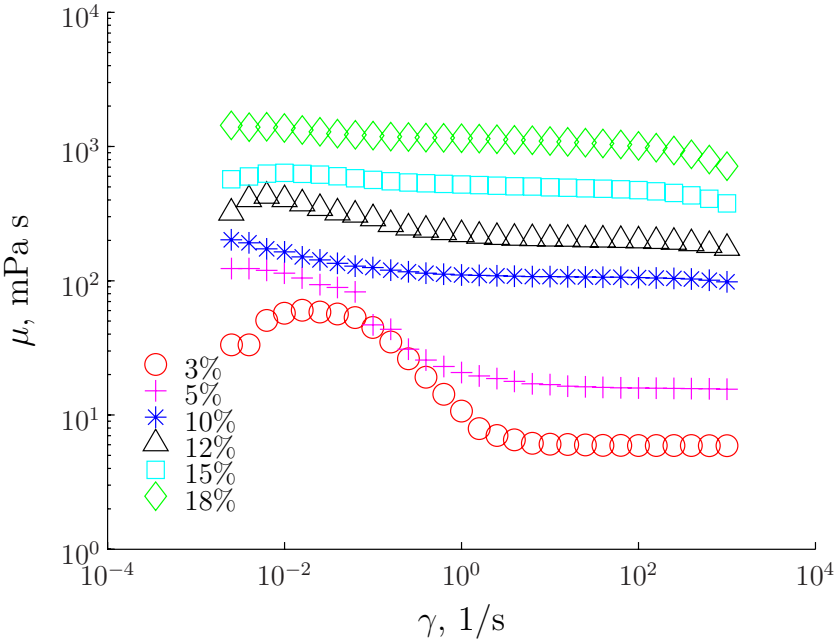

Figure 4.3: Shear viscosity of Opadry suspension #5.

Table 4.1: Summary of fluid properties and wettability.

Fluid	μ, mPa·s @1000 s^{-1}	ρ, kg/m^3	σ, N/m	T, °C	θ on mica
4, 15%, Opadry^{TM}II White, HPMC/PEG	73.6	1040	0.04707	25.4	15
5, 10%, Opadry^{TM}II White, HPMC	98	1020	0.04822	25.4	13
75% Glycerol/H_2O	35.5	1195	0.063[a]	25.4	13
85% Glycerol/H_2O	109	1220	0.062	25.4	16

[a]Interpolated value

drop generator and voltage source used here are from Microfab, Inc., in Plano, TX.

The procedure and mechanism of droplet ejection is as follows. Liquid is pumped into the capillary tube until the meniscus of the liquid is level with the tube outlet, then a waveform is sent to the piezo device which induces a pressure pulse inside the liquid thread. Once the kinetic energy of the liquid tongue ejected out of the tube is sufficient, capillarity will break the thread into one or a series of drops on the order of

the nozzle diameter at speeds of 0.2-1 m/s. The generation of drops by this method is commonly referred to as Drop-on-Demand technology, Chen and Basaran [9]. We use a slightly modified square waveform that follows the shape shown in Figure 4.4, Son and Kim [10].

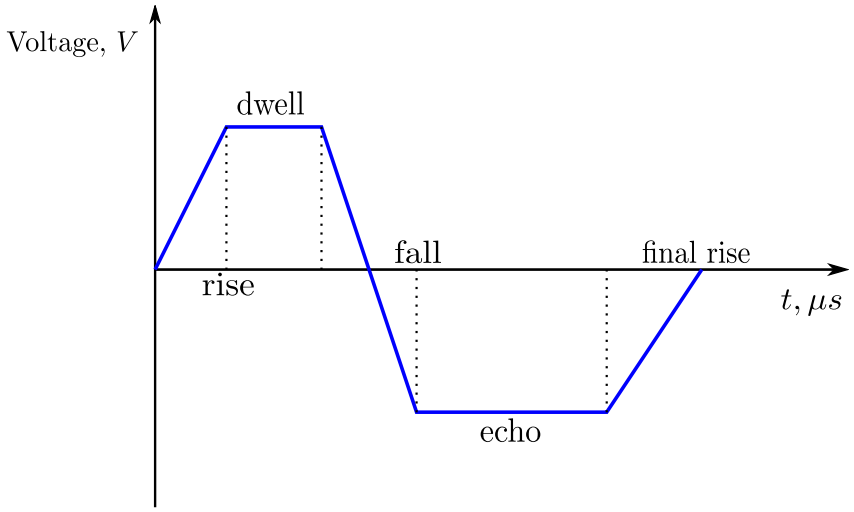

Figure 4.4: Typical waveform used to generated $\mathcal{O}(\mu m)$ sized drops. Typical times are rise = 2, dwell = 15, fall = 4, echo = 45, and final rise = 2 all in μs. Voltages and frequencies range from 20-50 V and 100-1000 Hz.

For higher impact speeds the colloidal dispersions are pumped at (1.12 ml/s) through the piezodriven capillary tube and eject as a liquid jet. A special waveform is used to excite the nozzle and break up the liquid jet into monodisperse drops. The method allows for higher impact speeds unachievable with drop-on-demand methodology.

4.4 Results

Over a range of $We \sim$ 1-10 and $Oh \sim$ 0.1-1, we provide measurements of the spreading diameter $d(t)$ and centerline height $h(t)$ scaled by the initial drop diameter D. For $We \sim 1$ impacts, the spreading regime is dominated by capillarity and resisted by viscosity for times $t > D/U$. In this regime viscous and capillary forces play dominant roles in the spreading dynamics, Figure 4.1. In other words, the drop spreads outwards due to the imbalance at the contact line and is inhibited by the liquid viscosity.

For $We \gg 1$ and $Oh \ll 1$, the spreading is driven by the impact pressure (ρU^2) and has a time scale set by D/U under the effect of inertia. However, for more wettable substrates, $\theta \longrightarrow 0$, a drop will continue to spread for times past D/U. As t reaches D/U, the spreading rate slows down and capillarity takes over inertia to continue driving spreading until it reaches equilibrium, Figure 4.5. For $Oh = 0.2$ and 1.2 (solution 4, 15%) at $We \approx 5$ we observe the continued spreading of a millimeter and micron sized drop, respectively, after time scale D/U has been reached and surpassed, Figure 4.6. The diameter continues to spread until $Ut/D \sim \mathcal{O}(10^2)$ suggesting the influence of a new time scale. In this regime, the spreading is driven by capillarity and resisted by viscosity which points toward the viscous time scale $\mu D/\sigma$. The spreading dynamics at increased We indicate a larger spread from the initial inertia-dominated stage, but, during the viscous stage the spreading diameter $\beta(t) = d(t)/D$, maintains a power law that varies between $(t/\tau)^{1/5} - (t/\tau)^{1/7}$ where $\tau = \mu D/\sigma$, Figure 4.7. This dependence is much faster than Tanner's law $R \sim t^{1/10}$ since we are in an earlier transient regime. The speed of the spreading is captured in the short times following D/U in a span of $16{\times}10^{-2}$ s, unlike most experimental studies which confirm Tanner's law over spreading times of $\mathcal{O}$(s), Rafaï et al. [28], Chen [27].

We observe similar spreading dynamics for a different colloidal dispersion with an $Oh \approx 1.3$ (solution 5, 10%). For increasing We we find spreading rates between $t^{1/7}$-$t^{1/6}$, Figure 4.8. Again we see that the initial area covered by the drop is larger for

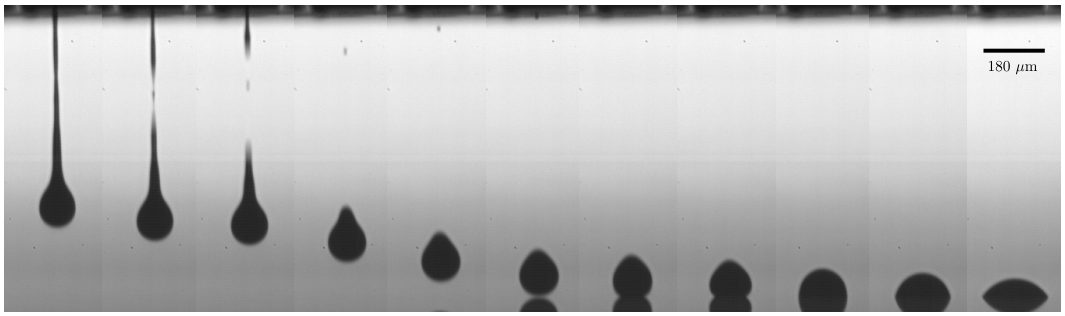

Figure 4.5: #5, 10% on mica spontaneous spreading. The drop size is 115 μm and the total time shown 3 ms.

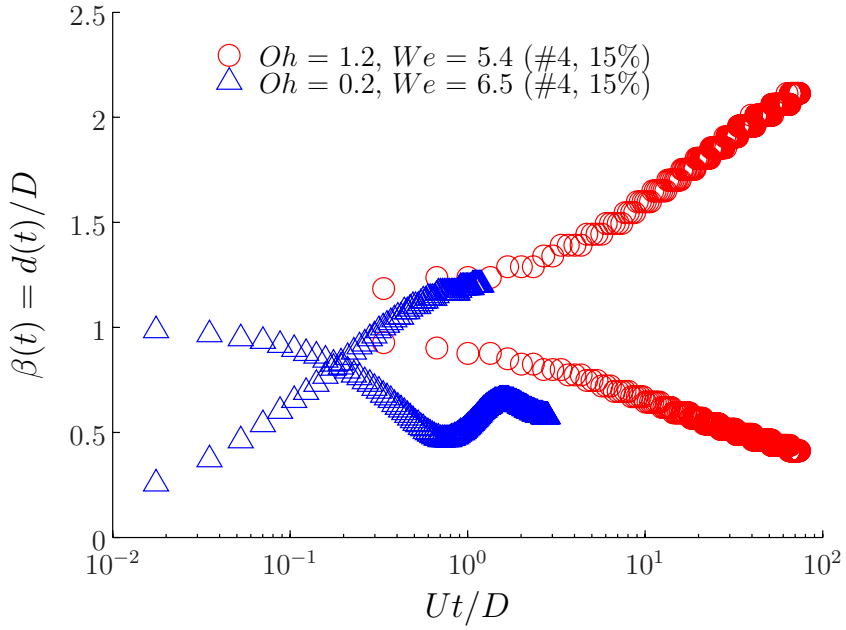

Figure 4.6: Continuation of spreading from mm to μm drop impacts of colloidal dispersion #4, 15%. ◯ are from micron drop impacts and △ are from mm drop spreading.

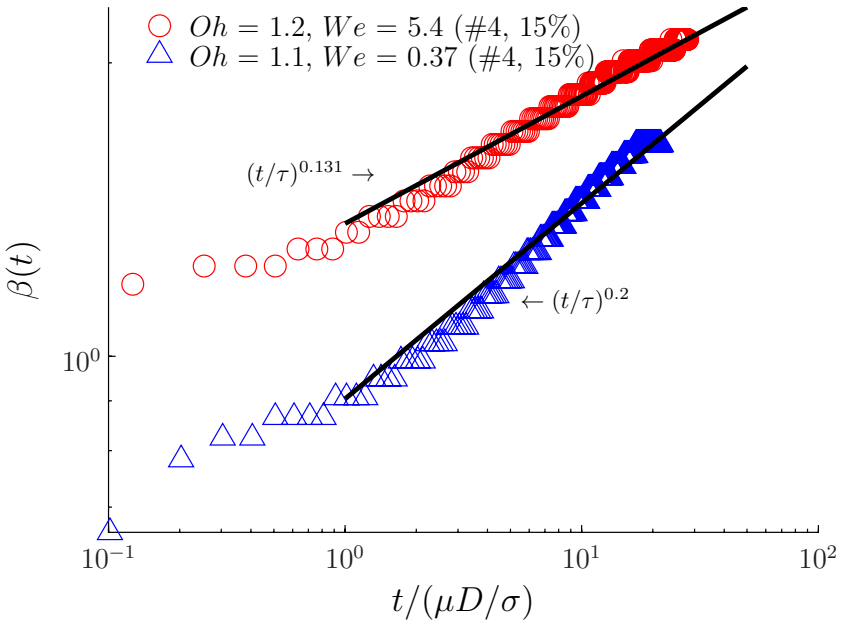

Figure 4.7: Transient spreading dynamics immediately following inertial driven phase D/U. The first four data points correspond to maximum spreading diameter due to inertia then transitions to capillary/viscous time scale $\tau = \mu D/\sigma$. Spreading continues until equilibrium ($\theta = 15°$) is reached. For $We = 5.4$ the initial area covered before spontaneous spreading ensures is larger but resulting dynamics follow a strong power law, $d(t)/D \sim (t/\tau)^n$. For $We = 5.4$ and 0.37, $n = 0.13$ and 0.20, respectively.

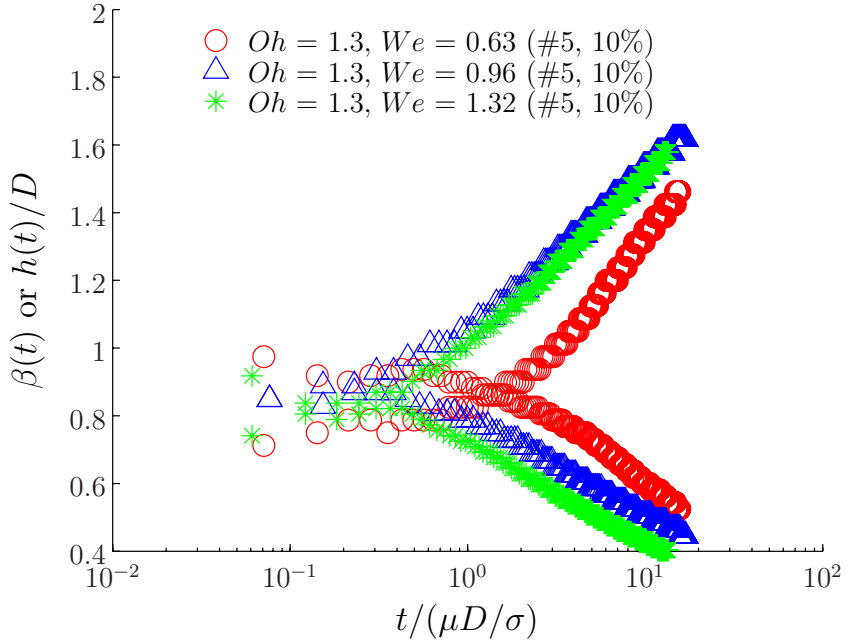

Figure 4.8: Capillary driven spreading on mica for 5, 10% with $\theta = 13°$.

increasing We as we should expect. However, the capillary driven spreading proceeds to follow a narrow band on n, $d \sim t^n$. For our viscous Newtonian 75% glycerol/water solutions the stage of spreading extends over a longer time span $t \approx 2\mu D/\sigma$ compared to $\mu D/\sigma$ for lower We, Figure 4.9. But for higher $Oh = 1.1$ glycerol/water solutions seen in Figure 4.10, the spreading at the end of the initial inertia dominated stage is larger as the We goes up. For the viscous stage, the exponent of the spreading rate is smaller for the larger initial spreading, so that all three experiments potentially reach a common final spreading diameter at late times. It is still unclear if the colloidal dispersions behave quantitatively different than Newtonian solutions at the same Oh number. The exponent in the power law may reveal a distinction.

For $We \approx 1.5$ and $Oh \approx 1.2$ in Figure 4.11 we observe the spreading rates fall under $t^{1/10}$. Similarly, for a colloidal drop impacting at $We \approx 0.4$ and $Oh \approx 1.2$ (solution 4, 15% and 85% glycerol/water) shown in Figure 4.12 , the spreading diameter $\beta \sim t^{1/5}$

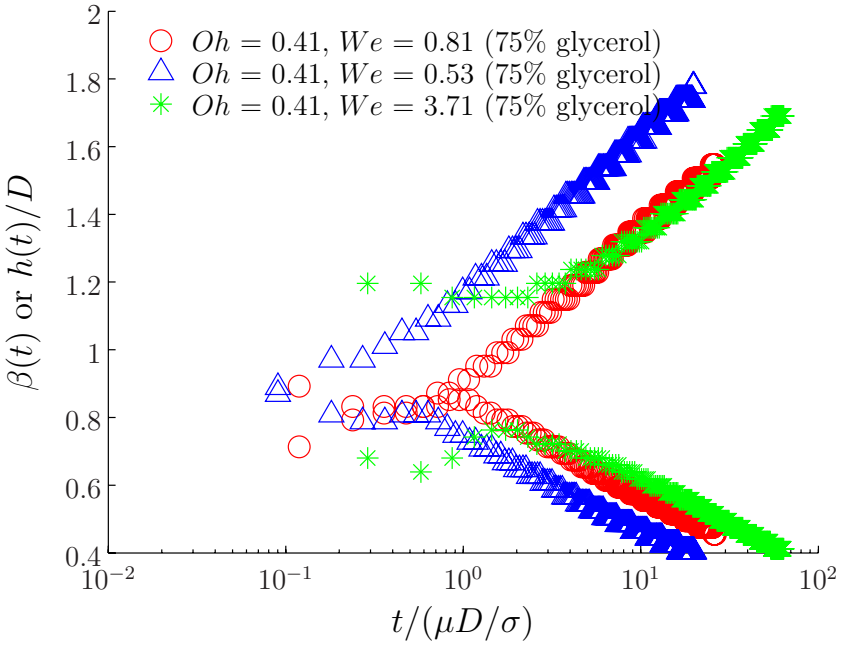

Figure 4.9: Spreading on mica with $\theta = 13°$. For $We = 3.71$ the contact line pins then continues to spread and follow lower We path.

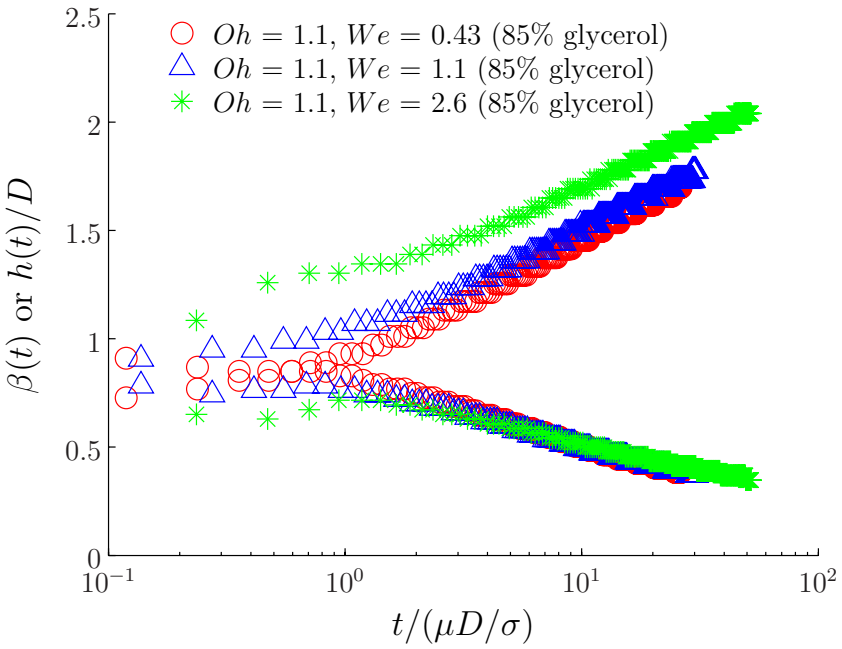

Figure 4.10: 85% glycerol/water on mica with $\theta = 16°$.

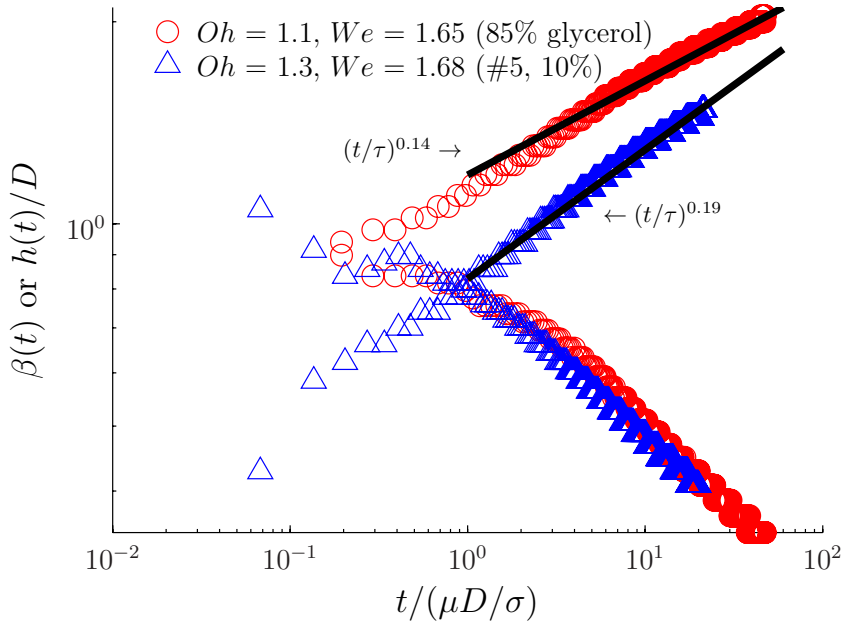

Figure 4.11: Effect of colloidal particles for colloidal dispersion #5, 10% and 85% glycerol/water with contact angles of θ of 13° and 16°, respectively.

accurate to within 12%. A summary of all the coefficients found from fitting the spreading diameter reveals that, with increasing We, the value of the constant C increases and the exponent n decreases, Figure 4.13. The coefficient C is $\mathcal{O}(1)$ which suggests that the viscous time scale τ is appropriate to describe these early times. The exponent n reaches a maximum of 1/5 for very low We and then approaches 1/7 for increasing We. However, only the viscous glycerol/water solutions approach 0.1 while the colloidal dispersions consistently stay in the range $1/7 \leq n \leq 1/5$, (see Table 4.2).

Admittedly, comparing the spreading diameters of the colloidal dispersions and glycerol solutions remains a challenge. We expect the volume fraction of the colloidal dispersions to be reduced for an ejected micron size drop compared to a millimeter size drop ejected from a syringe. However, the power law exponent n is consistently higher, approaching $n = 1/5$ for $We \longrightarrow 0$ which suggests a depletion of particles

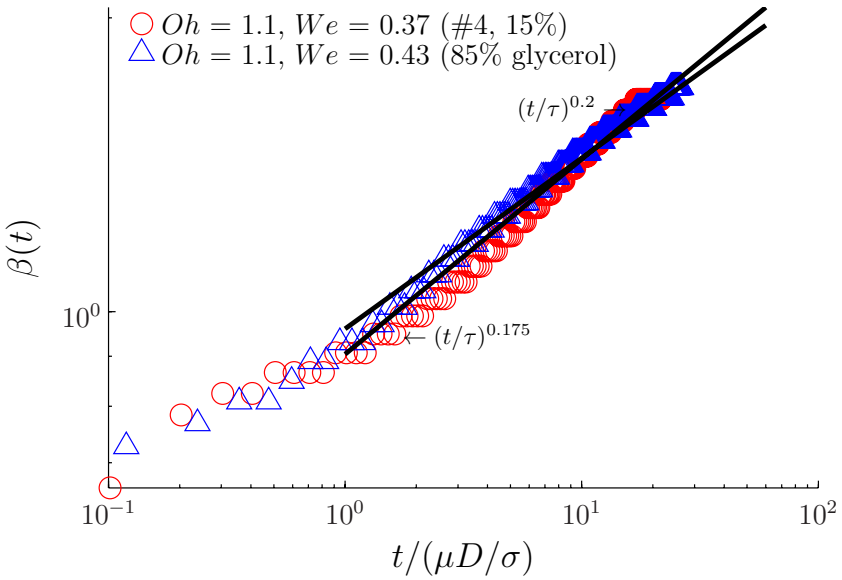

Figure 4.12: Effect of colloidal particles for colloidal dispersion #4, 15% and 85% glycerol/water with contact angles of θ of 15° and 16°, respectively. The spreading exponent n is 0.20 and 0.17 for dispersion and glycerol solutions, respectively.

Table 4.2: Average values of n and C for $We < 1$ and $We > 1$ for $0.4 \leq Oh \leq 1.4$.

	C	C	n	n
	$We < 1$	$We > 1$	$We < 1$	$We > 1$
Colloidal Dispersions	0.945 ± 0.149	1.05 ± 0.174	0.193 ± 0.023	0.157 ± 0.025
Glycerol Solutions	0.991 ± 0.117	1.14 ± 0.146	0.158 ± 0.013	0.128 ± 0.014

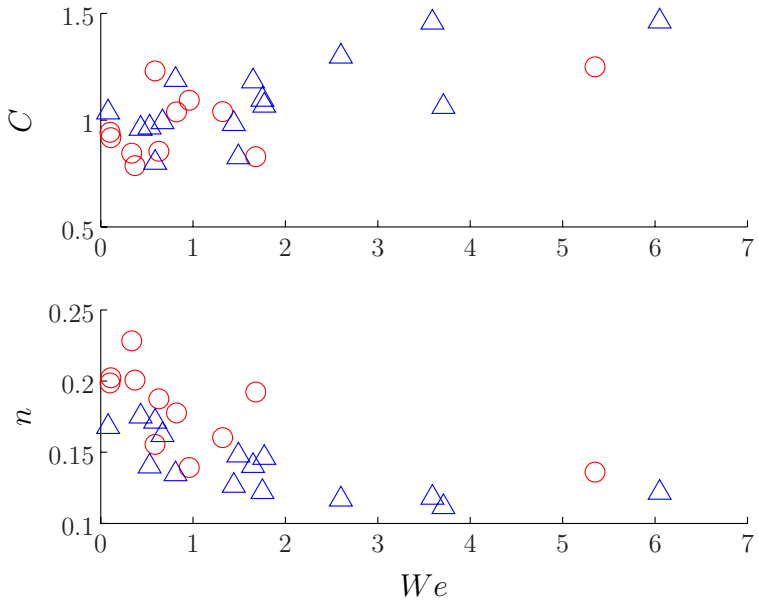

Figure 4.13: The spreading dynamics is fit to a power law $d(t)/D = C(t/(\mu D/\sigma)^n$. Fit values of C and n versus We for all viscous solutions. The red (◯) identify the colloidal dispersions and the blue (△) are the glycerol/water solutions. For $We < 1$ the colloids have $n = .193 \pm .023$ and $C = 1.05 \pm .174$ and for glycerol solutions $n = .158 \pm .013$ and $C = .991 \pm .117$. See Table 4.2 for complete statistics.

near the contact line. It could also be explained by the nature of incomplete partial wettability in which Tanner's law is restricted to fully wetting systems. Higher spatial resolution near the contact line would help clarify the mechanism responsible for this counter-intuitive phenomenon.

4.5 Conclusion

We studied micron-size droplets deposited on nearly fully wettable substrates in a parameter domain $0.1 < We < 10$ and $0.1 < Oh < 1$. We find that capillary spreading of micron-sized drops evolves according to a power law $d(t)/D = C(t/\tau)^n$, where $\tau = \mu D/\sigma$ and C and n are constants. This power law result is robust over the range of We studied: the coefficients C and n are $\mathcal{O}(1)$ constants. For colloidal dispersions with high Oh the exponent $n \rightarrow 1/5$ which has not been reported in early studies due to limited temporal resolution. For increasing We, the exponent n decreases. This result demonstrates the effect of residual inertia influencing the transient spreading dynamics immediately following inertial driven spreading. For Newtonian solutions at approximately equivalent Ohnesorge numbers the colloidal dispersions evolve with a lower time exponent n (slower spreading history). Moreover, we show how the early behavior of the spreading diameter evolves towards Tanner's law, $D \sim t^{1/10}$ for Newtonian solutions, as $We \longrightarrow 0$, yet this trend needs to be investigated systematically.

Chapter 5

OSCILLATORY AND SPREADING BEHAVIOR OF VISCOUS ACETONE-BASED SOLUTIONS

Droplet impact and spreading of acetone-based solutions relevant to pharmaceutical coating processes are investigated experimentally. We find that over a wide range of $We \sim$ 10-300 and $Oh \sim$ 0.01-1, the spreading dynamics and the maximum area is consistent with two energy balance based models. We also identify a narrow range of conditions $We \sim$ 30-50, where the centerline height sinks below a developing thick rim. The rim dynamics proceed to rise linearly while the contact line remains pinned in a process found consistent for both millimeter and micron-size drop impacts. The mechanism for this phenomenon is explained in terms of capillary wave propagation. This regime was also found in our earlier investigation discussed in Chapter 3 for colloidal dispersions and Glycerol/water solutions and is associated with the spread of high viscosity fluids (high Ohnesorge number) on a partially wettable surface ($0° < \theta < 90°$) at intermediate Weber numbers.

5.1 Introduction

In the pharmaceutical industry, spray coating processes require three processes to work in tandem to provide an ideal tablet finish. First, the coating liquids need to be disintegrated into drops that are $\mathcal{O}(10 - 100)\mu$m size range. The disintegration process is accomplished through a coaxial atomizer which injects a low speed liquid jet together with an annular high speed gas jet. The gas jet provides the high momentum source which induces a cascade of hydrodynamic instabilities, namely Kelvin-Helmholtz and Rayleigh-Taylor, that create a distribution of droplets of suf-

ficient size and speed, Figure 5.1. Such instabilities have led to an analytical model that is in good agreement with experiments, Aliseda et al. [4]. On their flight to the tablets, the newly created drops undergo evaporation of the solvent, a process that requires precise control to prevent unnecessary phase changes before the drops impact and spread on the tablets. Sartori [5] characterized the transport and drying of colloidal dispersion and acetone-based solutions and determined that the diameter of the drop shrinks according to the d-squared law, Law [98]. Finally, the last process is the droplet impact and spread on the tablets. The impact, spreading, coalescence, coverage, and drying of the liquid droplets all contribute to the final uniformity and finish of the tablet coating. Fundamentally, the impact and spreading of liquid droplets on solid surfaces play a significant role in these tablet spray coating operations. The rheology of these types of coating fluids presents a gap in drop impact studies despite its industrial relevance. Our studies in this range of parameters has elucidated a viscous dominated resonant regime previously unreported because in these flow scenarios, the effect of viscosity is one or two orders of magnitude larger than most previous studies, Yarin [15]. In our recent experiments, we observed that the impact and spreading of highly viscous colloidal dispersions provide reasonable agreement (within 10%) of the maximum spreading diameter with three well established models, Bolleddula et al. [99]. Furthermore, for moderate impact speeds we observed the rim height to increase linearly with times bounded around the time to reach the maximum spreading diameter. We also observe this behavior in the current study and propose a mechanism to explain this phenomena. The majority of studies that investigate droplet impact phenomena use fluids with simple rheology, namely Newtonian shear viscosities and constant surface tension. However, most industrial applications require coating liquids with highly complex rheology. The coating liquids used in the pharmaceutical industry can be classified into two broad categories: colloidal dispersions and acetone-based solutions. The various compositions of these constituents sets the final finish of the coat on the tablets. These coatings serve multiple purposes, some as simple

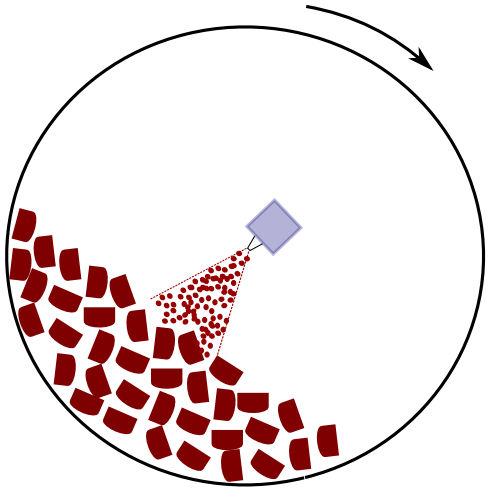

Figure 5.1: Simple schematic of spray coating operation. Atomizer at the center sprays tablets as they are turned. Drying air (not shown) subsequently cures coating.

as brand recognition, and masking unpleasant taste, and some more sophisticated such as controlled-release porous coatings that slow down tablet dissolution for as long as 8 hours. Recently, acetone-based solutions have been formulated to improve the accurate dosage of active ingredients. Because of the high volatility of acetone at room temperature (20°C) and pressure, these solutions require containment prior to experimentation to avoid evaporation of the acetone out of solution. However, when the coating solution impacts and spreads, the residence time is orders of magnitude shorter than the characteristic time of evaporation, thus preventing the coating from undergoing segregation of the phases.

When these solutions are exposed to the environment they undergo rapid evaporation of the solvent, phase change, and membrane formation on the free surface. Hence, the challenge with working with such fluids is controlling the characteristic time of transport to the characteristic time os phase change. If proper control is achieved, then the drops will impact and spread and then subsequently proceed to evaporate and leave a porous coat that serves as the barrier and means of providing controlled release of active ingredients. Similar types of these solutions have been

investigated in a series of works by Altinkaya [6, 100, 101] with experiments on the phase change with similar constituents as used in the pharmaceutical industry. Altinkaya [6] showed the network of polymeric structures formed after drying through SEM images. These structures maintain their structural integrity in the stomach to provide a porous barrier for the drug to penetrate into the patients' system at a constant, repeatable rate. Furthermore, Altinkaya [6] showed the locations of spinodal and binodal decomposition on ternary phase diagrams of CA, Acetone, and Water. Through a dip coating process, Altinkaya [6] created a film that is several orders of magnitude larger than the drops created in spray coating operations. The film formation requires orders of magnitude longer than the time scale of drop impact. The formation of membrane like structures is a particularly important topic as a means of assessing final coat finish.

Because of the relatively unstable nature of these solutions, the time and uniformity of tablet coating finish must be quantified and scaled accurately. In particular, the drop size and homogeneity play a key role in spreading of droplets on solid surfaces. One key parameter in drop impact studies is the maximum spreading diameter, which is a quantity used to estimate the area covered by a droplet during the first moments of contact.

Most approaches are based on the energy balance of a drop before and after impact with the underlying assumption that the kinetic energy of the drop is negligible after deposition. This assumption may not be consistent with observations of drops which impact, spread, and recede, Roisman et al. [38]. On surfaces which exhibit limited attractive forces, i.e. water on teflon, a drop will impact spread and recede and settle to equilibrium. Since the liquid is only partially attracted to the solid, the liquid dissipates a smaller fraction of energy at the contact line. While a portion of the energy is dissipated within the drop, a sufficient amount may remain as surface energy to drive retraction. However, experimental verification beyond visual observations has not been attempted to date. The forces which accompany spreading and recession

can be compared through dimensional analysis.

For a liquid drop of diameter D falling at a speed U with density ρ, surface tension σ, and viscosity μ, we obtain

$$We = \frac{\rho D U^2}{\sigma}, Re = \frac{\rho D U}{\mu}, Oh = \frac{\mu}{(\rho \sigma D)^{1/2}} = \frac{We^{1/2}}{Re}. \tag{5.1}$$

The effect of inertia is seen through the Weber and Reynolds numbers while the Ohnesorge number is purely a function of the liquid properties and a characteristic length scale, in this case the size of the drop D. However, the drop size D plays a key role in enhancing the effect of viscosity since $Oh \sim 1/D$. Moreover, the drop size regulates the effect of gravity which is often neglected in the majority of drop size studies, noting that $Fr = U^2/(Dg) \ll 1$, Rioboo and Tropea [13]. The Bond number ($Bo = \rho g D^2/\sigma$) is however, a more accurate indication of the effect of gravity on drop spreading. Dong et al. [92] conducted experiments with micron-sized droplets, $Bo \ll 1$, and found no discernible effect of gravity on droplet spreading for $Oh \sim 0.001$ drops of Newtonian liquids.

The maximum spreading diameter is obtained during the inertial or kinematic phase of drop impact, with a characteristic time scale of Ut/D, where U and D are the impact velocity and initial drop diameter, respectively. In this regime, the drop spreads solely due to the inertia of the drop and doesn't have time to reach an equilibrium with the presence of intermolecular forces between the liquid and the solid. These intermolecular forces are well described by Young's equation, which describes the minimal shape of a drop on a solid surface according to the interactions between the solid/liquid/gas interfacial tensions as $\sigma \cos\theta = \sigma_{sg} - \sigma_{ls}$, where s, l, and g represent the solid, liquid, and gas surfaces. These forces only play a role for $t \gg D/U$ and mostly on fully wettable surfaces ($\theta < 10°$). Thus the impact dynamics and spreading are reasonably described by either an energy balance before and after impact or, more recently, by applying conservation of mass and momentum on a drop spreading, Roisman et al. [38]. For highly viscous colloidal dispersions studied, we

found that a simple energy balance approach developed by Mao et al. [2] and Asai et al. [1] provides good agreement between predicted and experimental maximum spreading diameters to within 10%. It is unclear how robust these models developed for Newtonian liquids will stand up to the highly viscous and complex rheology liquids studied herein. Also, we will investigate how the effect of viscosity is enhanced with drop sizes that decrease by orders of magnitude. Associated with the dynamics of the spreading diameter is the film thickness, and in particular the dynamics of the spreading rim.

The dynamics of rim and film thickness of the drop have recently attracted attention in the literature. The thickness of the rim of the thin lamella near the splash threshold was measured at times shorter than D/U and found an unusual plateau behavior at high impact speeds, de Ruiter et al. [102]. However the liquids studied were low viscosity alcohols. Furthermore, Roisman et al. [103] extracted rim data for similarly low Oh number cases. In such cases, a less viscous regime for high impact speeds was investigated near or during splashing events. Herein, we observe that for liquids with viscosities within 10-100 cP at $We \sim 30$, a thick rim develops as the centerline height of the drop sinks below. During this phase, the rim height grows linearly with time until the centerline height of the drop recovers above the rim. The centerline height of the drop then proceeds through one or two periods of oscillation and then damps to equilibrium. This regime is analogous to the stair-cased shapes observed for drops impacting superhydrophobic surfaces with the exceptions of the capillary waves visually imperceptible and the absence of a contact line, Renardy et al. [52]. This behavior has not been observed to our knowledge. This is reasonable since we are studying realistic rheology coating liquids under a wide range of operating conditions. In the following sections, we will describe our experimental methods and uncover the spreading dynamics of highly volatile acetone-based solutions over a range of dimensionless groups indicative of actual spray coating conditions.

5.2 Experimental Methods

The coating liquids used in this study are derived from formulations created by our collaborators at Pfizer to provide controlled-release functionality for gastroenteric drug delivery. These solutions are acetone-based and hence must be prepared and used immediately to avoid rapid evaporation. The acetone-based solutions are prepared by mixing the different solvents and stirring until a central vortex forms in the beaker. Water soluble components are added first and then, the Cellulose Acetate(CA), which makes up the large majority of the solid content in the solution, is slowly poured to facilitate dissolution of Cellulose Acetate in acetone. Once the CA is completely added to the mixture, the beaker is covered and allowed to mix for up to 4 hours to ensure the CA is completely dissolved. Glycerol/water solutions are prepared in a similar manner with the exception of the water being poured into the glycerol and are utilized as Newtonian fluids for comparison with the acetone-based solutions.

An Anton Paar Rheometer with a double gap configuration is used to measure shear viscosity μ. The viscosity values over a range of shear rates from 0.001-1000 s^{-1} show only a slightly shear thinning behavior, Figure 5.2. For impact speeds $U \sim \mathcal{O}(10^{-1}\text{m/s})$ and drop sizes $D \sim \mathcal{O}(10^{-4}\text{m})$, estimated shear rates are $\gtrsim \mathcal{O}(10^{3}\text{s})$. Possible non-Newtonian behavior at very low shear rates would present itself in millimeter-size drops gently placed on a substrate, a problem not studied herein. Therefore, the viscosity at 1000 s^{-1} is used as a first order estimate in representing dimensionless groups (i.e. Re, Oh).

The impact surfaces are actual tablet cores which vary in composition, hardness, and surface treatments. The tablet cores are made with either Microcrystalline cellulose (MCC) or Magnesium Stearate. The main variable in this study is the amount of hydrophobic lubricant precoated on the tablet which varies from 0 to 4%. The surface energetics are obtained from sessile drop measurements on the different liquid/surface combinations and show partial wetting characteristics for the acetone-based solutions,

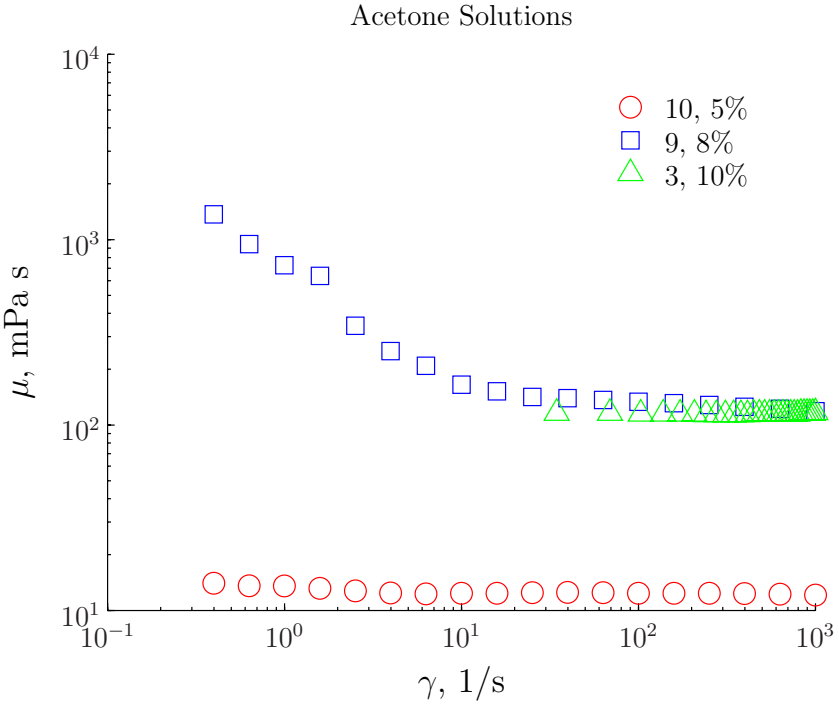

Figure 5.2: Shear viscosities over range of shear rates displaying slightly shear thinning behavior.

Table 5.1. Mica surfaces are used as a control in validating impact results at identical We. Mica surfaces are cleaved to provide a fresh, clean, and smooth surface.

Single drops are ejected by one of two methods. 1) A drop of liquid is forced through a blunt needle via a syringe pump and allowed to drop under its own weight. The drop sizes are approximately 2.6 mm in diameter and are calculated from the images of each individual experiment. The impact speeds vary from 0.3-2.5 m/s with corresponding release heights of 4-300 mm, respectively. 2) Drops of size $D < 1$ mm are generated via piezoelectric driven nozzle. In our setup, a capillary tube is surrounded by a piezoelectric sleeve from Microfab Inc., Plano, TX. A jet of liquid is forced through the nozzle and breaks into individual droplets due to a the Rayleigh-Plateau, (i.e. the same process observed in a water faucet slightly open). We couple this phenomena with by forcing the piezoelectric nozzle simultaneously and thus achieve

Table 5.1: Summary of equilibrium contact angles from FTÅ200 measurement system.

Fluid	03134	03135	03136
Solution 3, 10%	93	95	88
Solution 9, 8%	79	112	80
Solution 10, 5%	68	67	53

Table 5.2: Waveform parameters, all in μs

rise	dwell	fall	echo	final rise
2	15	4	45	2

droplet breakup earlier in the jet stream. For this process, maintaining a clean nozzle is critical to forcing the liquid jet out of the orifice since precipitous film formation often clogs the nozzle orifice. We have been able to create drops $D \sim \mathcal{O}(10 - 100\mu m)$ that impact at speeds $U \sim 1$ m/s. The waveform used is a slightly modified square wave, similar to that shown in Figure 5.3. The exact parameters are given in Table 5.2, (Son and Kim [10]).

The sequences of drop generation, flight, and impact on solid surfaces are visualized through a Phantom V12.1 High Speed Camera. For millimeter size drop impacts we film at 7600 fps. For micron size drop impacts we film at rates of 30000-60000 fps. Hence, for drops that are $\geq$100 μm, we are able to capture the inertial and capillary driven spreading dynamics. The millimeter size drops are recorded with a 180-mm Macro Tamron Lens with a spatial resolution of 17 μm/pixel. A long distance microscope from Infinity, Inc. provides a spatial resolution of 1.45 μm/pixel, used for the micron sized droplets.

The overall setup up of the experimental apparatus consists of a high speed camera

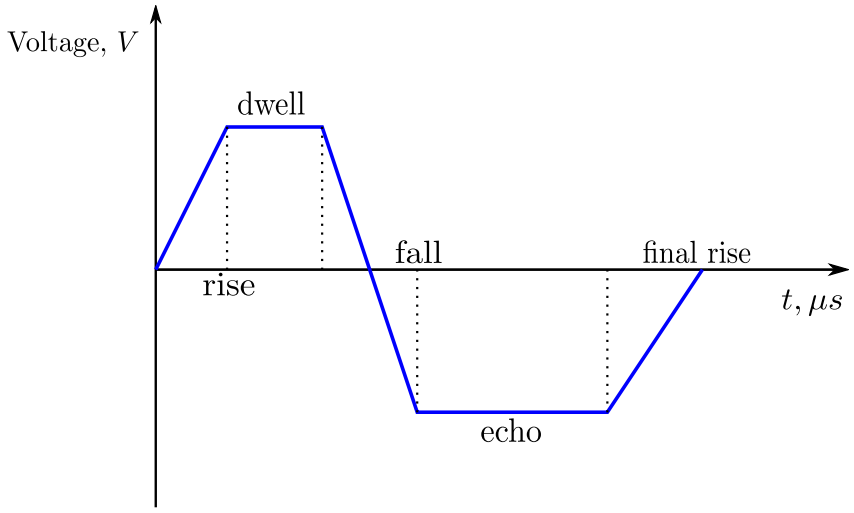

Figure 5.3: Typical waveform used to generated $\mathcal{O}(\mu m)$ sized drops. The specific times are identified in Table 5.2.

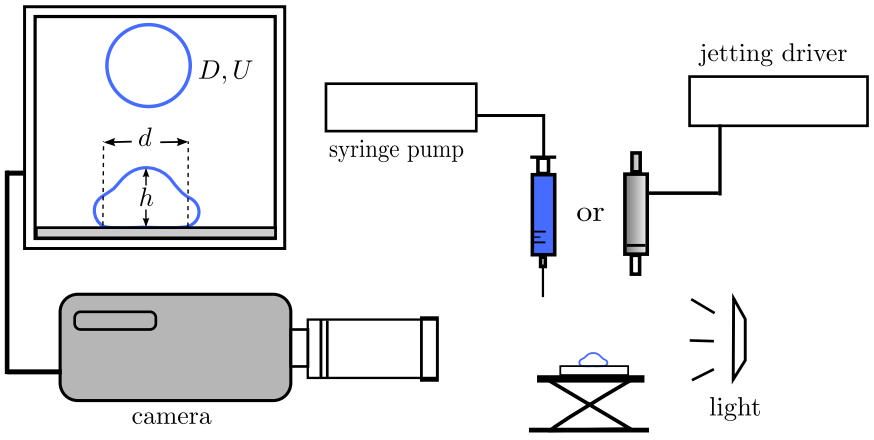

Figure 5.4: Schematic of experimental apparatus.

viewing a drop falling from a side view, as shown in Figure 5.4. The impact surface is placed on a vertical stage. The drop generation devices are mounted on a vertical traverse. The drops are backlit by an Edmunds optical-fiber light source. The high speed camera and voltage source (jetting drive) are controlled by proprietary user software. The images are processes using Spotlight, an image analysis software created by NASA, Klimek and Wright [91]. The maximum spreading diameter from up to 9 repeated tests of a single experiment is used to estimate experimental reproducibility. We find the maximum/minimum standard deviation is $\pm 8.5\%/2.1\pm\%$. The entire drop impact test space is summarized in Table 5.3.

Table 5.3: Summary of calculated dimensionless parameters from experimental set. Each of the acetone-based solutions is identified by (#), (% solids). Impact surfaces are actual tablets identified by 3134, 3135, and 3136 which vary in precoated hydrophobic lubricants.

	#10, 5%			#9, 8%			#3, 10%		
	We	Oh	Re	We	Oh	Re	We	Oh	Re
3134 (2%)	9.3	0.047	65	6.4	0.36	7	9.4	0.47	6.5
	58	0.043	174	28	0.35	15	50	0.46	15.4
	420	0.04	467	383	0.35	56	326	0.47	39
3135 (4%)	6.93	0.047	56	5.7	0.38	6.2	10.2	0.45	7
	50	0.045	157	28	0.36	15	50	0.45	15.6
	399	0.046	438	377	0.36	54	364	0.46	42
3136 (0%)	5.15	0.044	51	0.82	0.36	2.5	12.7	0.46	7.7
	54.8	0.045	163	33	0.38	15.5	53	0.46	16
	423	0.043	469	391	0.35	56	361	0.47	40.6

5.3 Results and Discussion

Over the range of $We \sim$ 1-400, $Re \sim$ 1-400, and $Oh \sim$ 0.01-1 (see Table 5.3), our results for droplet impact with partial wettability ($\theta = 53^\circ - 112^\circ$) are described by inertia dominated spreading, exponential growth in spreading area, and a maximum diameter observed at dimensionless times of $\tau = Ut/d \sim 1 - 4$, as shown in Figures 5.5, 5.6, and 5.7. In this regime, there is a sharp rise in the spreading diameter of the drop $d(t)$ followed by an abrupt arrest of the contact line. The maximum area covered during this inertial dominated regime is referred to as the maximum spreading diameter which can be predicted from an energy balance approach, Asai et al. [1], Mao et al. [2]. Furthermore, the centerline height, $h(t)$, decreases sharply and either asymptotes or abruptly reaches a minimum and starts to increase. In this last case, $h(t)$ proceeds through a short oscillatory period. Finally, the maximum diameter is observed at times characteristic of the end of the inertia-dominated time scale. Despite the fact that the nature of these solutions inherently contain complex phenomena, the spreading history and maximum spreading diameter can be predicted within reasonable agreement. Figures 5.8 and 5.9 shows a comparison of two predictive models for the maximum spreading diameter and both show good agreement with the highest error for $We \sim 300$. This result illustrates the effective choice of viscosity for characterizing experimental results. This agreement also illustrates the characteristic time for this spreading event $Ut/D \sim 1$ is sufficiently faster than the characteristic time for phase change. Furthermore, we find the effect of wettability is negligible in this time scale and only enhances spreading if the solid/liquid has a sufficiently small contact angle ($\theta < 10^\circ$). One key feature not previously studied in drop impact studies is the regime observed in the centerline height after a nondimensional time equal to 1. Under certain conditions characterized by $0.01 \leq Oh \leq 0.1$ and $10 \leq We \leq 50$, the centerline height of the drop seems to increase in a linear fashion then proceed through a one or two periods of damped oscillation, Figures 5.10 and 5.11.

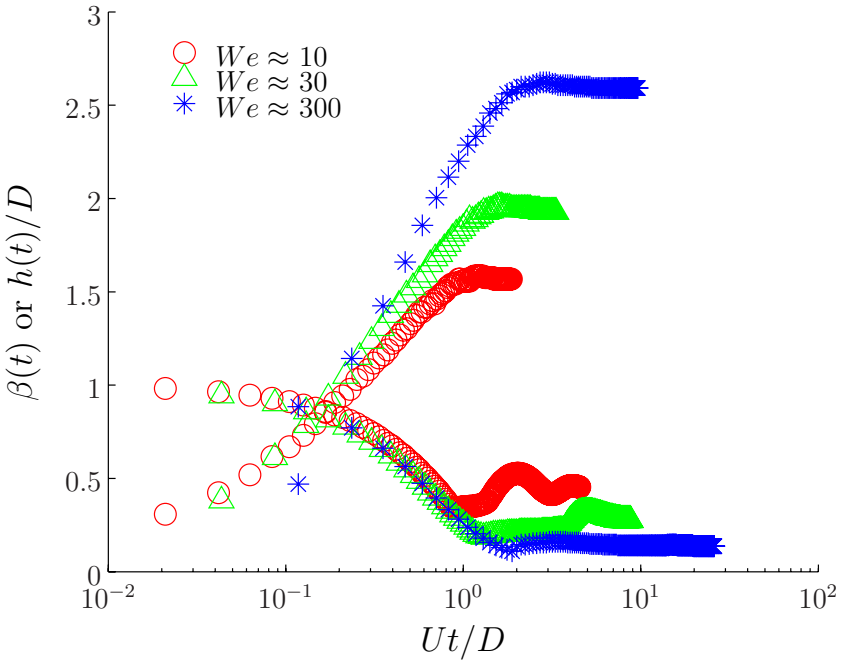

Figure 5.5: Spreading diameter and centerline height for #10, 5%($Oh = 0.047$) tablet 03134.

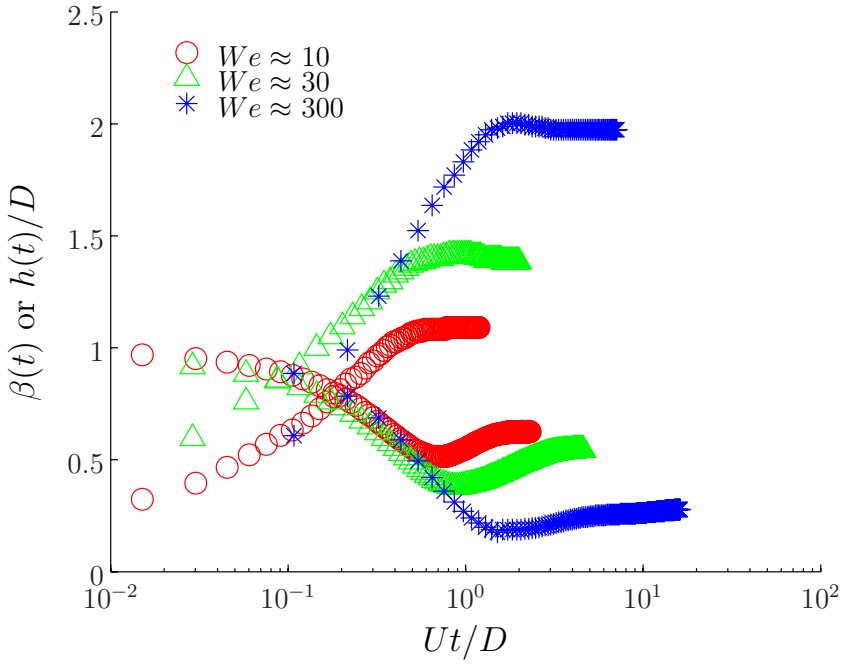

Figure 5.6: Spreading diameter and centerline height for #9, 8%($Oh = 0.36$) tablet 03134.

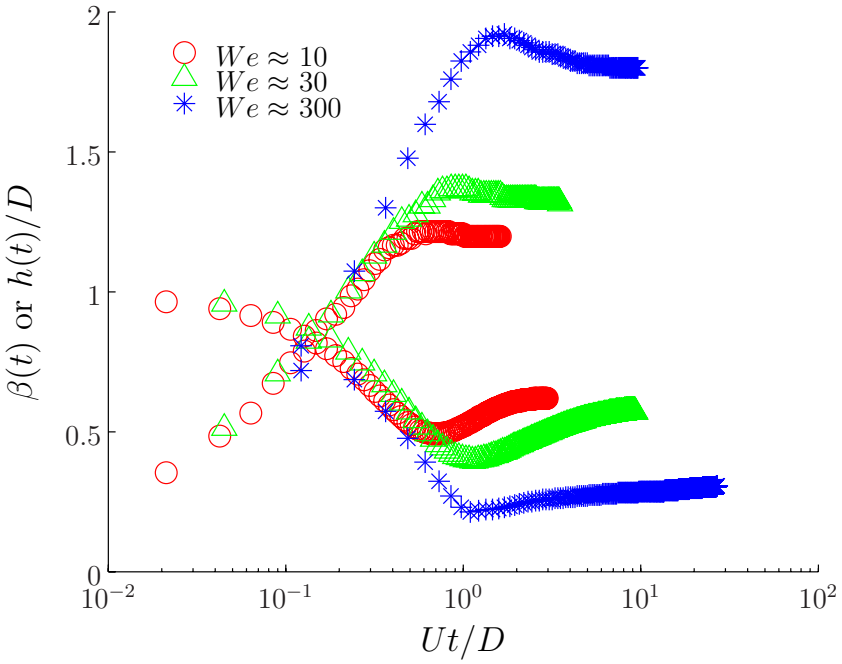

Figure 5.7: Spreading diameter and centerline height for #3, 10%($Oh = 0.46$) tablet 03134.

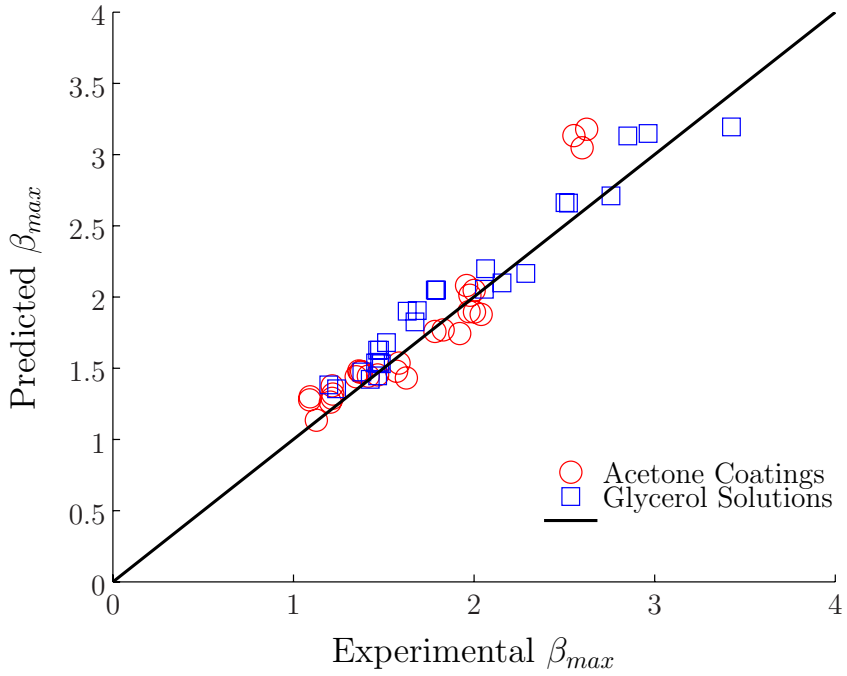

Figure 5.8: Summary of β_{max} diameters for all fluids tested at a time of 1-4 Ut/D versus model of Asai, Eq. 3.15. Red circles indicate acetone solutions and blue squares indicate glycerol/water mixtures.

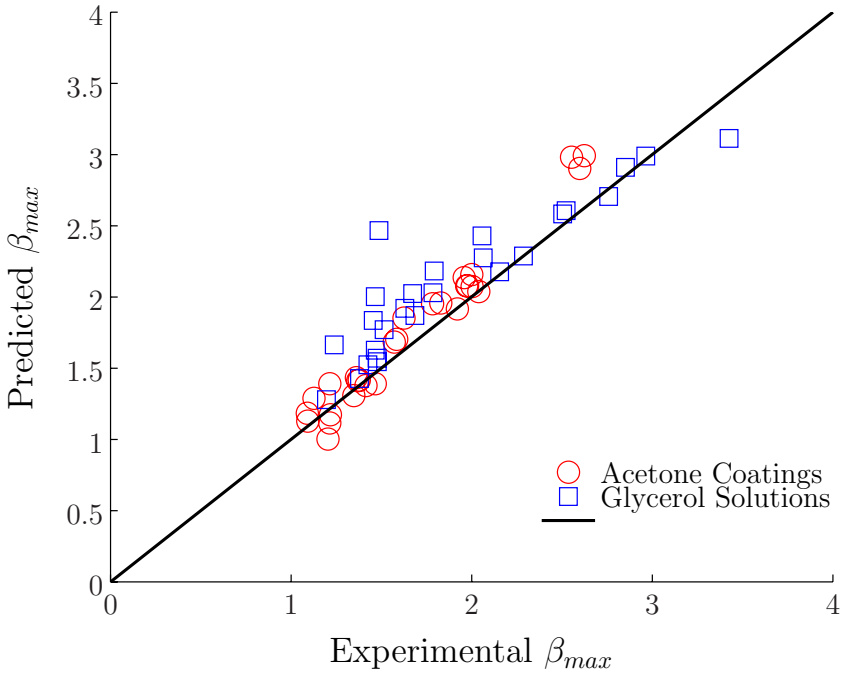

Figure 5.9: Summary of β_{max} diameters at a time of 1-4 Ut/D versus model of Mao, Eq. 3.14. Red circles indicate acetone solutions and blue squares indicate glycerol/water mixtures.

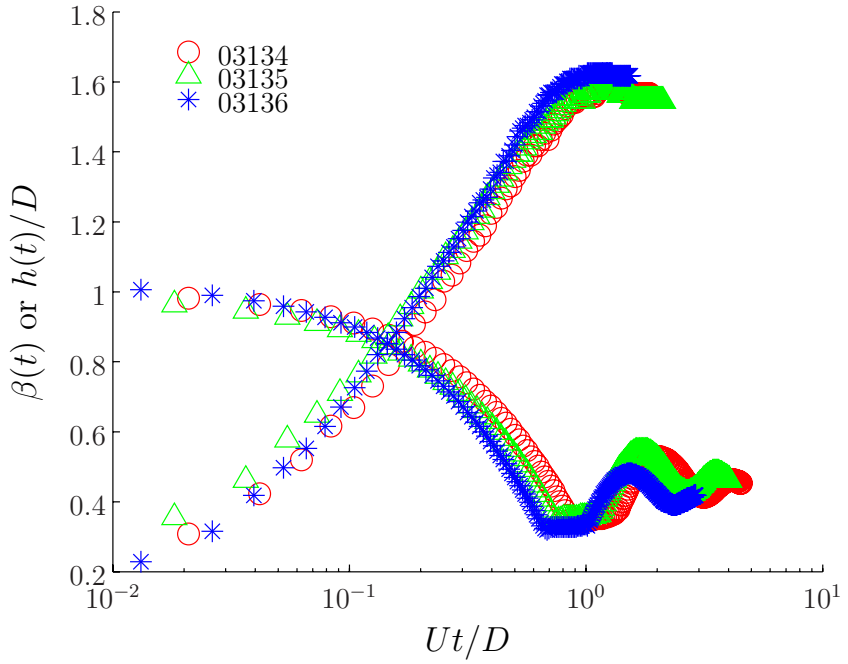

Figure 5.10: Spreading diameter and centerline height for #10, 5%($Oh = 0.047$) for $We = 10$.

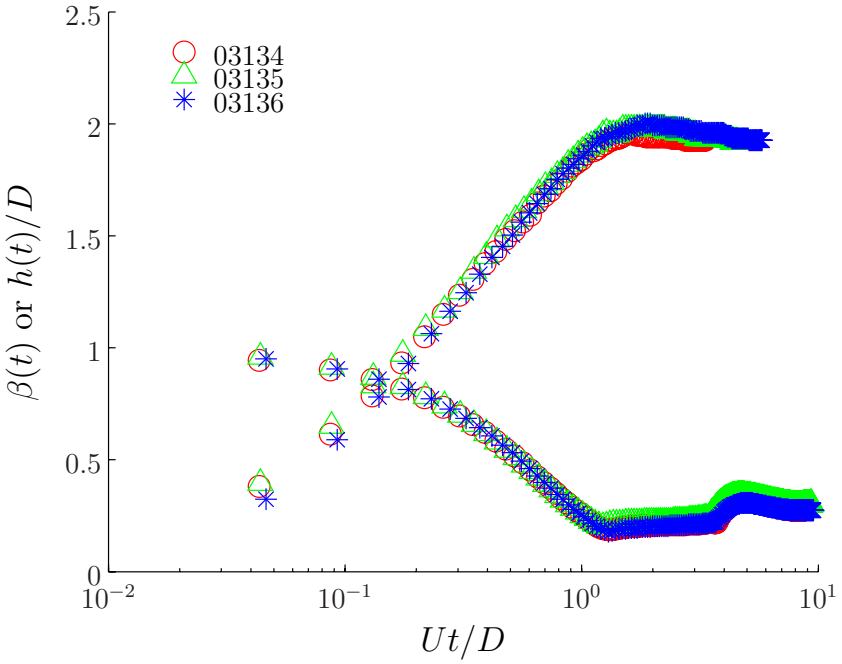

Figure 5.11: Spreading diameter and centerline height for #10, 5%($Oh = 0.047$) for $We = 30$.

If the inertia of the drop is sufficiently high and the contact line becomes pinned after a certain amount of spreading, the centerline height will sink below the toroidal rim and subsequently recover and proceed through either one or two periods of damped oscillation until it asymptotes. As the centerline height of the drop is moving upwards, the location of the rim rises to conserve mass until the centerline height of the drop rise above the rim, (see Figure 5.12). A representative spreading sequence showcasing the rise of the rim height until the final shape of the drop is a spherical cap is shown in Figure 5.13. Based on the surveyed literature, this phenomena has not been observed for drops with low Oh (0.001 for water). This behavior was also observed for similar high Oh experiments with colloidal dispersions, Bolleddula et al. [99]. This 'resonant' event occurs at We = 10-30 for $Oh = 0.043$ as seen in Figure 5.10. Furthermore, this behavior is not observed for higher the higher solid content acetone based solutions $Oh \sim$ 0.36-0.46(9, 8% and 3, 10%). Phase changing effects may play a stronger role a dissipating energy upon impact. We also observe a faster recovery for glycerol/water solutions compared to shear thinning acetone-based solutions, Figure 5.14.

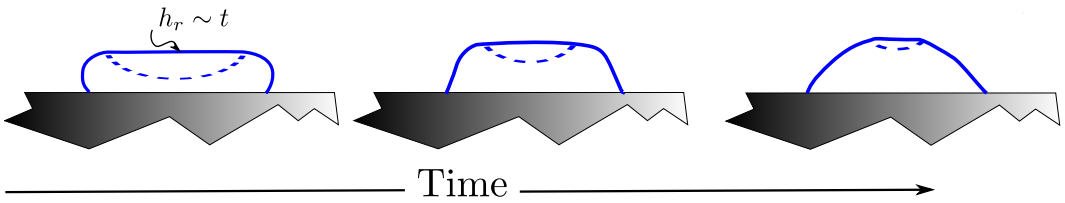

Figure 5.12: Schematic of rim height h_r location following impact driven spreading. The centerline height depression below rim occurs at times of 0.6-1.7 Ut/D.

We hypothesize that the physical mechanism is caused by a capillary wave that is initiated from the pinned contact line between the drop and target surface. When the drop makes contact with the solid surface, a wave is generated and travels around the side of the drop towards the apex. Subsequently, the wave travels back down as the drop is spreading. If the impact speed is too low then the wave is imperceptible as the centerline height will not dive below a potential rim. If the impact speed is too high,

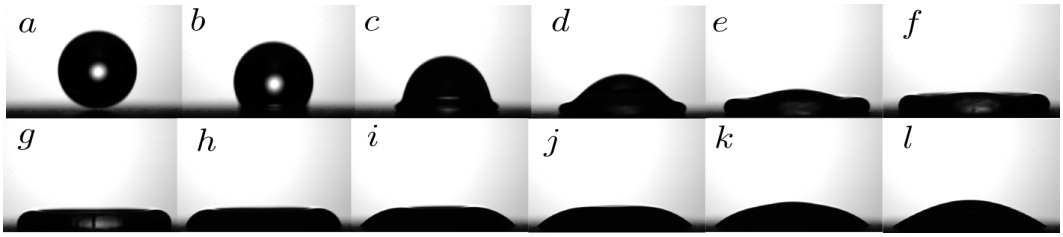

Figure 5.13: Sequence of solution 10, 5% on tablet 03134 at $We \approx 58$ and $D \approx 2.64$ mm. Entire sequence is 1.5 ms. Panels $g - j$ identify onset of centerline rim height locations.

then the periphery of the drop spreads to a further extent such that rim is always lower than the centerline height and the wave will again be imperceptible. If the We is sufficiently high such that the centerline height continues to decrease after the contact line is pinned, the motion associated with the wave resonates with that downward centerline motion, giving rise to a high amplitude oscillation that is observable in the surface of the drop. The wave eventually dissipates to a steady state position at an approximate dimensionless time of 4. The results have thus far demonstrated this characteristic behavior for drops that are millimeter sized. However, comparisons to realistic drop sizes $\mathcal{O}(10 - 100)\mu$m may further elucidate this 'resonant' behavior or any other additional mechanism.

The micron-size drops used in this study are created by perturbing a 200 micron diameter liquid jet which creates monodisperse drops in the 300 micron size range. The drops impact the solid surfaces at speeds of approximately 2-5 m/s and impact at $We \sim 100$ allowing direct comparison to the millimeter size drop. For $We \sim 300$ for solution 3, 10% solids, we observe a negligible effect in the spreading history, Figure 5.15. Since for the millimeter and micron size drops the Ohnesorge number is high (Oh = 0.47 and 0.9), respectively, the effect of viscosity is not dominant. However when the difference between Oh from millimeter and micron size drops changes by a factor of 10, the effect of the viscosity is enhanced as seen through the Oh. We see that the

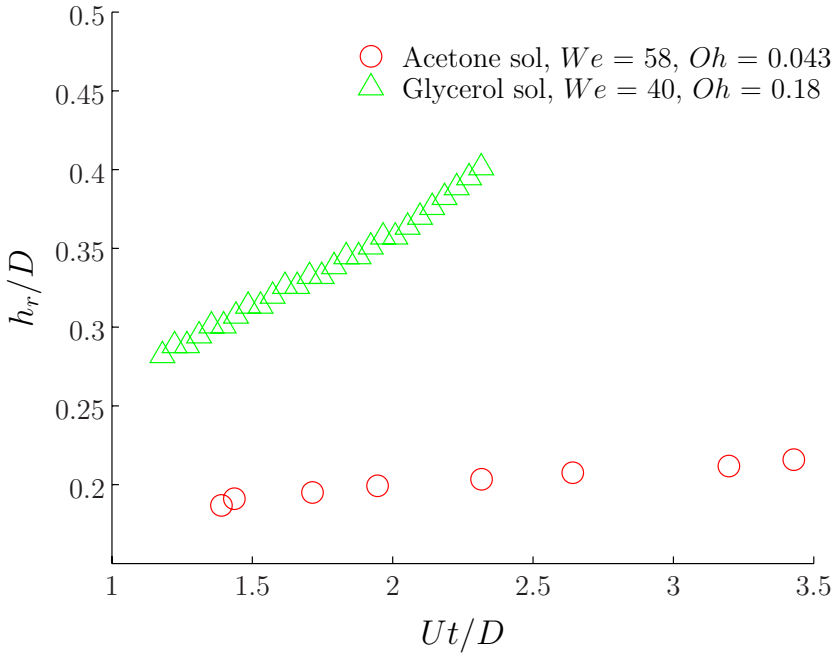

Figure 5.14: Rim height data scaled by impact diameter D for #10, 5% ($Oh = 0.043$) and Glycerol solution ($Oh = 0.18$) on substrates with static contact angles of 53° and 70°, respectively. Although the We and contact angles are not in exact agreement, the general behavior of the recovery of the rim height is preserved.

spreading process is hindered and slowed down by the enhanced effect of viscosity for solution 10 at moderate We, Figure 5.16. Although the spatial resolution of the optics is limited in this case, the behavior of the rim height, specifically the slope with which it goes up, is consistent with the previously described results: apparent linear rise height behavior in micron size drop impacts. The slope between the rim height from millimeter and micron size drop impacts is in good agreement for similar Oh values, Figure 5.17. However, due to the limited spatial resolution, further investigation is necessary to provide a detailed description of the rim height dynamics.

As an indication of the challenges working with this class of fluids we have begun to investigate the formation of a porous membrane that accompanies the phase change process as the acetone evaporates out of solution. We have observed directly that

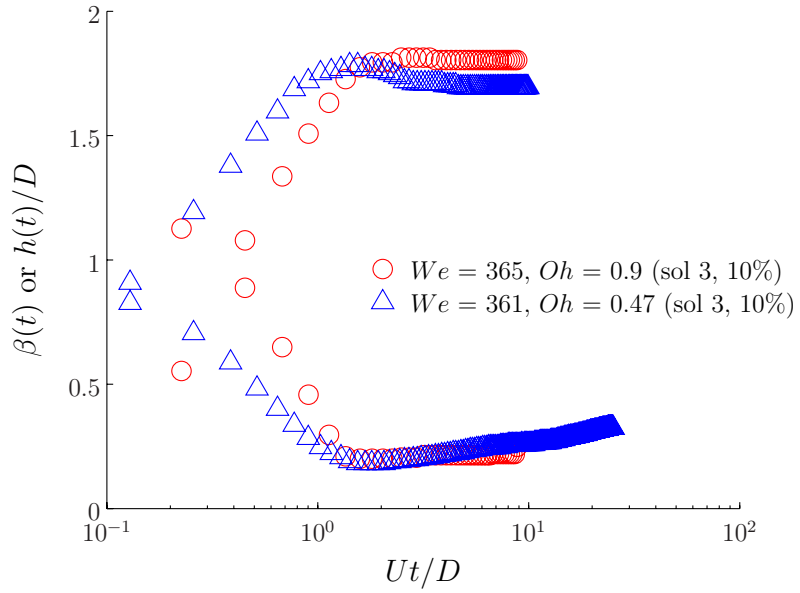

Figure 5.15: Comparison plot from millimeter ($Oh = .47$) and micron size ($Oh = .9$) drop impact of 3, 10%. The maximum spreading diameter is approximately equal while slight recession is observed for millimeter drop spreading.

when the drop is allowed to evaporate, a membrane forms around the periphery of the drop. To demonstrate the presence of this membrane we conducted an experiment to test the structural integrity of this membrane. We slowly pumped a drop of solution 10, 5% out of a syringe such that a drop is allowed to rest in the ambient environment and hence evaporate. The evaporation of the acetone accompanies the formation of a porous shell or membrane on the periphery of the drop. After waiting waiting a few seconds the drop is pumped such that the weight over the drop overcomes the surface tension and falls under it's own weight. The time from the creation of the drop to when it is released from the syringe tip is increased for three increasing intervals of exposure before release, $t = 0$, 5, 10 s, Figure 5.18. We observe that, for the sequence shown for a) $t = 0$s, the drop spreads rapidly upon contact. For b) $t = 5$s, the drop rebound partially and then spreads. Finally for c) $t = 10$s exposure, the drop actually bounces completely off the surface and then proceeds through 2 moderate rebounds

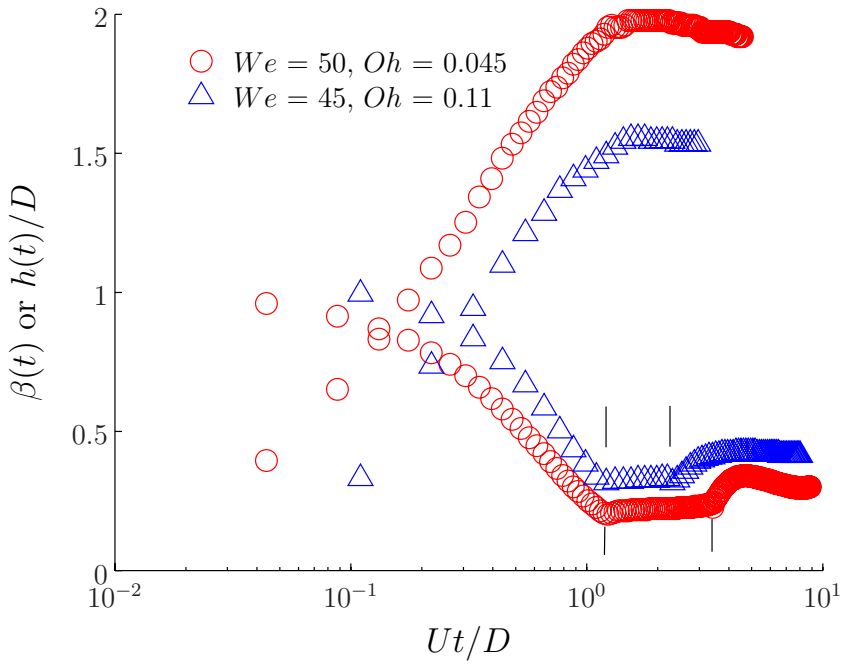

Figure 5.16: Comparison plot from mm and micron size drop impact of 10, 5%. The enhanced spreading for similar We is apparent since Oh is lower for larger drop size. Drop sizes are 2.5 mm and 386 μm, respectively. Solid vertical lines indicate location of rim height h_r data.

and then spreads to equilibrium. The extended exposure to the environment promotes the thickening of the membrane and thus sustains its presence over a longer period of time as indicated by 3 rebounds until the eventual rupture of the membrane allows the drop to spread. We hypothesize that the permeability of the membrane allows the acetone to mix and break down the membrane from the inside out until the liquid breaks locally and spreading takes over. We plan to investigate the characteristic time scale at which the membrane is strong enough to form a barrier to rupture in future studies.

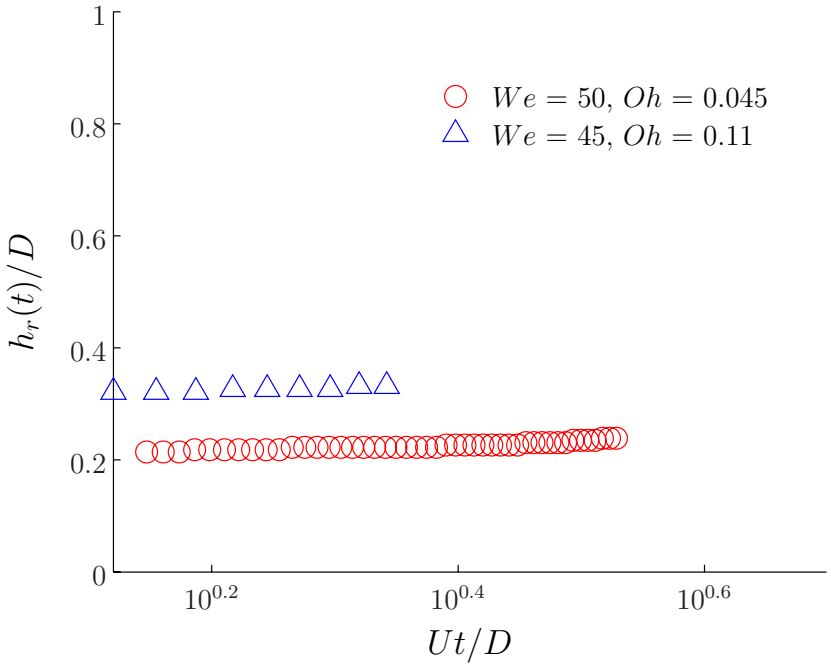

Figure 5.17: Rim height data extracted from Figure 5.16. Rim height recovery occurs between dimensionless times of 1.4-3.3 and 1.3-2.2 for mm and μm drop impacts, respectively.

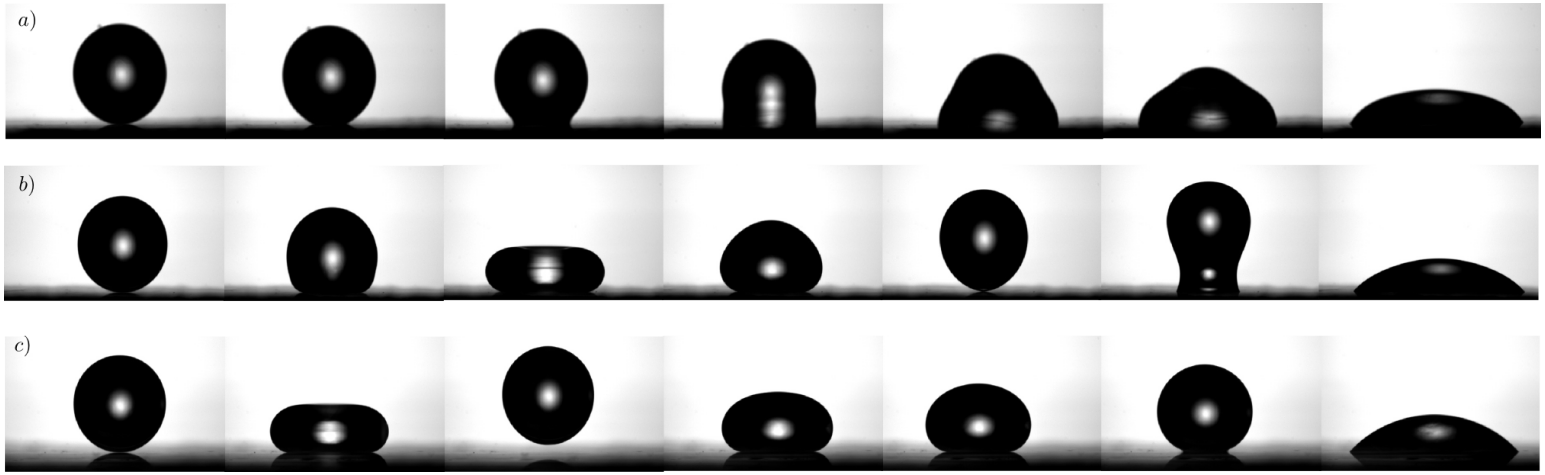

Figure 5.18: Indication of membrane formation on the periphery of the drop. A 2.22 mm drop is held at the end of a syringe for times $t = 0$, 5, and 10 s and then released. The drops then impact at $We \approx 2$. For sequence a), the drop spreads upon contact over a time of 11 ms. b) When the drop is exposed to the ambient environment for 5 s, the drop impacts, partially bounces and then spreads to equilibrium over a total time of 36 ms. c) Finally for $t = 10$s, the formation of the membrane inhibits drop spreading for 76 ms during which drop goes through 3 bounces until the contact line appears and spreads to equilibrium in 17 ms.

5.4 Conclusion

Pharmaceutically relevant acetone-based solutions were studied experimentally with a drop impact apparatus which created both mm and micron-size drops, over a range of $We \sim$ 1-300 and $Oh \sim$ 0.01-1. For these high viscosity fluids, the maximum spreading diameter is within 7% of predictive models created by Asai et al. [1] and Mao et al. [2]. Moreover, comparisons between millimeter and micron-sized drops revealed that for equivalent We, the spreading decreased due to the enhanced influence of viscosity characterized by the Oh. In this regime, a capillary wave 'resonant' regime was identified. When the centerline height of the drop falls under the rim and then proceeds to recover, the rim height is found to increase linearly with time, a behavior that to our knowledge, has not been documented in prior drop impact studies. Unlike drop impacts on hydrophobic surfaces where pyramidal or stair like shapes of the drop have been observed in a narrow We regime, the increased effect of viscosity damps these short wavelength structures. Furthermore, due to the highly volatile nature of these solutions, the acetone is prone to evaporate out of solutions. During this process the solid constituents precipitate leading to a porous membrane-like structure that serves as the final coat on the tablets. The formation of this membrane-like structure can inhibit spreading completely and lead to incomplete coatings. Determining the time scale for this film formation should provide key insight into this process and will be a subject of future investigation.

Chapter 6

CONCLUSIONS AND RECOMMENDATIONS

6.1 Conclusions

A systematic study of droplet impact was conducted with both canonical Newtonian fluids with high viscosity and complex rheology liquids relevant to the pharmaceutical industry. Such liquids contain large quantities of insoluble solids and result in an aqueous suspension or contain highly volatile constituents with membrane forming polymers in solution. At viscosities of $\mathcal{O}(10-100)$cP over a range of $We \sim \mathcal{O}(1-300)$, characteristic of spray coating conditions, we have demonstrated the outcome of drop impact results in spreading avoiding splash and rebound, with only minimal recession of the spreading diameter. The role of viscosity observed with and without colloids is reasoned to explain the inhibition of splashing and rebounding.

We confirm previous studies (Mao et al. [2] and Asai et al. [1]) that during the initial stages of impact corresponding to $Ut/D \sim$ 1-4, the spreading diameter is insensitive to wettability. Furthermore, we observe reasonable agreement with two existing models for β_{max} for all We studied. Despite reasonable agreement, the effect of the colloidal particles is not included and may assist in providing better accuracy in the models. The utility of maximum spreading diameter models developed by Asai et al. [1] and Mao et al. [2] still provide a robust model for predictive capability. Additionally, we verify that this extended viscous regime obeys $\beta_{max} \sim Re^{1/5}$ even for the complex rheology liquids studied herein.

Over a limited range, $We = 0.2-10$, these highly viscous colloidal dispersions were studied on a nearly wettable substrate immediately following the inertial driven phase. In this transient regime, capillarity is resisted by viscosity which yields a characteristic

time scale $\tau \sim \mu D/\sigma$. The spreading diameter showed excellent agreement with a power law $d(t)/D = C(t/\tau)^n$ where C is an $\mathcal{O}(1)$ constant and $1/7 \leq n \leq 1/5$. For these highly viscous colloidal dispersions $n \longrightarrow 1/5$ while for equivalently viscous glycerol solutions $n \rightarrow 1/10$. It is reasoned that the lower surface tension of the colloidal dispersions enhanced the rate of spreading in this transient regime. However the higher surface tension glycerol water solutions evolved closer to Tanner's law, $D \sim t^{1/10}$.

For highly viscous acetone-based solutions we find that the maximum spreading diameter agrees within 7% of the models of Asai et al. [1] and Mao et al. [2]. Furthermore, for critical Weber and Ohnesorge numbers, we observe the dynamics of the rim height in short inertial times. The rim height is shown to grow linearly with time as the centerline height recovers and proceeds through few damped oscillations to equilibrium. This behavior occurs at intermediate $We \sim 30 - 50$ and $Oh \sim 0.01$. During this regime, it is proposed that a capillary wave is initiated at the point of contact between the drop and substrate. Once the wave propagates around the periphery and meets at the apex it is reflected back finding a resonance with the motion of the centerline. The rim height is observed to increase linearly with time as the centerline height sinks and proceeds through one or two periods of damped oscillation. Additionally, we developed an experimental methodology to study viscous, ($Oh \sim 1$), μm sized drops over a range of $We \sim \mathcal{O}(1 - 100)$. This parameter space created experimental access for comparable We from millimeter and micron-sized drop impacts. There are relatively few experimental setups capable of measuring the small temporal and spatial characteristics of micron-sized drop impacts. In our study, we observed an enhanced effect of viscosity since $Oh \sim 1/D$.

The work in this dissertation has addressed a class of rheology that has been absent in the context of droplet impact and spreading despite their abundance in industrial applications. We hope the results from this study has helped clarify the role of densely populated dispersions in inertial and capillary driven spreading events. We also hope

to continue to investigating these types of spreading events both experimentally and theoretically to further elucidate the role of particles and phase transformations in moving contact line scenarios.

6.2 Recommendations for Future Work

The experimental data provided here on the capillary spreading of colloidal dispersions spreading on solid surfaces has not been compared to theory which captures the effects of particles. Thus, a theoretical study on the early and late time dynamics of the spreading diameter will provide confirmation of the power law behavior observed herein. Further experimentation should be directed on preexisting liquid layers of varying depth. These prewet surfaces experiments were not attempted herein but should demonstrate the effectiveness of coalescence and hence uniformity of the coat. As we briefly showcased in Chapter 5, the acetone based solutions form a porous membrane on the free surface when exposed to air. This phase change process and it's role in spreading dynamics would open a relatively unstudied class of problems both theoretically and experimentally.

Appendix A

IMAGE PROCESSING

The following protocol outlines the steps used to extract data from raw videos using the image analysis software, Spotlight.

1. Click on AOI $\longrightarrow$ Process Sequence

2. Create a Process Sequence in the following order

3. Filter - smooth, Contrast - linear stretch, Morphological - outline, and Threshold - simple - standard (61). (*Note that the threshold is what must be controlled to accurately track a moving interface. Take care in defining an appropriate threshold for each image sequence.*)

4. Save Image processing sequence and click OK

5. Click on AOI $\longrightarrow$ New $\longrightarrow$ Threshold tracking

6. Place box over area of interest and point arrow in anticipated direction of movement

7. Load Process Sequence then click on Track Continuous.

Once the data file is created it can be processed for analysis.

Appendix B

MATERIALS PROPERTIES LIST: LIQUIDS AND SURFACES

Table B.1: Composition list of coating solutions from Pfizer.

#	Coating Type	% Solids
1	Opadry II White HPMC/Lactose/TiO_2/ Triacetin	15
2	Opadry II White PVA/PEG	20
3	Pfizer Membrane	10
4	Opadry II White HPMC/Lactose/TiO_2/ Triacetin/PEG	15
5	Opadry II White HPMC/Lactose/TiO_2/ Triacetin	10, 12, and 15
6	Opadry Clear HPMC/Triacetin	5
7	Opadry I White HPMC/TiO_2/PEG	15
8	Opadry I Blue HPMC/TiO_2/PEG	15
9	Pfizer Membrane	8
10	Pfizer Membrane	5
11	Opadry II Blue PVA/PEG/ Soy lecithin/TiO_2/Talc	15 and 18
12	Opadry II Blue HPMC/Lactose/TiO_2/Triacetin	10 and 18
13	Opadry II White PVA/PEG/ TiO_2/Talc	18, 20

Table B.2: Coating liquids properties list. Viscosities maintain slightly shear thinning characteristics yet at $1000s^{-1}$ the viscosity is listed here. (* denotes interpolated value)

#, % solids	T, °C	ρ, kg/m^3	σ, N/m	μ, N·s/m^2 @ 1000 s^{-1}
1, 15	25.4	1050	0.04698	0.098
2, 20	25.4	1070	0.04393	0.039
3, 10	25.4	820	0.02971	0.102
4, 15	25.4	1040	0.04707	0.074
5, 10	25.4	1020	0.04822	0.098
5, 12	25.4	1030	0.04766	0.175
5, 15	25.4	1040	0.04667	0.377
6, 5	25.4	990	0.04772	0.081
7, 15	25.4	1040	0.04769	0.307
8, 15	25.4	1040	0.03195	0.294
9, 8	25.4	870	0.02732	0.115
10, 5	25.4	800	0.02732	0.011
11, 15	25.4	1050	0.04421	0.018
11, 18	25.4	1060	0.04483	0.031
12, 10	25.4	1020	0.04782	0.091
12, 15	25.4	1040	0.04835	0.405
13, 18	25.4	1050	0.04608	0.027
13, 20	25.4	1060*	0.04700*	0.042

Table B.3: Summary of tablet surfaces in impact study. Tablets are described by sample content, tablet weight, breaking force, and main variable.

#	Lot #	Sample Information	Tab Weight, mg	Tablet Breaking Force, kp	Variable
1	031-1-1	100% Methocel K4M CR Premium (controlled release polymer) -Hydrophilic	346	14	Tablet breaking force or hardness
2	031-1-2	100% Methocel K4M CR Premium (controlled release polymer) -Hydrophilic	348	22	Tablet breaking force or hardness
3	031-2	100% Polyethylene Glycol (PEG 3350) -Hydrophilic	N/A	10	Waxy material
4	031-3-1	100% Microcrystalline Cellulose (MCC or Avicel PH102)	352	16	Control Hydrophilic (no lubricant)
5	031-3-2	MCC : magnesium stearate 99.5:0.5	383	19	0.5 % lubricant
6	031-3-3	MCC : magnesium stearate 99: 1	395	19	1 % lubricant
7	031-3-4	MCC : magnesium stearate 98:2	400	15	2 % lubricant
8	031-3-5	MCC : magnesium stearate 96:4	394	11	4 % lubricant
9	031-3-6	100% Microcrystalline Cellulose (MCC or Avicel PH102) Hydrophilic :hydrophobic	396	28	Control Hydrophilic (no lubricant) compressed with higher weight

BIBLIOGRAPHY

[1] A. Asai, M. Shioya, S. Hirasawa, and T. Okazaki. Impact of an ink drop on paper. *Journal of imaging science and technology*, 37, 1993.

[2] T. Mao, D.C.S. Kuhn, and H. Tran. Spread and rebound of liquid droplets upon impact on flat surfaces. *AIChE Journal*, 43:2169–2179, 1997.

[3] I.V. Roisman. Inertia dominated drop collisions. ii. an analytical solution of the navier-stokes equations for a spreading viscous film. *Physics of Fluids*, 21, 2009.

[4] A. Aliseda, E.J. Hopfinger, J.C. Lasheras, D.M. Kremer, A. Berchielli, and E.K. Connolly. Atomization of viscous and non-newtonian liquids by a coaxial, high-speed gas jet. experiments and droplet size modeling. *International Journal of Multiphase Flow*, 34:161–175, 2008.

[5] S. Sartori. Temporal and spatial study of drying of suspension and solution droplets for tablets coating purposes. Master's thesis, UCSD, 2010.

[6] S.A. Altinkaya. In vitro dry release rates from asymmetrc-membrane tablet coatings: prediction of phase-inversion dynamics. *Biochemical Engineering Journal*, 28:131–139, 2006.

[7] S. Middleman. *Modeling Axisymmetric Flows*. Academic Press, London, 1995.

[8] J.F. Dijksman. Hydrodynamics of small tubular pumps. *Journal of Fluid Mechanics*, 139:173–191, 1984.

[9] A.U. Chen and O.A. Basaran. A new method for significantly reducing drop radius without reducing nozzle radius in drop-on-demand drop production. *Physics of Fluids Letters*, 14, 2002.

[10] Y. Son and C. Kim. Spreading of inkjet droplet of non-newtonian fluid on solid surface with controlled contact angle at low weber and reynolds numbers. *Journal of Non-Newtonian Fluid Mechanics*, 162:78–87, 2009.

[11] V. Bergeron, D. Bonn, J.Y. Martin, and L. Vovelle. Controlling droplet deposition with polymer additives. *Nature*, 405:772–775, 2000.

[12] D. Bartolo, A. Boudaoud, G. Narcy, and D. Bonn. Dynamics of non-newtonian droplets. *Physical Review Letters*, 99:174502–1–174502–4, 2007.

[13] R. Rioboo and C. Tropea. Outcomes from a drop impact on solid surfaces. *Atomization and Sprays*, 11:155–165, 2001.

[14] M. Rein. Phenomena of liquid drop impact on solid and liquid surfaces. *Fluid Dynamics Research*, 12:61–93, 1993.

[15] A.L. Yarin. Drop impact dynamics: Splashing, spreading, receding, bouncing... *Annual Review of Fluid Mechanics*, 38:159–192, 2006.

[16] X. Zhang and O.A. Basaran. Dynamic surface tension effects in impact of a drop with a solid surface. *Journal of Colloid and Interface Science*, 187:166–178, 1997.

[17] D. Kannangara, H. Zhang, and W. Shen. Liquid-paper interactions during liquid drop impact and recoil on paper surfaces. *Colloids and Surfaces A: Physicochemical and Engineering Aspects*, 280:203–215, 2006.

[18] R.C. Daniel and J.C. Berg. Spreading on and penetration into thin, permeable

print media: Application to ink-jet printing. *Advances in Colloids and Interface Science*, pages 439–469, 2006.

[19] A. M. Worthington. On the forms assumed by drops of liquids falling vertically on a horizontal plate. *Proceedings of the Royal Society of London*, 25:261–272, 1876. ISSN 03701662.

[20] J.C. Berg. *An Introduction to Interfaces and Colloids: The Bridge to Nanoscience*. World Scientific Publication Co., 2010.

[21] P.G. de Gennes. Wetting: statics and dynamics. *Review of Modern Physics*, 57:827–863, 1985.

[22] V.M. Starov, V.V. Kalinin, and J.D. Chen. Spreading of liquid drops over dry surfaces. *Advances in Colloid and Interface Science*, 50:187–221, 1994.

[23] R.G. Cox. The dynamics of the spreading of liquids on a solid surface. Part 1. Viscous flow. *Journal of Fluid Mechanics*, 168:169–194, 1986.

[24] L.M. Hocking and A.D. Rivers. The spreading of a drop by capillary action. *Journal of Fluid Mechanics*, 121:425–442, 1982.

[25] R. Rioboo, M. Marengo, and C. Tropea. Time evolution of liquid drop impact onto solid, dry surfaces. *Experiments in Fluids*, 33:112–124, 2002.

[26] L.H. Tanner. The spreading of silicone oil drops on horizontal surfaces. *J. Phys. D: Appl. Phys.*, 12, 1979.

[27] J. Chen. Experiments on a spreading drop and its contact angle on a solid. *Journal of Colloid and Interface Science*, 122, 1988.

[28] S. Rafaï, D. Bonn, and A. Boudaoud. Spreading of non-newtonian fluids on hydrophilic surfaces. *Journal of Fluid Mechanics*, 513:77–85, 2004.

[29] E.B. Dussan. On the spreading of liquids on solid surfaces: static and dynamic contact lines. *Annual Review of Fluid Mechanics*, 11:371–400, 1979.

[30] S. Chandra and C.T. Avedisian. On the collision of a droplet with a solid surface. *Proceedings of the Royal Society of London*, 432:13–41, 1991.

[31] D.B. van Dam and C.L. Clerc. Experimental study of the impact of an ink-jet printed droplet on a solid surface. *Physics of Fluids*, 16, 2004.

[32] V. Medhi-Nejad, J. Mostaghimi, and S. Chandra. Air bubble entrapment under an impacting droplet. *Physics of Fluids*, 15:173–183, 2003.

[33] P. Attané, F. Girard, and V. Morin. An energy balance approach of the dynamics of drop impact on a solid surface. *Physics of Fluids*, 19, 2007.

[34] I.V. Roisman, E. Berberović, and C. Tropea. Inertia dominated drop collisions. i. on the universal flow in the lamella. *Physics of Fluids*, 21, 2009.

[35] C. Clanet, C Beguin, D. Richard, and D. Quere. Maximal deformation of an impacting drop. *Journal of Fluid Mechanics*, 517:199–208, 2004.

[36] B.L. Scheller and D.W. Bousfield. Newtonian drop impact with a solid surface. *AIChE Journal*, 41, 1995.

[37] M. Pasandideh-Fard, Y.M. Qiao, S. Chandra, and J. Mostaghimi. Capillary effects during droplet impact on a solid surface. *Physics of Fluids*, 8:650–659, 1996.

[38] I.V. Roisman, R. Rioboo, and C. Tropea. Normal impact of a liquid drop on a dry surface: model for spreading and receding. *Proceedings of the Royal Society of London*, 458:1411–1430, 2002.

[39] T. Bennett and D. Poulikakos. Splat-quench solidification: estimating the maximum spreading of a droplet impacting a solid surface. *Journal of Materials Science*, 28:963–970, 1993.

[40] Š. Šikalo, C. Tropea, and E.N. Ganić. Impact of droplets onto inclined surfaces. *Journal of Colloid and Interface Science*, 286:661–669, 2005.

[41] S. Bakshi, I.V. Roisman, and C. Tropea. Investigations on the impact of a drop onto a small spherical target. *Physics of Fluids*, 19, 2007.

[42] F.H. Harlow and J.P. Shannon. The splash of a liquid drop. *Journal of Applied Physics*, 38:3855–3866, 1967.

[43] S.E. Bechtel, D.B. Bogy, and F.E. Talke. Impact of a liquid drop against a flat surface. *IBM J. Res. Develop.*, 25:963–971, 1981.

[44] J. Fukai, Z. Zhao, D. Poulikakos, and C.M. Megaridis. Modeling of the deformation of a liquid drop impinging upon a flat surface. *Physics of Fluids*, 5: 2588–2599, 1993.

[45] J. Fukai, Y. Shiiba, T. Yamamoto, O. Miyatake, D. Poulikakos, C.M. Megaridis, and Z. Zhao. Wetting effects on the spreading of a liquid droplet colliding with a flat surface: Experiment and modeling. *Physics of Fluids*, 7:236–247, 1995.

[46] M. Bussman, J. Mostaghimi, and S. Chandra. On a three-dimensional volume tracking model of droplet impact. *Physics of Fluids*, 11:1406–1417, 1999.

[47] M.R. Davidson. Boundary integral predication of the spreading of an inviscid drop impacting on a solid surface. *Chemical Engineering Science*, 55:1159–1170, 2000.

[48] M. Pasandideh-Fard, S. Chandra, and J. Mostaghimi. A three-dimensional

model of droplet impact and solidification. *International Journal of Heat and Mass Transfer*, 45:2229–2242, 2002.

[49] D. Quéré. Wetting and roughness. *Annual Review of Materials Research*, 38: 71–99, 2008.

[50] D. Richard and D. Quéré. Bouncing water drops. *Europhysics Letters*, 50: 769–775, 2000.

[51] K. Okumura, F. Chevy, D. Richard, D. Quere, and C. Clanet. Water spring: A model for bouncing drops. *Europhysics Letters*, 62:237–243, 2003.

[52] Y. Renardy, S. Popinet, L. Duchemin, M. Renardy, S. Zaleski, C. Josserand, M.A. Drumright-Clarke, D. Richard, C. Clanet, and D. Quere. Pyramidal and toroidal water drops after impact on a solid surface. *Journal of Fluid Mechanics*, 484:69–83, 2003.

[53] I.S. Bayer and C.M. Megaridis. Contact angle dynamics in droplets impacting on flat surfaces with different wetting characteristics. *Journal of Fluid Mechanics*, 558:415–449, 2006.

[54] T.D. Blake and J. Haynes. The kinetics of liquid/liquid displacement. *Journal of Colloid and Interface Science*, 30, 1969.

[55] R. Kannan and D. Sivakumar. Impact of liquid drops on a rough surface comprising microgrooves. *Experiments in Fluids*, 44:927–938, 2008.

[56] H.-Y. Kim and J.-H. Chun. The recoiling of liquid droplets upon collision with solid surfaces. *Physics of Fluids*, 13:643–659, 2001.

[57] D. Caviezel, C. Narayanan, and D. Lakehal. Adherence and boucing of liquid droplets impacting on dry surfaces. *Microfluid Nanofluid*, 5:469–478, 2008.

[58] F.J. Heymann. High-speed impact between a liquid drop and a solid surface. *Journal of Applied Physics*, 40:5113–5122, 1969.

[59] M.B. Lesser. Analytic solutions of liquid-drop imact problems. *Proceedings of the Royal Society of London*, 377:289–308, 1981.

[60] M.B. Lesser and J.E. Field. The impact of compressible liquids. *Annual Review of Fluid Mechanics*, 15:97–122, 1983.

[61] J.P. Dear and J.E. Field. High-speed photography of surface geometry effects in liquid/solid impact. *Journal of Applied Physics*, 63:1015–1021, 1988.

[62] J.E. Field, J.P. Dear, and J.E. Ogren. The effects of target compliance on liquid drop impact. *Journal of Applied Physics*, 65:533–540, 1989.

[63] C.D. Stow and M.G. Hadfield. An experimental investigation of fluid flow resulting from the impact of a water drop with an unyielding dry surface. *Proceedings of the Royal Society of London*, 373:419–441, 1981.

[64] CHR. Mundo, M. Sommerfeld, and C. Tropea. Droplet-wall collisions: Experimental studies of the deformation and breakup process. *International Journal of Multiphase Flow*, 2:151–173, 1995.

[65] K. Range and F. Feuillebois. Influence of surface roughness on liquid drop impact. *Journal of Colloid and Interface Science*, 203:16–30, 1998.

[66] A.L. Yarin and D.A. Weiss. Impact of drops on solid surfaces: self-similar capillary waves, and splashing as a new type of kinematic discontinuity. *Journal of Fluid Mechanics*, 283:141–173, 1995.

[67] R. D. Cohen. Shattering of a liquid drop due to impact. *Proceedings of the Royal Society of London*, 435:483–503, 1991.

[68] R. Bhola and S. Chandra. Parameters controlling solidification of molten wax droplets falling on a solid surface. *Journal of Materials Science*, 34:4883–4894, 1999.

[69] S.D. Aziz and S. Chandra. Impact, recoil and splashing of molten metal droplets. *International Journal of Heat and Mass Transfer*, 43:2841–2857, 2000.

[70] M. Bussmann, S. Chandra, and J. Mostaghimi. Modeling the splash of a droplet impacting a solid surface. *Physics of Fluids*, 12:3121–3132, 2000.

[71] J.C. Bird, S. S H Tsai, and H.A. Stone. Inclined to splash: triggering and inhibiting a splash with tangential velocity. *New Journal of Physics*, 11, 2009.

[72] L. Xu, W.W. Zhang, and S.R. Nagel. Drop splashing on a dry smooth surface. *Physical Review Letters*, 94:184505–1–4, 2005.

[73] L. Xu, L. Barcos, and S.R. Nagel. Splashing of liquids: Interplay of surface roughness with surrounding gas. *Physical Review E*, 76, 2007.

[74] S. Mandre, M. Mani, and M.P. Brennner. Precursors to splashing of liquid drops on a solid surface. *Physical Review Letters*, 102, 134502, 2009.

[75] Stefano Schiaffino and Ain A. Sonin. Molten droplet deposition and solidification at low weber numbers. *Physics of Fluids*, 9(11):3172–3187, 1997. doi: 10.1063/1.869434.

[76] D. Attinger, A. Zhao, and D. Poulikakos. An experimental study of molten microdroplet surface deposition and solidification: Transient behavior and wetting angle dynamics. *ASME*, 2000.

[77] H. Dong, W.W. Carr, and J.F. Morris. Visualization of drop-on-demand inkjet: Drop formation and deposition. *Review of Scientific Instruments*, 77, 2006.

[78] H.J. Shore and G.M. Harrison. The effect of added polymers on the formation of drops ejected from a nozzle. *Physics of Fluids*, 17, 2005.

[79] Y. Son, C. Kim, D.H. Yang, and D.J. Ahn. Spreading of an inkjet droplet on a solid surface with a controlled contact angle at low weber and reynolds numbers. *Langmuir*, 24:2900–2907, 2008.

[80] M. Toivakka. Numerical investigation of droplet impact spreading in spray coating of paper. In *Spring Advanced Coating Fundamentals Symposium*, 2003.

[81] N. Mourougou-Candoni, B. Prunet-Foch, F. Legay, M. Vignes-Adler, and K. Wong. Influence of dynamic surface tension on the spreading of surfactant solution droplets impacting onto a low-surface-energy solid substrate. *Journal of Colloid and Interface Science*, 192:129–141, 1997.

[82] N. Mourougou-Candoni, B. Prunet-Foch, F. Legay, and M. Vignes-Adler. Retraction phenomena of surfactant solution drops upon impact on a solid substrate of low surface energy. *Langmuir*, 15:6563–6574, 1999.

[83] B. Prunet-Foch, F. Legay, M. Vignes-Adler, and C. Delmotte. Impacting emulsion drop on a steel plate: Influence of the solid substrate. *Journal of Colloid and Interface Science*, 199:151–168, 1998.

[84] J.J. Cooper-White, R.C. Crooks, and D.V. Boger. A drop impact study of worm-like viscoelastic surfactant solutions. *Colloids and Surfaces A: Physicochemical and Engineering Aspects*, 210:105–123, 2002.

[85] J.J. Cooper-White, R.C. Crooks, K. Chockalingham, and D.V. Boger. Dynamics of polymer-surfactant complexes: Elongational properties and drop impact behavior. *Ind. Eng. Chem. Res.*, 41:6443–6459, 2002.

[86] A. Rozhkov, B. Prunet-Foch, and M. Vignes-Adler. Impact of drops of polymer solutions on small targets. *Physics of Fluids*, 15:2006–2019, 2003.

[87] A. Rozhkov, B. Prunet-Foch, and M. Vignes-Adler. Dynamics and disintegration of drops of polymeric liquids. *Journal of Non-Newtonian Fluid Mechanics*, 134:44–55, 2006.

[88] M. Nicolas. Spreading of a drop of neutrally buoyant suspension. *Journal of Fluid Mechanics*, 545:271–280, 2005.

[89] S. Nigen. Experimental investigation of the impact of an (apparent) yield-stress material. *Atomization and Sprays*, 15:103–117, 2005.

[90] A. Saïdi, C. Martin, and A. Magnin. Influence of yield stress on the fluid droplet impact control. *Journal of Non-Newtonian Fluid Mechanics*, 165:596–606, 2010.

[91] R. Klimek and R. Wright. Spotlight-8 image analysis software. *NASA TM*, 214084, 2006.

[92] H. Dong, W.W. Carr, D.G. Bucknall, and J.F. Morris. Temporally-resolved inkjet drop impaction on surfaces. *AIChE Journal*, 53, 2007.

[93] J. J. Stickel and R.L. Powell. Fluid mechanics and rheology of dense suspensions. *Annual Review of Fluid Mechanics*, 37:129–149, 2005.

[94] J.N. Israelachvili. *Intermolecular and surface forces*. Academic Press, 1985.

[95] J. Eggers and H.A. Stone. Characteristic lengths at moving contact lines for a perfectly wetting fluid: the influence of speed on the dynamic contact angle. *Journal of Fluid Mechanics*, 505:309–321, 2004.

[96] R.V. Craster, O.K. Matar, and K. Sefiane. Pinning, retraction, and terracing of evaporating droplets containing nano. *Langmuir*, 25:3601–3609, 2009.

[97] H.J. Jeong, W.R. Hwang, C. Kim, and S.J. Kim. Numerical simulations of capillary spreading of a particle-laden droplet on a solid surface. *Journal of Materials Processing Technology*, 210:297–305, 2010.

[98] C.K. Law. Multicomponent droplet combustion with rapid internal mixing. *Combustion and Flame*, 26:219–333, 1976.

[99] D.A. Bolleddula, A. Berchielli, and A. Aliseda. Impact of a heterogeneous liquid droplet on a dry surface: application to the pharmaceutical industry. *Advances in Colloid and Interface Science*, 159:144–159, 2010.

[100] S.A. Altinkaya and B. Ozbas. Modeling of asymmetric membrane formation by dry-casting method. *Journal of Membrane Science*, 230:71–89, 2004.

[101] S.A. Altinkaya, H. Yenal, and B. Ozbas. Membrane formation by dry-cast process model validation through morphological studies. *Journal of Membrane Science*, 249:163–172, 2005.

[102] J. de Ruiter, R.E. Pepper, and H.A. Stone. Thickness of the rim of an expanding lamella near the splash threshold. *Physics of Fluids*, 2010.

[103] I.V. Roisman, K. Horvat, and C. Tropea. Spray impact: rim transverse instability initiating fingering and splash, and description of a secondary spray. *Physics of Fluids*, 18, 2006.